NANO-SQUID SUSCEPTOMETRY AND FLUCTUATION EFFECTS IN SUPERCONDUCTING RINGS

A DISSERTATION
SUBMITTED TO THE DEPARTMENT OF APPLIED PHYSICS
AND THE COMMITTEE ON GRADUATE STUDIES
OF STANFORD UNIVERSITY
IN PARTIAL FULFILLMENT OF THE REQUIREMENTS
FOR THE DEGREE OF
DOCTOR OF PHILOSOPHY

Nicholas C. Koshnick
March 2009

I certify that I have read this dissertation and that, in my opinion, it is fully adequate in scope and quality as a dissertation for the degree of Doctor of Philosophy.

(Kathryn A. Moler) Principal Adviser

I certify that I have read this dissertation and that, in my opinion, it is fully adequate in scope and quality as a dissertation for the degree of Doctor of Philosophy.

(Malcolm R. Beasley)

I certify that I have read this dissertation and that, in my opinion, it is fully adequate in scope and quality as a dissertation for the degree of Doctor of Philosophy.

(David Goldhaber-Gordon)

Approved for the University Committee on Graduate Studies.

Abstract

This thesis is broken down into two main components: the design and implementation of two generations of Scanning Superconducting Quantum Interference Device (SQUID) sensors, and the use of these tools to describe several kinds of fluctuations that can significantly affect the properties of micron sized aluminum rings.

The first chapter describes the susceptometer that was used for the bulk of the ring experiments. In it, I outline the advantages of a multi-layer design with local field coils and integrated feedback loops. To reach the fundamental sensitivity limits set by Johnson noise in the device itself, I employed piezo electric positioners to measure background magnetic fields, in addition to taking images of the magnetic field. The second chapter describes a generation of SQUIDs with FIB-patterned pickup loops that are connected to a similar base design. The coupling to ultra-small objects is significantly enhanced by the pickup loop's small diameter (down to ~ 600 nm) and reduced scan height ($\lesssim 300$ nm) enabled by lithographically patterned terraces. When combined with our device's low flux noise, this enhanced coupling brings SQUIDs close to the point where they could distinguish the field from a single electron spin.

Fluctuations are important for superconductors when multiple wave-function configurations need to be considered to describe the overall behavior of the system. This study includes several experimental regimes where physically distinct energy scales play an important role. In relatively dirty rings, I show how fluxoid transitions can significantly reduce the ring's ability to screen magnetic field. In smaller, cleaner rings, the contribution from fluxoid modes plays a smaller role, and non-Gaussian and Gaussian fluctuations induce superconductivity at and above the superconducting critical temperature, T_c. In this case, I also focus on rings that are biased with half

of a flux quantum of field, which enables two flux modes to contribute to the ring's response. I specify the point where thermal fluctuations smear out the Little-Parks effect, where T_c is reduced due to the Aharonov-Bohm phase winding energy. In the final section, I report on our efforts to fabricate and measure ultra clean rings where the Thouless energy is approximately equal to T_c.

Acknowledgements

I believe physics is still largely an oral tradition, where we learn from each other through countless hours of debate. I would like to thank my advisor, Kathryn Moler, for being the best leader I know in allowing this to happen. She has always been fair and even in mitigating the inevitable disputes. She has insisted on a lab and group meeting environment that is energized by debate. This has forced me to re-examine my assumptions, and has allowed me to connect all I know to basic principles. Finally, her leadership has influenced us to laugh a bit, and to enjoy both work and play. I would also like to thank Kam for pushing for certain results, for always requiring us to rigorously defend our methods, and for teaching me a bit of the art of scientific writing.

Most of my work was done with the mesoscopics subgroup. I can't thank Hendrik Bluhm enough, not only for starting this effort in earnest, but for always being an active ear and willing debater. Working with him brought me to a higher theoretical level, and he instilled a certain level of experimental discipline that I would not have had on my own. I thank Julie Bert, the newest member, for helping with all of the projects, and in particular for carrying out a lion's share of work in screening the nano-SQUIDs presented in chapter 3. Her discipline and competence will lead to exciting results in the years to come.

There are many people outside of our lab who have played a large role in allowing my work to happen. Most notably is Martin Huber, who worked with me on the nano-SQUID design and completed all of the optical fabrication steps. Much of my mastery of SQUID technologies, such as SQUID array amplifiers, is directly related to his influence. I also thank Hal Edwards, Jeff Large, and Steve O'Connel for working

with us to establish a FIB fabrication method when it was clear an E-beam approach would not work.

Many people have helped me understand fluctuations in superconducting rings. Foremost, I thank Xiaxian Zhang and John Price. Their work in the mid 90's laid the foundation for almost all of our work. Conversations with John led us to anticipate the effects of SQUID radiation, and to consider bilayered samples as an attractive candidate material for making rings (see chapter 6). I thank Georg Schwiete for patiently teaching me almost everything I know about non-gaussian fluctuations, and Jorge Berger for organizing a conference on the subject, and following up on the work with correspondence and work of inhomogeneities.

Moler lab members, both past and present, have been like an extended family. Ophir Auslaender, Brian Gardner, Lan Luan, and Clifford Hicks in particular have taught me numerous things, daily. I thank all my Physics/Applied Physics friends for shaping my understanding and, of course, all the faculty for their teaching efforts. All the McCullough basement dwellers, and in particular Ron Potok and Myles Steiner for teaching me general lab techniques and basic lithography, respectively. James Conway has gone beyond the call of duty to help keep the ebeam writer working well, and Bob Hammond and Tom Carver have been invaluable for their knowledge of metallurgy. The GLAM/CPN staff Laraine Lietz-Lucas, Cyndi Mata Barnett, and Stephen Swisher for cutting the red tape, and Kyle Cole for giving me numerous outreach opportunities, and reminding me of how much I love to teach.

I want to thank my reading committee members, Mac Beasley and David Goldhaber-Gordon, for being there to lend a supportive ear with many pointers along the way. Mac's superconductivity class and David's mesoscopics reading class were two of the best and most useful classes I took at Stanford.

Finally, I would like to thank my Mom, who is one of the most creative people I know, and who worked to instill that quality in me from a young age. My Dad, who taught me to be a diligent student, to calculate things in the back of my head, and to always come to my own conclusions. And Maureen, who has broadened and redoubled my interest in both science and new technologies, and who has taught me a bit about how to be a passionate human as well as a good scientist.

Contents

List of Tables

List of Figures

Chapter 1

Overview and introduction

This thesis describes superconducting fluctuation effects in micron-sized aluminum rings. The rings were studied experimentally using a SQUID, or Superconducting Quantum Interference Device, which at the simplest level is simply a tool that measures magnetic field. We fabricate these SQUIDs on one wafer, and polish it so that the active area of the device is near the corner. We fabricate the rings on a separate wafer, and bring the SQUID down over each ring, measuring the ring's response to an applied field, one at a time. The device used for these measurements, and some details of the technique, will be the subject of chapter 2. Chapter 3 describes a new SQUID that is smaller and closer to the sample, allowing for a much better spin sensitivity. These two published papers include historical references, and appendix B puts these devices in the context of our ideas for future work. This introduction will begin with a broader introduction to superconductivity, from which the basic properties of SQUIDs can be derived. Since numerous books [21] review both the basics and intricacies or SQUID design, this chapter is focused on the historical importance of fluctuation effects in superconductors, and their broad relation to the work presented in chapters 4, 5, and 6.

Low temperature experiments have allowed physicists to measure many exotic states of matter. One of the most dramatic effects is the phenomenon of superconductivity. Superconductivity occurs when a suitable material is cooled below some critical temperature, T_c, which allows the electrons to undergo a phase transition

to a state where they behave cooperatively. Once superconductivity occurs, their collective behavior can be described by a macroscopic quantum wave function.

Superconductivity has three hallmark properties. Below the transition temperature, superconductors have zero resistance and they screen magnetic field (the so called Meissner effect). The final hallmark is flux quantization. If a very large magnetic field is applied to a superconductor, the part that goes through the material is forced to go through in quantized bundles, called vortices. This trait relates to the fact that superconductors can be described by a single valued wave function, Ψ, that is a function of space and is characterized by magnitude and a phase $\Psi(x) = |\Psi(x)| \exp(i\phi(x))$. The phase at any location has a single value between zero and 2π. This implies that if you follow the phase around any normal metal region, the value of that phase must wind an integer number of times. Vortices correspond to one winding, each associated with one flux quantum of magnetic field. As we will see, rings can have more than one winding especially when a magnetic field is applied.

The Josephson equations describe how a change in the phase, ϕ, can create a voltage. Vortex motion across a superconductor is thus associated with voltage, or resistance. Similarly, it is the phase winding in the Josephson junctions of our SQUIDs that give us the voltage through which we measure magnetic field.

Fluctuations are important because they can make the hallmarks of superconductivity occur at a different temperature than the temperature predicted by the microscopic mechanisms for superconductivity in a given material. The Berezinsky-Kosterlitz-Thouless (BKT) transition is a good example of this: In sufficiently thin two dimensional superconductors, the BKT effect explains how thermal energy can create vortex-anti-vortex pairs, and how those pairs can become physically separated from each other in the superconductor. As the vortex pairs start proliferating and annihilating, the vortex motion causes resistance. The pair motion also means that relative phase is not well defined across the superconductor, and the superconductor is no longer very effective at screening magnetic field.

Fluctuation superconductivity was being worked out in the late 1970's, and early 1980's [54], but the focus of superconductivity research shifted dramatically when so called high temperature superconductivity (High-T_c) was discovered [7] on the eve of

1987. Interest in the field has increased again in the last ten years, because of the role superconducting fluctuations may play in the High-T_c phase diagram [26]. This is particularily true in the pseudo-gap regime where some form of superconductivity may exist but there is no global phase coherence or zero resistance.

This thesis focuses on one dimensional (1D) superconductors. In this case 1D implies the crossection of a superconductor is less than the penetration depth, λ, and the coherence length, ξ, each typically more than 100 nm in aluminum. In 1D, one only needs to consider variations along the linear dimension. Our rings are simply a one dimensional wire that is wrapped around on itself. The ring's 1D nature provides a simplified model system, with solutions that are theoretically tractable. Measuring a ring's response to magnetic field also access to certain thermodynamic properties that can not be accessed directly with standard resistance measurements.

Generally, we say fluctuations are important when one needs to consider multiple wave function solutions to describe the behavior of the system. In 1D wires, fluctuations are very important because solutions along the wire with different phase windings have nearly identical energies. Thermal energy can also induce a momentary weak point in the superconductor allowing the phase to change [53]. Since phase change gives voltage, 1D wires can have finite resistance well below the nominal critical temperature, and above T_c there are electron pair correlations along the wire, which makes the transition very broad. These effects have been studied to great length with transport measurements, with a large part of the recent work focussed on the nature of the phase slip initiation [10]. Relatively less work has been done at and above T_c.

In this thesis, I have studied the intimate relation between phase and amplitude in uniform rings. In chapter 5, I describe relatively long, dirty rings, where thermal energy can cause the population of multiple phase winding solutions reducing the ring's ability to screen magnetic field. In chapter 4, I discribe a range of moderately clean rings, where phase winding is so costly that superconductivity is destroyed (the Little-Parks effect), leaving a remnant fluctuation induced response above the reduced flux-dependent T_c. In chapter 6, I present work towards the realization of even cleaner rings, with both large and small amplitudes, where it may one day be

possible to observe quantum induced fluctuations.

The SQUID described in chapter 2 was designed and implemented by Martin Huber. My major contributions were in the development of the scanning technique, the interpretation of the fundamental noise sources, and to the formulation and writing of the paper. The SQUID described in chapter 3 was designed primarily by myself, with some design help and all of the optical fabrication done by Martin Huber. The FIB fabrication was done first in Jeff Large's group at Texas Instruments, and then later by myself at Stanford. Julie Bert did the initial screening of most of the devices, and aquired the noise data presented in figure 3.2g. The data in chapters 4, 5, and 6 was taken with a scanning microscope in the dilution refrigerator originally designed and implemented by Per Björnsson [11]. Hendrik Bluhm added the course motion and wrote much of the scanning and data acquisition software. Hendrik and I participated roughly equally in debugging the system, enhancing the ability to apply large currents, and reducing the system's noise. The samples for both of these experiments were made by myself, and I did almost all of the data interpretation, with the notable exception of the initial fluxoid fluctuation idea, which came from Hendrik. The bilayer idea, chapter 6, was originally suggested by John Price at the University of Colorado - Boulder. Sorting out the low-frequency noise components, appendix A, was done collaboratively with Jason Pelc, and the section on concepts for future SQUIDs, appendix B, benefited greatly from discussions with, and the ongoing design by John Kirtley.

Chapter 2

Gradiometric micro-SQUID susceptometer for scanning measurements of mesoscopic samples

Martin E. Huber, Nicholas C. Koshnick, Hendrik Bluhm, Leonard J. Archuleta, Tommy Azua, Per G. Björnsson, Brian W. Gardner, Sean T. Halloran, Erik A. Lucero and Kathryn A. Moler

Review of Scientific Instruments, **79**, 053704 (2008)

We have fabricated and characterized micro-SQUID susceptometers for use in low-temperature scanning probe microscopy systems. The design features the following: a 4 μm sensor loop; a field loop to apply a local field to the sample; an additional counter-wound sensor-loop/field-loop pair to cancel the background signal from the applied field in the absence of the sample; modulation loops to allow setting the SQUID at its optimum bias point (independent of the applied field), and shielding that minimizes coupling of magnetic fields into the leads and body of the SQUID. The design is highly symmetric to cancel the flux signal from uniform external fields. We use a SQUID series array preamplifier and obtain a system bandwidth of 1 MHz. The

flux noise at 125 mK is approximately 0.25 $\mu\Phi_0/\sqrt{Hz}$ above 10 kHz, with a value of 2.5 $\mu\Phi_0/\sqrt{Hz}$ at 10 Hz.

2.1 Introduction

The magnetic response of micro- and nano-scale objects, as a function of an applied magnetic field, reveals properties that cannot be probed directly by other methods. For instance, the current in a mesoscopic ring is the first derivative of the rings free energy with respect to magnetic flux, allowing for the study of fundamental thermodynamic properties [49]. The periodicity of the free energy with respect to the flux quantum allows for a variety of fluxoid physics, including the Little-Parks effect [56], multiple fluxoid transitions [17], and the detection of novel superconducting wave function states.[16] The intrinsic sensitivity of Superconducting Quantum Interference Devices (SQUIDs) to magnetic flux makes these devices some of the world's best instruments for measuring magnetic fields [21]. In this paper we present a scanning SQUID susceptometer that has enabled results [49, 17, 16] on micron scale objects in part because it is specifically designed to measure the response of small objects as a function of applied field.

Micro-SQUIDs excel at quantitative measurement of small magnetic signals, and scanning SQUID microscopy is often used for imaging.[47] Our devices have been used for such studies in the past [12], we emphasize design aspects that a scanning system can also be used to measure the total magnetic response to applied field (moment or susceptibility) of nanoscale objects, which has more traditionally been done with non-scanning sensors that may be integrated onto the same chip as the sample [59], require physical placement of a sample in the sensor loop [6], or in a static flip-chip geometry.[90] Use of a scanning sensor has multiple advantages for this purpose, allowing measurement of samples that are on different substrates or that can be fabricated by incompatible processes, as well as measurement of multiple samples in a single cool-down. Most importantly for the smallest signals, a scanning sensor allows in situ measurements of the background simply by moving away from the sample.

All SQUIDs have nonlinear current-voltage characteristics with a critical current that depends periodically on the total flux Φ through the SQUID loop with a periodicity of the superconducting flux quantum, $\Phi_0 = h/2e$. The smallest micro-SQUIDs fabricated to date are also the most basic, consisting of a simple superconducting loop with two Josephson junctions or microbridges [22, 52, 87]. The single-loop designs are hysteretic because they lack shunt resistors (in the case of tunnel junctions) or have intrinsic heating issues (associated with hot quasiparticles in microbridges). Because it is not possible to use a feedback circuit to keep the SQUID in a flux locked loop when there are no modulation loops, the response of simple SQUIDs is non-linear in applied field. In principle, shunt resistors and a modulation loop could be added, but in practice, it is difficult to fabricate shunt resistors into a small region and modulation loops have limited use because the modulation field is applied to the sample as well. Fabricating a sensor loop that is separate from the core area of the SQUID solves both of these problems.

SQUIDs with independent control of sample flux and bias flux allow for operation at the maximum-sensitivity bias point for all measurement fields. We have designed our device with separate sensor/field loops (for applying fields to the sample and measuring the sample's response) and modulation loops (for setting the flux bias of the SQUID). These two sets of loops are separated in space to reduce cross-coupling and are arranged as gradiometers to reduce coupling to external magnetic fields. Coupling the sensor loop directly to the main body of the SQUID through integrated coaxial leads [43] results in the scanning SQUID magnetometer design reported by Kirtley and Ketchen. Separating the sensor loop and the junction body also allows the sensor loop to be optimized for coupling to the sample.

In many cases, it is desirable to null the SQUID's response to the applied field so that the signal only reflects the magnetic response of the sample to the applied field. This can be done by including a separate, counter-wound sensor-loop/field-loop pair to cancel the applied field. Designs including such features are known as SQUID susceptometers and were first proposed and produced by Ketchen [43] and implemented in a scanning geometry by Gardner et al [28]. The previously reported design had 8 μm sensor loops and did not have a high degree of symmetry.

We report on the design, fabrication, and characterization of scanning SQUID susceptometers with 4 μm sensor loops, integral and robust shielding, and a high degree of symmetry. Section 2.2 will describe design considerations. Section 2.3 will describe the experimental configuration, including the scanning stage and pre-amplifier with which we could achieve the same intrinsic flux noise while scanning as while in a static, well-shielded environment. Section 2.4 will describe the flux noise optimization process and background cancellation technique. Section 2.5 will describe images taken by this device which will allow for the description of the pick-up loop imaging kernel and will describe the spin and ring-current sensitivities.

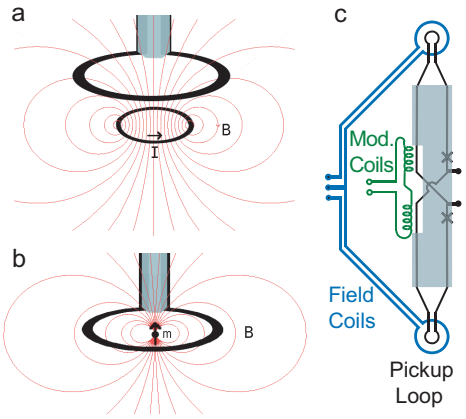

Figure 2.1: (a) Field lines (red) from a current I in a ring positioned on axis but slightly below the sensor loop (black), with shielding tab shown in gray. (b) Field lines (red) from dipole moment of a sample located at the center of a sensor loop (black). The inclosed flux increases as the loop diameter is decreased. The net flux also increase if the sample is moved toward the wire forming the sensor loop. (c) Simplified diagram of the device, showing the general relationship between the sensor loops, the field loops, and the modulation loops. The center-tap of the field coils allows compensation of lithographic imperfections between the two sensor loops. The blue/gray shading represents the low inductance planar coaxial shield on the susceptometer arms.

2.2 Design

SQUIDs are intrinsically sensitive to the magnetic flux threading their pickup area, thus the best field sensitivity is achieved with the largest pickup area compatible with a given application. While large SQUIDs have the best sensitivity to magnetic field, small SQUIDs have better coupling to small samples. Our 4 μm sensor loop size allows for a large pickup loop area relative to the lithographically-limited spacing between the pickup loop leads, allowing for an convenient scan-imaging kernel. It also allows for optimal coupling to micron-scale samples, such as rings, where fields $\lesssim$ 50 Oe (where vortices move in the SQUID) can apply several supercontucting flux quantum, Φ_0, through a given sample's center. When the sample's diameter is sufficiently small compared to the pickup loop size (Fig. 2.1a) the field lines can be approximated as an ideal dipole (Fig. 2.1b). When the dipole moment, m, is in the center of the pickup loop and aligned perpendicular to the pickup loop plane as shown, the magnetic flux captured by the sensor is $\Phi_{SQ} = mr_d/R$ where R is the radius of the ring, $r_{cl} = 2.8 \times 10^{-}15$ m is the classical electron radius, Φ_{SQ} is in units of Φ_0 and m is in units of electron spins, μ_B [41]. Qualitatively, smaller sensor loops allow fewer field lines to close within the sensor area, increasing the total magnetic flux threading the loop. The coupling decreases rapidly if the dipole is more than the pickup loop radius away from the plane of the sensor loop. Maximal coupling occurs when the dipole is directly next to the sensor loop itself, at which point, the Meissner screening associated with the sensor loop line-width can play an important role and more accurate modeling[40] is required to estimate an accurate spin sensitivity.

To measure the magnetic response of a sample as a function of applied field, the measurement process must cancel the sensor's response to the applied field itself. To aid this cancellation process, our susceptometer is designed with two, nominally identical, counter-wound sensor loops, separated by $\approx$ 1.2 mm on the sensor chip so that one loop can be located in close proximity to the sample while the other loop is far from the sample substrate to avoid unwanted coupling [Fig. 2.1c]. The symmetry of the design leads to both a geometric cancellation of a uniform applied field and a balanced inductance between the two arms of the SQUID, which leads to improved

electrical performance.

We apply field to the area near the two sensor loops with local single-turn field loops that are fully integrated into the SQUID chip layout. The inner diameter of each field loop is 10 μm, or approximately twice the diameter of the sensor loop, allowing for a mutual inductance of 2 pH or $\approx 1\ \Phi_0$/mA. The field at the center of the loop is approximately 1 Gauss/mA. Although the critical current of the field coil lines is $I_{FC} \approx 75$ mA, effective operation is limited to a range $I_{FC} \lesssim \pm 45$ mA due to the onset of vortex motion. The field loops are fabricated from a thin-film Nb layer deposited directly on the substrate so as to avoid edge crossings that might decrease the critical current of the lines. The vortex motion is thus likely to occur in one of the shielding layers as described the next section.

The two field loops are connected in series, so that a constant current applies the same magnetic induction to both sensor loops. A geometric imbalance of approximately 1 part in 100 is thought to be caused by lithographic imperfections. A center tap on the field loop leads allows one to cancel the residual geometric coupling between field loops and sensor loops to within 1 part in 10,000. At this level of cancellation, we are able to apply $\sim 40\ \Phi_0$ of field with a residual signal of only a few mΦ_0. This allows for sufficient dynamic range in the preamplifier/readout electronics to measure the residual background with the same sensitivity as we measure the signal itself.

The local field coils have three additional advantages when compared to a system which operates in a uniform field applied by an external solenoid. First, the integrated field coils have a comparatively low inductance which enables the possibility of oscillating the applied field at a high rate ($\sim$ 10 kHz), alleviating many of the problems associated with low frequency sensor noise. Second, because the field from the field coils falls off like $1/r^3$ when the distance from the sample, r, is larger than the field coil diameter, the coupling to the sample is proportional to $1/r^6$ (as opposed to $1/r^3$ for a uniform field). This allows for a more independent characterization of the SQUIDs response to the applied field *in situ* away from any sample. Finally, the local field coils allow for the modulation loops and Josephson junctions to operate in a low field environment.

Integrated modulation loops allow for operation in a flux locked loop. The feedback technique linearizes the response in the applied flux and allows the SQUID to operate at a flux bias point of optimal sensitivity [21]. The modulation loops are larger than the applied field loops, reducing the feedback current requirements, and thus the heating from stray resistances in the low temperature wiring. Although the modulation loops cancel off constant background fields with their gradiometric design, they are still highly sensitive to gradients in the applied field due to their large size, thus we find that scanning mount vibrations of approximately 25 nm magnitude limit the sensitivity of the system when it is operated in a field applied by an external solenoid.

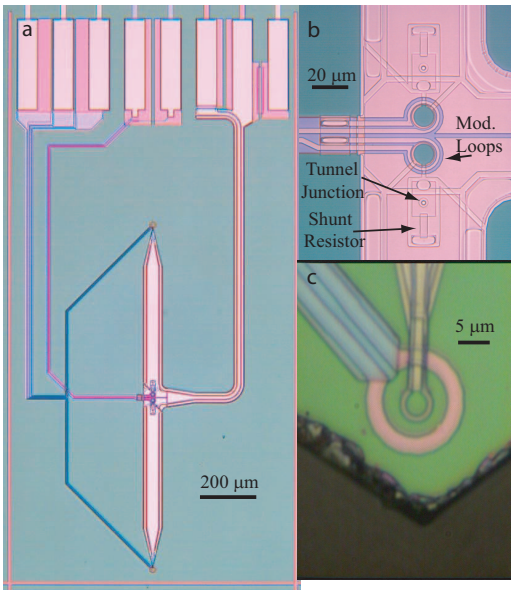

Figure 2.2: (a) Photomicrogaph of the full device, prior to polishing the tip. Pads for wirebonding are at the top. The distance between sensor loops is 1.2 mm. The field coil lines approach each sensor coil from a 45 degree angle to the axis; the modulation coils approach coupling loops in the center of the SQUID perpendicular to the axis. (b) Close-up view of the core area of the SQUID, including junctions, shunt resistors, and modulation loops. (c) Close-up view of the sensor area, after polishing. Note shielding layers above both the sensor loop leads and the field loop leads.

The gradiometric sensor loops and like-polarity field loops form the ends of a

symmetric common axis, the susceptometer axis, which extends 1.2 mm in length (Fig. 2.2a). The SQUID junctions and modulation loops are at the center of the susceptometer (Fig. 2.2b) placed symmetrically between the sensor loops/field loop pairs. The sensor loops are connected to the SQUID core by low-inductance planar coaxial lines that taper to a narrow point in the vicinity of the sensor loops (Fig. 2.2c). The SQUID bias leads extend perpendicularly from the susceptometer axis and are also realized as a planar coaxial structure. The modulation loop leads extend from the center of the susceptometer in the opposite direction from the SQUID bias leads.

The flux coupling geometry at the center of the susceptometer has been designed to allow one to couple external fields to a SQUID that is primarily a self-shielded planar transmission line. The key to the design is a conceptual twisting of the flux plane from the transmission line region (where its normal vector points along the susceptometer axis) to the modulation region (where the plane is that of the substrate) without excessive losses or excess inductances. Ketchen and Kirtley [41] have described the importance of shielding the sensor from parasitic coupling (through connecting leads and/or gaps between layers). We follow a similar design philosophy, taking advantage of improvements in lithography to reduce sharp corners by tapering the tip at a shallow angle. The field coils and the last 40 μm of the sensor loops are shielded by a superconducting tab.

The SQUID fabrication uses a conventional Nb/AlO_x/Nb trilayer Josephson junction technology, including PdAu shunt resistors, SiO_2 dielectric interlayers, and Nb wiring layers. The Nb and Al are deposited by dc sputtering in an Ar atmosphere, the PdAu resistors are deposited by electron-beam evaporation, and the SiO_2 interlayer is deposited by Electron Cyclotron Resonance Plasma Enhanced Chemical Vapor Deposition (ECR PECVD). A full description of this process is included elsewhere [72]. Device features were defined in an optical lithography process with approximately 0.8 μm minimum feature size (sensor loop wire width).

2.3 Experimental System

The field loop leads are oriented at a 45° angle to the axis of the SQUID so that the susceptometer may be polished to approximately 15 μm of the field coil so that the sensor loop is near the edge of the chip. The device is then fastened to a cantilever and aligned at an angle of approximately 2° with respect to the sample plane so that the sensor loop can be positioned in close proximity ($\sim$1 μm) to the sample. The cantilever movement is controlled by a large area scanning piezoelectric S-bender [77] with additional coarse motion control by stick-slip motion attocube positioners [1].

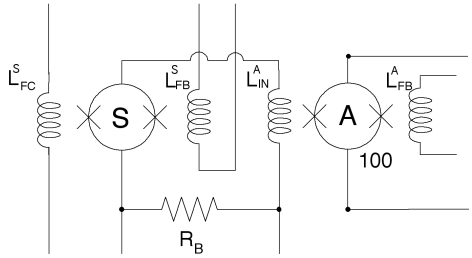

Figure 2.3: Circuit diagram for the device operation. Local compensated field coils apply magnetic field to the two ends of the SQUID susceptometer (S) with coupling $L^S_{FC} = 1.0\Phi_0/mA = 2.1$ pH . Modulation coils with $L^S_{FB} = 16\Phi_0/mA = 33$ pH allow for additional feedback (FB) circuitry to keep the device at an optimal working flux bias, while linearizing the response to an applied field. The susceptometer is voltage biased through $R_B \approx 100m\Omega$ and the SQUID current is coupled to a series array SQUID preamplifier (A) [36] with input inductance $L^A_{In} = 33\Phi_0/mA = 68$ pH. The flux bias of S is set through a offset voltage in the FB circuitry, and the flux bias of A is set through the mutual inductance $L^A_{FB} = 4.2\Phi_0/mA = 8.7$ pH.

We voltage bias the SQUID and read out the current with a SQUID array preamplifier to improve performance (Fig. 2.3). In many underdamped SQUIDs, resonances and/or hysteretic characteristics are observed when current biased, due to multiple stable voltage states that are present for a given current. The same devices are stable when voltage-biased. Voltage biasing is also more appropriate when using a low-input-impedance preamplifier such as a SQUIDor a SQUID array.

The advantage to using a SQUID series array preamplifier is that it's output

impedance is designed to couple well to room-temperature electronics. Thus, there is no need for an impedance-matching transformer that might limit the bandwidth. Moreover, the feedback circuit can be directly coupled, without use of a modulation frequency. We use a N = 100 SQUID series array [36] with an output impedance of $\sim 300\Omega$. When the array is operated in a magnetically shielded environment, a minimal amount of flux trapping occurs and the combined output from all of the SQUIDs is in phase, and thus adds coherently to the total signal. The input current sensitivity of the SQUID series array is approximately 2.5 pA/$\sqrt{Hz}$ with a 1/f knee at $\sim$ 50 Hz. This measured noise is less than the fundamental noise of the susceptometer.

2.4 Noise Design and Performance

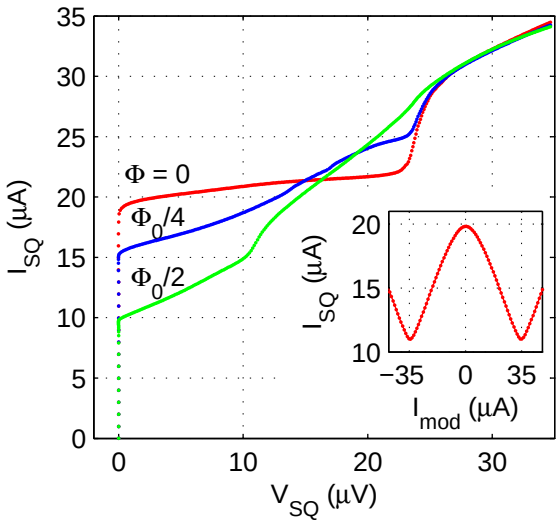

Figure 2.4: Current-Voltage characteristics of the SQUID at various flux bias points. Inset: SQUID current, I_{SQ}, as a function of the modulation loop current, I_Φ, flux Φ as coupled through the modulation coils.

In order to minimize the SQUID flux noise, we followed a design prescription [79] which sets the Josephson junction current, I_c, from the SQUIDself-inductance, L_{SQ}, with the relation $I_c = \Phi_0/2L_{SQ}$. Numeric modeling [40] was used to estimate the

inductance of individual SQUID components yielding: modulation core region, 55 pH, strip line, 9 pH/mm, tapper region, 4 pH , pickup loop, 13 pH. The combined inductance $L_{SQ} \approx 100pH$ agrees to within experimental uncertainty of the actual inducatance, as extrapolated [67] from the critical currents at applied flux values of $\Phi = 0$ and $\Phi_0/2$. The corresponding design $I_c \approx 10\ \mu$A agrees well with the measured Max$(I_c/2)$ as shown in figure 2.4a. Using the same design prescription, Shunted DC SQUIDs are non-Hysteretic when the parameter $\beta_C = 2\pi I_c R^2 C_J/\Phi_0 \leq 1$, where C_J is the capacitance of each junction. We report on our lowest resistance ($R_{SQ} = 1.2\Omega$) devices which have a non-hysteretic response and the measured noise performance. The choices give a design value of $\beta_L = 1$ and $\beta_C = 0.3$. The dynamic resistance under a common operating bias is approximately 3.5 Ω.

A bias resistor of approximately 100 mΩ is fabricated on the same substrate as the susceptometer. This resistor is not used at ultra-low temperatures where heat loading is an issue.

2.4.1 Measured Flux sensitivity

The frequency independent flux sensitivity of dc SQUIDs has been thoroughly analyzed with respect to design parameters [79]. Fig. 2.5b shows the "white" flux noise (as measured between 20 and 30 KHz) as a function of temperature for a typical device. One contribution to this noise is Johnson noise in the shunt resistors. This noise is minimized when $\beta_L \sim 1$ and $\beta_c = 1$, giving a theoretical limit [80] of $\Phi_n = \sqrt{S_\Phi} = (16 k_B T L_{SQ}\sqrt{L_{SQ}C_J})^{1/2}$. Above $0.5K$, the device noise has the same functional dependence on the temperature and is only slightly larger in magnitude than this limit, in accordance with the reduced β_c parameter. When the temperature is reduced below $0.5K$, the flux noise plateaus at a value higher than the quantum limit, and equivalent to the theoretical thermal saturation of the flux noise at 0.39 K. Other experimental data indicates that the device itself is nominally cooled to the control temperature, yet the noise is still excessive. The most likely cause of excess noise is the hot-electron noise in the shunt resistors as described by Wellstood [85], resulting from weak electron-phonon coupling at low temperatures.

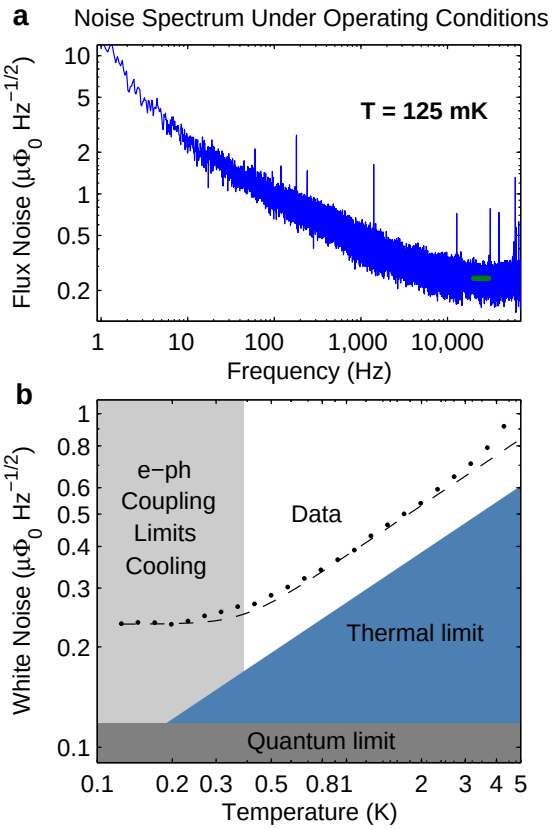

Figure 2.5: a) Noise spectrum (blue) observed in a functional scanning setup at 125 mK. The low frequency (1/f) noise is believed to be associated with the magnetic field of spins, as discussed in the text. The RMS white noise floor (green) is approximately 0.25 $\mu\Phi_0/\sqrt{Hz}$. b) White noise floor (points) as a function of temperature. The shaded areas represent the quantum and thermal noise limits for the optimal performance of a resistively shunted device with an inductance of 90 pH. The dashed line represents a fit to the thermal temperature dependence with the electron temperature limited by weak electron phonon interactions which set a which set a minimum electron temperature of 390 mK for our device parameters.

The 1/f-like low frequency noise is typically about 2 $\mu\Phi_0/\sqrt{Hz}$ at 10 Hz, and depends on frequency approximately as $\Phi_n \propto \sqrt{S_\Phi} = f^{-0.35}$ rather than $\sqrt{S_\Phi} = f^{-0.5}$. We have checked that it does not come from the SQUID series array or room temperature amplifier stages, and there is only very weak temperature dependence. Tests using a bias reversal scheme [21] indicate that this low frequency noise is true flux noise, rather than due to critical current fluctuations. Similar 1/f flux noise levels have been reported for other devices [86].

2.4.2 Bandwidth

The bandwidth of the array with an open-circuit on the input coil is greater than 100 MHz. In closed-loop operation, the bandwidth is limited by the room temperature electronics to approximately 5 MHz. In principle, the frequency response of the susceptometer is limited by the L/R time-constant of the SQUID array input inductance and susceptometer dynamic resistance. The measured bandwidth of the present arrangement (1 MHz) is consistent with measured values of L and R.

2.5 Imaging and Coupling to Mesoscopic Samples

Our sensor is designed to measure the weak magnetic signals from mesoscopic objects (Fig. 2.6). To locate these small signals, larger magnetic features must be included in the lithography. The sample in figure 2.6a includes aluminum rings and a gold meander wire to indicate each ring's position. Current through the grid of meander wires generates magnetic field that can be imaged with the susceptometer's pickup coil (Fig. 2.6b). Notches in the grid represent binary bits that differentiate one grid section from the next. Below the superconducting transition temperature for aluminum, the rings have a strong diamagnetic response to an applied field generated by the field coil (Fig. 2.6c). A higher resolution scan of a single ring (Fig. 2.6d) shows the imaging kernel of the sensor in susceptibility mode. The dark area around the ring represents a weak negative coupling when the ring is directly next to the pick loop and the returning field lines thread sensor area. The sensitivity to the

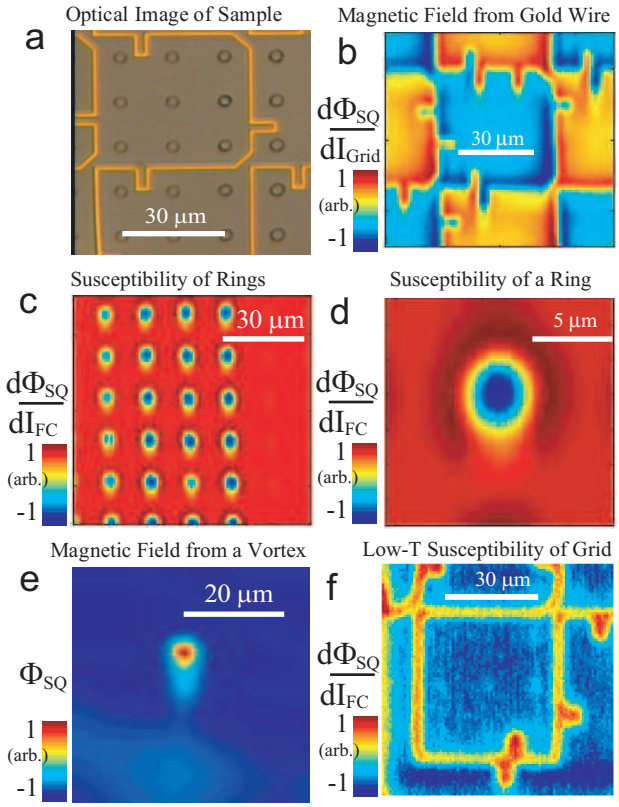

Figure 2.6: (a) Optical micrograph of a sample with aluminum rings and a gold meander wire. (b) Lockin measurement of current carried through the meander wire (different grid section). (c) Image of the rings' superconducting response to field applied from the field coils (susceptibility scan). (d) Higher resolution image of a single ring showing the sensors imaging kernel in susceptibility mode. (e) Image of a single superconducting vortex in niobium, demonstrating the magnetometry imaging kernel. (f) Susceptibility scan of the grid lines at ?? mK, which is consistent with a 100 ppm? spin response.

ring below the center of the scanned image represents flux threading the pickup loop leads. The magnetometry response of a vortex pinned in niobium thin film sample (Fig. 2.6e, zero applied field) represents typical response from a sharp feature with its own intrinsic magnetic moment. The region where flux leaks through the pickup loop leads represents a larger part of the "magnetometry kernal" as compared to the susceptometry mode, because samples with intrinsic field source produce a measurable signal outside of the area near the field coils. Figure 2.6f shows the response from a sample like the one shown in 2.6a but where the superconducting (Al) rings have been fabricated with normal metal (Au), and where a AlO_x insulator exists above the grid lines and below the rings. At the lowest temperatures ($\sim$ 30 mK) a paramagnetic susceptibility associated with spins in the metal and or this insulating layer[14] is visible after averaging times of a few to several tens of minutes.

Once a scanning technique has been used to identify a specific sample on a multi-sample substrate, the sensor can be used to make in situ background measurements, allowing for the aquisition of a full $I - \Phi$ curve. This procedure involves measuring the nonlinear SQUID response as a function of field (Fig. 2.7b) at various distances from the sample in question (Fig. 2.7a). We usually apply a sinusoidal current to the field coils in order to avoid high frequency components, which would be more affected by the finite measurement bandwidth. The counter-wound design leads to the initial two orders of magnitude of cancellation of the applied flux, as described above. After nulling the linear in-phase component of this response by feeding an adjustable current into the center tap, we typically find a residual signal on the order of 10^{-4} times the bare applied flux. This residual signal consists mostly of an out-of-phase component, which arises as the difference of two large signals of equal amplitude with a very slight phase shift. Particularly at a large applied field, a nonlinear component that we attribute to current induced pair breaking in or near the field coils becomes visible. To distinguish this sensor background from the much smaller sample signal, we measure it in situ by moving the pickup loop away from the sample and subtracting the result from that obtained when coupled to the sample. Our best results were obtained when moving the scanner on and off the sample parallel to the substrate, and measuring about 1 s at each position, so that the background susceptibility from the substrate is

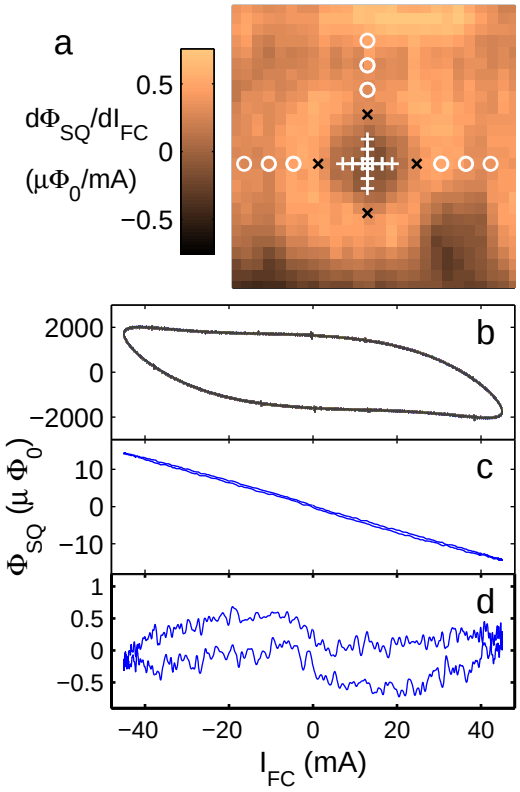

Figure 2.7: a) Lockin measurement of the SQUID response to current applied by the field coil. The cross marks are centered on the susceptibility response of a gold ring with a sample structured similar to 2.6a,e b) $\Phi_{SQ} - I_{FC}$ curves taken at the points indicated in part a. c) SQUIDresponse after the points centered over the ring (white plus marks) are subtracted from the response off the ring (white circles) as weighted by the SQUIDs response kernel. d) Subtracting the linear spin response leaves a non-linear response associated with non-equilibrium effects in the metal.

also eliminated, and slow variations in the sensor background are averaged out. With this procedure, we were able to obtain a nonlinear response of less than 0.1 $\mu\Phi_0$ at a field coil current of 35 mA (corresponding to about 35 Φ_0 or 35 G) after averaging for 38 hrs above a region of bare silicon substrate and subtracting the linear component. The latter was at least partly due to the susceptibility of nearby metal patterned on the substrate. Thus, we have achieved a cumulative background rejection of better than 8.5 orders of magnitude.

2.6 Conclusion

We have characterized a Nb high-symmetry scanning SQUID susceptometer between 0.025 K and 6 K. The spectral density of the flux noise in the frequency-independent region is 0.25 $\mu\Phi_0/\sqrt{Hz}$ below $\sim$ 200 mK. This device has better than 100 times greater spin sensitivity than our previous device, with more than 1000 times greater bandwidth. The improved performance is due to the reduced sensor loop dimensions, improved shielding, and improved symmetry with regard to the SQUID and field loop placement, and voltage biasing techniques on the readout stage. As expected, the limiting factor in bandwidth is set by the array input loop and the dynamic resistance of the SQUID susceptometer. The ability to position the sensor over multiple samples in a given cryogenic run and the ability to isolate the sensor from the samples for background subtraction combine to maximize the device utility and sensitivity.

This work was supported by the Packard Foundation and by NSF Grants No. DMR-0507931, DMR-0216470, ECS-0210877 and PHY-0425897. Some analysis was supported by Stanford's Center for Probing the Nanoscale (CPN), an NSF NSEC, NSF Grant No. PHY-0425897. We thank J. R. Kirtley and K. Irwin for useful discussions.

Chapter 3

A Terraced Scanning SQUID Susceptometer with Sub-Micron Pickup Loops

3.1 Our Sub-micron Terraced Susceptometers

Nicholas C. Koshnick, Martin E. Huber, Julie A. Bert, Clifford W. Hicks, Jeff Large, Hal Edwards, Kathryn A. Moler

Applied Physics Letters, Dec 15, 2008 [50]

Abstract

SQUIDs can have excellent spin sensitivity depending on their magnetic flux noise, pick-up loop diameter, and distance from the sample. We report a family of scanning SQUID susceptometers with terraced tips that position the pick-up loops 300 nm from the sample. The 600 nm – 2μm pickup loops, defined by focused ion beam, are integrated into a 12-layer optical lithography process allowing flux-locked feedback, in situ background subtraction and optimized flux noise. These features enable a sensitivity of $\sim$70 electron spins per root Hertz at 4K.

In 1989, Ketchen et al.[45] argued that the advent of sub-micron lithography should enable Superconducting Quantum Interference Devices (SQUIDs) with single electron spin sensitivity. Stationary devices can measure nanomagnets with great success [88], but it remains difficult, even with the highest spin-sensitivity SQUIDs [22], to detect single-molecule field sources. Scanning devices [84, 46, 64, 32, 27, 37] make it possible to isolate magnetic field sources and to perform background measurements in situ [49]. Single-layer scanning nano-SQUIDs [32] have not yet achieved the excellent flux sensitivity of the best large multi-layer SQUIDs. Multilayer SQUIDs thus far have had large pickup areas that do not capture dipole field lines well thereby limiting the spin sensitivity of these devices. For a normal-oriented dipole on the center line of a pickup loop of radius R, the spin sensitivity, S_n, is

$$S_n(\mu_B/\sqrt{\text{Hz}}) = \Phi_n \frac{R}{r_e}\left(1+\frac{h^2}{R^2}\right)^{3/2} \tag{3.1}$$

where Φ_n is the flux noise in units of $\Phi_0/\sqrt{\text{Hz}}$, h is the pickup loop's height above the sample, and $r_e = e^2/mc^2 \approx 2.8\times10^{-15}$ m [45]. On the center line, near-optimal signal is achieved for $h < R$. The spin sensitivity can be further improved by placing the dipole near the edge of the pickup loop, although demagnetization limits this enhancement for $h < w$, where w is the linewidth. For simplicity, we use Eq. 1 to compare representative published scanning SQUIDs (Table 1).

Our scanning SQUID combines Focused Ion Beam (FIB) defined pick-up loops with a 12 layer optical lithography process that includes local field coils. Integrated terraces minimize h. We characterize the imaging kernel with a superconducting vortex and a dipole field source. Flux noise measurements at 4 Kelvin demonstrate a spin sensitivity of $\sim$70 $\mu_B/\sqrt{\text{Hz}}$. Flux noise may decrease at lower temperatures (sections 2.4, 3.2) leading to a projected sensitivity of $\lesssim 15$ $\mu_B/\sqrt{\text{Hz}}$.

Our susceptometer incorporates two symmetric counter-wound arms, each with an integrated modulation loop, pickup loop, and local field coil (Fig 1a). A three metalization layer, linear coaxial transmission line geometry shields the device from

Table 3.1: Survey of reported scanning SQUIDs and estimated spin sensitivity for $h = 0$ (Eq. 3.1). Except [32], the corners are typically 20-60 μm from the pickup loop, likely limiting h to 1 – 3 μm. For rectangular loops we use $R = (l_1 l_2/\pi)^{1/2}$.

Principal Investigator	Year	Size μm^2	Flux Noise $(\mu\Phi_0/\sqrt{\text{Hz}})$	Spin Sensitivity $(\mu_B/\sqrt{\text{Hz}})$
van Harlingen [84]	1993	100	3	6,000
Kirtley [46]	1995	81	2	3,700
Morooka [64]	2000	16[1]	8	6,400[1]
Hasselbach [32]	2000	4	100	40,000
Hilgenkamp [27]	2006	12	2	1,400
Huber [37]	2008	12	0.80[2]	640[2]
Present Work	2008	0.3	0.68	73

[1] calculations from relevant line midpoints, [2] noise at 4 K

magnetic fields. The transmission line geometry has a low inductance per unit length (∼10 pH/mm), which allows for a large separation between the feedback/junction area and the two pickup loops without significantly increasing the devices theoretical white noise floor [79]. The separation permits the use of standard, well optimized junction and resistive shunt fabrication processes [72]. The resistive shunts ensure a non-hysteretic response. The scanning SQUID is voltage biased and its current is amplified with a SQUID Series Array (SSA) amplifier [36]. A feedback circuit controls the current in the modulation loop, responding to the SSA output voltage to create a flux locked loop. Feedback linearizes the signal and allows for optimal sensitivity at all applied fields. The counter-wound field coils aid background subtraction [37]. By applying a local field to the sample only in the area of the pickup loop, the field coils also allow for a low magnetic field environment near the junction, modulation, and amplification stages.

To achieve optimal flux noise [79], each junction's critical current, I_0, is approximately half the superconducting flux quantum $\Phi_0/2$, divided by the SQUID's self inductance, L. At 4 K, we have a 0.68 $\mu\Phi_0/\sqrt{\text{Hz}}$ noise floor above 100 Hz and 1.2 $\mu\Phi_0/\sqrt{\text{Hz}}$ 1/f-like noise at 10 Hz (Fig. 2f). If the dominant flux noise is Johnson noise in the shunt resistors, as indicated by $T^{1/2}$ temperature dependence in a previous similar device [37], a white noise floor of 0.25 $\mu\Phi_0/\sqrt{\text{Hz}}$ may be achievable at 300

mK (see section 3.2). Cooling fins attached to the shunt resistors of some devices to minimize the effect of electron-phonon coupling limited cooling may enable a white noise floor of 0.12 $\mu\Phi_0/\sqrt{\text{Hz}}$ at dilution refrigerator temperatures (see section 3.2).

When limited by Johnson noise in resistive shunts, the theoretical flux noise dependence scales like $L^{3/2}$, whereas quantum noise scales like $L^{1/2}$ [79]. The incentive for a well quantified low inductance adds to the criteria for optimal pickup loop design. When the width, w, or the thickness, t, of a superconducting feature become smaller than the penetration depth, λ, kinetic inductance can overcome the geometrical inductance contribution [18] and scales like $L_k \propto \lambda^2/wt$ [60]. Thus, linewidths smaller than λ are undesirable. This effect, along with phase winding considerations related to coherence length effects [31], ultimately sets the pickup loop size limit. Inductance also scales with feature length, so we have kept the sub-micron portion of the leads short, just long enough to allow the pickup loop to touch down first without excessive stray pickup.

For optimal coupling, a dipole on the center line of the pickup loop should have $h < R$, while a dipole near the edge of the pickup loop should have $h < w$. Fig. 1b shows a optically defined, w = 0.6 μm, R = 1.6 μm, pickup loop pattern with etch features inside and outside the field coil. The outer etch supplements hand polishing to bring the corner of the chip close to the field coil, and the inner etch reduces the oxide layer above the field coil. The thickness of the multiple layers are important parts of the design. In Fig. 1b, the pickup loop is under 250 nm of $Si0_2$ as required for a top layer of shielding (see section 3.2). It is thus at least this distance from the surface. The well created by the circular field coil allows little tolerance from the optimal alignment angle of 2.5 degrees (Inset Fig. 1b). Additionally, it is difficult to align the device such that the off-center field coil leads don't touch down first. While the SiO_2 layer and limited alignment tolerance is suitable for the w and R of the optically patterned design, these effects are detrimental for sub-micron pickup loops.

We explored several techniques to create superconducting sub-micron pickup loops integrated with the multilayer structure: ebeam defined lift-off lithography with Al, ebeam lithography for etching optically patterned Nb layers, and FIB etching of optically patterned Nb layers. The FIB etching was the most tractable. We also

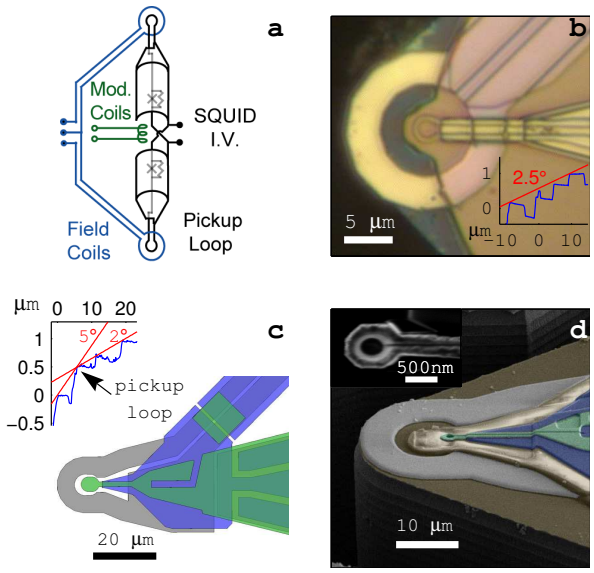

Figure 3.1: a) Diagram of a counterwound SQUID susceptometer. Both the optically patterned tips (b) and FIB defined tips (c, d) feature etch defined terraces that reduce the pickup loop to sample distance. Figure b, inset: AFM data down the center line of the device showing that the pickup loop is closest to the surface when the tip is aligned at precisely 2.5 degrees (more detail in section 3.2). In the FIB design (c), the thickness of the field coil and and pickup loop leads combine with the inner terrace to form a high centerline that allows roll angle tolerance. Figure c, inset: AFM data showing the pickup loop can touch down first when the pitch angle is between 2°-5°. Pickup loops down to 600 nm can be reliably fabricated with a FIB defined etch process of the topmost layer.

found that sputtered Nb has a smaller penetration depth (∼90 nm) than e-beam evaporated Al patterned with PMMA liftoff (∼120-160 nm), allowing for smaller linewidths and reducing the calculated [40] inductance for a pair of pickup loops (22 pH vs. 66 pH). The inductance of the rest of the design is 60-65 pH. Here, we only report results from optically and FIB defined Nb tips.

Our FIB design uses three superconducting layers (Fig 1c) such that the field coil lines (gray) run underneath a shielding layer (purple) and approach the tip from the same angle as the pickup loop. The pickup loop on the top layer (green) is closest to the sample, which also allows for post-optical FIB processing. This design allows the pickup loop to touch first when the SQUID is aligned to a pitch angle of 2° – 5°(Fig.

1c inset), with a roll tolerance equal to the pitch angle.

To increase durability, we fabricated some devices with the pickup loop retracted from the end of the etch-defined $Si0_2$ tab (Fig 1d), allowing the $Si0_2$ to take the brunt of the wear. The $Si0_2$ tab also overlaps with the inside edge of the field coil, making a high point that protects the pickup loop for pitch angles less than 2 degrees. The alignment angle is difficult to set accurately and can change due to thermal contractions, so these considerations are important for protecting the device.

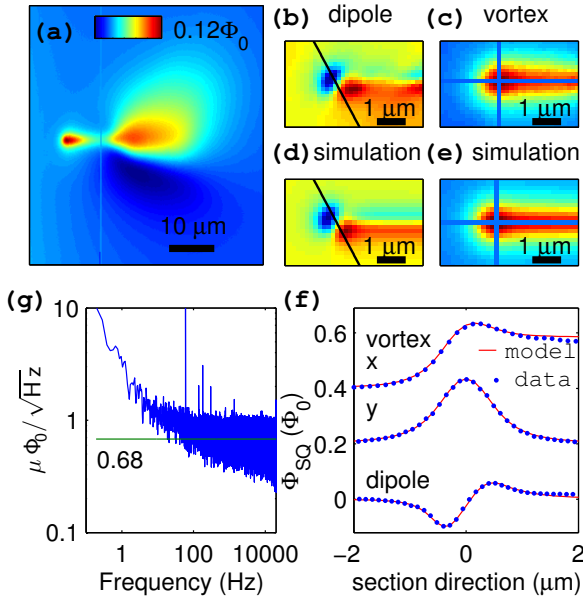

Figure 3.2: a) A FIB-fabricated device's magnetometry response near an isolated superconducting vortex. Both positive and negative flux coupling occurs near the leads to the pickup loop (shown on the right side). (b-f) data and modeled results for a pickup loop with a 500 nm inner diameter and 250 nm linewidth. The flux captured from an isolated surface dipole (b) and monopole magnetic field source (c) agrees with the modeled results (d,e) calculated by integrating the field lines that thread a pickup loop kernal located 400 nm above the surface. (f) Linescans of (b-e) offset for clarity. (g) Noise spectrum at 4 K. The green line shows the rms average between 5 KHz and 10 KHz.

We imaged Sr_2RuO_4 (Fig. 2) to characterize the FIB-defined device's coupling to a sample. Flux from a monopole-like superconducting vortex can couple through both the pickup loop and its leads (Fig. 2a). Our smallest SQUIDs are designed to do comparative studies on and off a particular mesoscopic structure, rather than

provide a point like imaging kernel.

Fitting a simple model of the pickup loop response to the vortex and dipole (Fig. 2b-g) gives an effective h. The vortex model is a monopole field source one penetration depth ($\lambda_{Sr_2RuO_4} = 150$ nm) below the surface [46]. The dipole model is a free-space dipole field source at the surface. The field from each of these two sources is integrated over the effective pickup loop area at an effective height $h_{eff} = 400$ nm. This h_{eff} implies that the closest side of the 200 nm thick pickup loop is 300 nm above the scanned surface. Several effects could make this estimate of h larger than the physical distance from the sample, such as the existence of a Meissner image dipole, $\lambda_{Sr_2RuO_4} >$ 150 nm due to dead layers or finite T, and demagnetization effects from the thickness of the pickup loop.

In conclusion, we have demonstrated SQUIDs with 0.68 $\mu\Phi_0/\sqrt{\text{Hz}}$ flux noise at 4 K, reliable FIB pickup loops with diameters as small as 600 nm, and a terraced geometry that allows the pickup loop to come within 300 nm of the surface. These features give a spin sensitivity of $\sim$70 $\mu_B/\sqrt{\text{Hz}}$, that is, the device noise is equivalent to the signal from a single electron spin after an averaging time of a little more than one hour. At lower temperatures a lower flux noise is likely, leading to spin sensitivities less than $15\mu_B/\sqrt{\text{Hz}}$.

3.2 Supplemental Material"

This section is also posed as EPAPS Document No. E-APPLAB-93-013850 (available at `http://www.aip.org/pubservs/epaps.html`).

This supplementary material explains the focused ion beam fabrication process, layer thickness effects, and the possible effects of the shunt-resistor cooling fins.

3.2.1 FIB fabrication

The Focus Ion Beam (FIB) etch process was optimized at Texas Instruments circuit design and repair lab with single beam (ion beam only) machines. The images shown in Fig. 3.3 were taken at Stanford using a dual beam, SEM and ion beam, machine. After etching, 15 of 17 devices continued to work with modulation depths and symmetry properties similar to their pre-tested values indicating no substantial change in the devices' inductance [67].

3.2.2 Layer Thickness Effects

Our fabrication steps did not include a planarization process between the various layer depositions and etches. The geometric effects created by multiple layer crossings can therefore be significant. We have used this to our advantage to optimize the touch down properties of the tip as described in the main text and in Fig. 3.4a-d. The graphical representation of the layers in b, d, and e do not demonstrate that the etch-defined walls are not vertical. Therefore layers that appear to be discontinuous in b and d are usually connected by material that extends over the side walls.

Because we did whole-wafer processing at NIST, we were not constrained to standard layer thicknesses or by the requirements of other devices. We processed two wafers with the thicknesses listed in Table 3.2.

The values for wafer W46, shown in Fig. 3.4b, were chosen to further enhance the alignment tolerance made possible by the new design. While this increase in the the touchdown tolerance angle was not required, most of the FIB work was nevertheless done on devices from this wafer because there was less over-etch on the W2 layer. This left a comparatively wide pickup-loop-to-SQUID-body stem, which was easier to FIB (ie. the process shown in Fig 3.3c). Conversely, most of the 3 and 4.6 μm SQUIDs were from wafer W47. This was because many of the optically defined devices on W46 lost their field coils during during an ultra-sound cleaning step.

The thicknesses for wafer W47 were used to construct Fig. 3.4d. The W47 thicknesses were chosen to be similar to the previous device [37] in order to reduce the chance of open and short circuits that can occur at layer crossings. The one

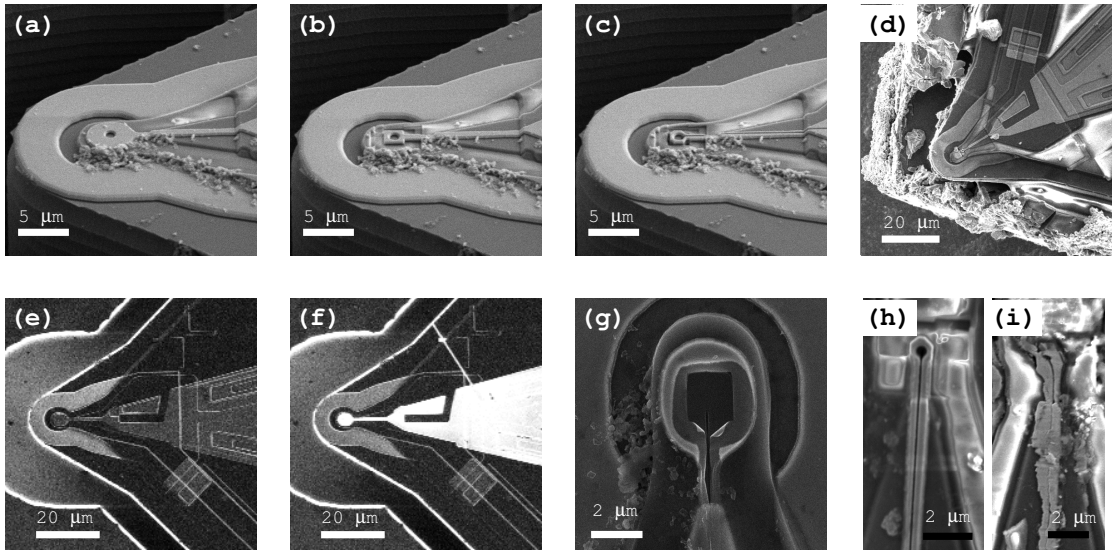

Figure 3.3: Pickup loop structures were milled from an optically patterned Nb tab. (a) A FIB drilled hole creates the center of the pickup loop. (b) Successive steps shape the outside of the pickup loop. (c) Leads are created by milling the center of the optically-defined stem, which connects the circular pickup loop to the rest of the SQUID. The pickup loop center is re-milled to remove redeposited material. (d) The device chip is polished to a corner defined by an optically patterened trench, which allows the active area of the device to touch first. (e,f) Before milling, a Pt strap is connected to the degenerately doped Si trench in order to increase the top layer's visibility. This process allows the etch-stop point to be identified *in situ* while milling. The Pt strap is subsequently milled away. (g) SEM of a pickup loop that was milled in the presence of XeF_2 gas to increase the etch rate and reduce the re-deposition. We found that this process continues to etch the Nb after the intended exposure over a period of many minutes. This effect is apparent in the distance between the inner square, which represents the intended etch area, and the outer circle. This image also shows the result of over-etching the SiO_2 layer, which leading to SiO_2 peeling (bottom of inner square). To avoid wuch corrosive effects, later etches were done in without XeF_2. (h) We could reliably make structures with line widths of ~ 200 nm, limited only by Ga implantation effects [81] and the superconducting penetration depth. When compared to previous pickup loop structures that remain under oxide layers, these top layer structures show increased sensitivity to both mechanical contact (i) and electrostatic shock.

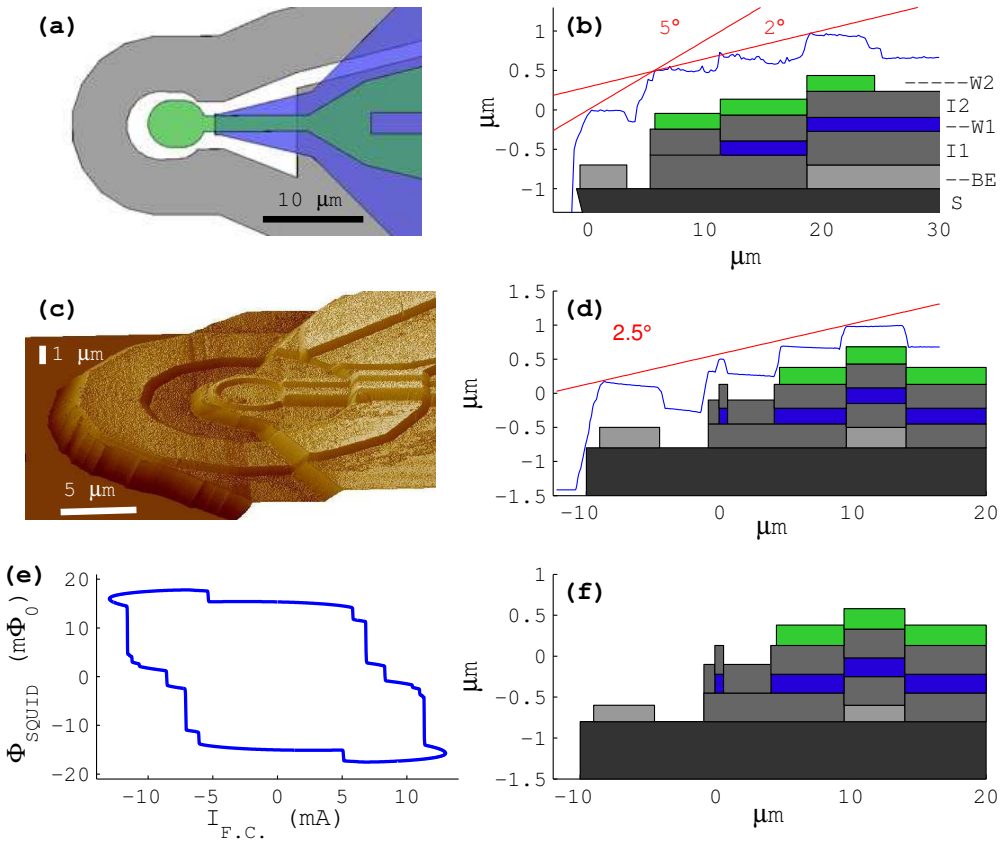

Figure 3.4: (a) Diagram of the three optically-defined superconducting layers before the final FIB milling step. (b) AFM data showing a cross section along the center line of the SQUID with a graphical representation of the substrate (S), superconducting layers (BE, W1, W2), and insulating layers (I1, I2) that create the steps. The layer crossings and etches are designed in such a way that the top layer pickup loop can touch first if the alignment angle is between 2° and 5°. (c) AFM data showing a 4.6 μm optically defined SQUID with an etched terrace similar to the 3 μm discussed in the main text. (d) AFM data and the corresponding layer diagram along the direction of one of the pickup loop leads. The pickup loop is closest to the sample when the device is aligned at an angle of 2.5°. The top layer is used as a shield to make a smaller magnetometry imaging kernel. When imaging items of the pickup loops 4.6 μm size, the increased scan height caused by the lack of alignment tolerance, and buried (middle layer) pickup loop is not significant. Therefore this device is well optimized for imaging micron scale samples. (e) SQUID response as a function of field coil current in a 3 μm device. Flux jumps reproducibly occur at certain values of $I_{F.C.}$. (f) Diagram demonstrating how a 200 nm base electrode layer (as used in previous devices [37]) allows for more contiguous upper wiring layers, as compared to the 300 nm base electrode line (b,c) used in this generation of devices.

Table 3.2: Layer thicknesses of the two processed wafers.

Wafer	Counter Electrode (CE)	Base Electrode (BE)	Resistors	Insulator one (I1)	Wiring one (W1)	Insulator two (I2)	Wiring two (W2)
W46	120 nm	300 nm	150 nm	425 nm	180 nm	330 nm	200
W47	120 nm	300 nm	150 nm	350 nm	230 nm	350 nm	250

exception was that the base electrode thickness was increased from 200 to 300 nm to help increase the maximum field coil current, $I_{F.C.}^{max}$. The width of the field coil lines was also increased. While these changes allowed $I_{F.C.}^{max}$ to increase from $\sim$ 75 mA to $\sim$ 135 mA, the current where vortices begin move, $I_{F.C.}^{vjump}$, went from $\sim$ 45 mA to as little as 6 mA (Fig. 3.4e). Above $\pm$13 mA, the vorticies jump at irregular field values, making the careful comparison of magnetization curves between two points on or off the sample difficult. To the extent that precise magnetization curves [49] are an important design goal, future design improvements should focus on increasing $I_{F.C.}^{vjump}$ rather than $I_{F.C.}^{max}$. While many effects can cause a low $I_{F.C.}^{vjump}$, we expect the reduced value may be caused by discontinuities created by the 300 nm base electrode layer, as portrayed by the difference between Fig. 3.4d and Fig. 3.4f. The value of $I_{F.C.}^{vjump}$ was similar for both W46 and W47.

3.2.3 Cooling fins

As discussed in the main text, the dominant noise source in our design is expected to be Johnson noise in the shunt resistors. At low temperatures Joule heating from the SQUID bias current can saturate the electron temperature of the resistors, and thereby saturate the device's white noise floor above the quantum and the thermal limits. In this case, cooling is most likely limited by the relatively weak electron-phonon coupling interactions [85]. To address this potential limitation, we have added cooling fins to our shunt resistors to increase the volume where electron-phonon interactions can occur, Fig. 3.5a. The cooling fins increase the normal electron volume by more than a factor of one thousand allowing the minimum theoretical electron temperature to go from 392 mK to 135 mK, Fig. 3.5b.

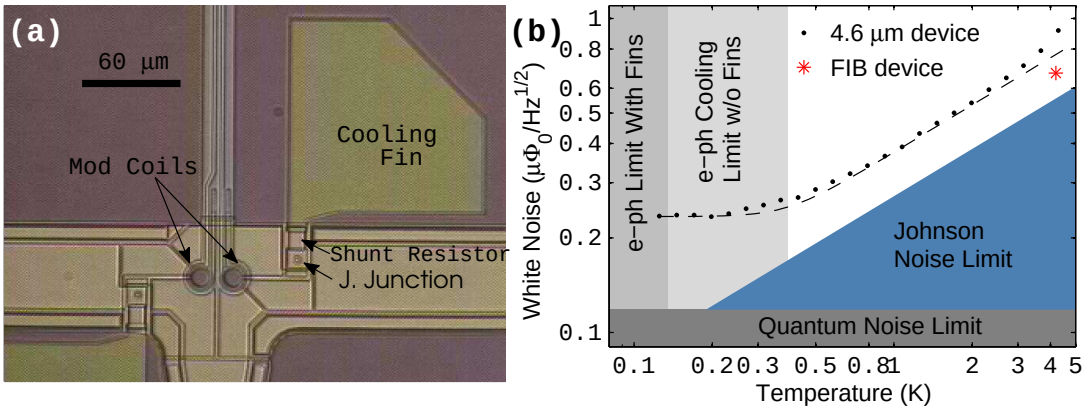

Figure 3.5: (a) An optical micrograph of the SQUID core, which includes Josephson junctions, shunt resistors, and modulation coils. The design improves on our previous work [37] by adding cooling fins to help dissipate the heat generated in the shunt resistors by increasing the volume where electrons and phonons can thermalize. (b) A reproduction of the white noise of an earlier device [37] as a function of temperature, and the 0.68 $\mu\Phi_0/\sqrt{Hz}$ noise from one current generation device at 4.2K. The lower right shaded areas represent the Johnson and quantum noise limits [79], given the relevant device parameters. The left hand shaded areas indicate the e-ph limited cooling limits with and without cooling fins when a 1.2 Ω shunt resistor is heated by 9 μA of current.

The cooling fins must be well coupled to the shunt resistors so that thermal gradients do not limit the desired effect. One can obtain a back-of-the-envelope estimate for such a gradient by using the Wiedeman-Franz law. From this law at a base temperature of 0.1K, 200 pW of power in a resistor (10 μA through 2 Ω) generates a thermal gradient of $\sim$ 0.1K when the resistance between the shunt resistor and the main part of the cooling fin, R_c, is 1Ω. This gradient scales approximately linearly with R_c. The shunt resistors were designed to be less than 0.5 squares away from to the cooling fins in order to make the thermal gradient less than 0.1 K. Both the resistors and the cooling fins are made from a PdAu layer with $R_{\square} \sim 2\Omega$. The cooling fins were fabricated directly on top of the silicon wafer to maximize thermal conductivity to the substrate.

Chapter 4

Fluctuation Induced Superconductivity in Mesoscopic Aluminum Rings

4.1 Fluctuation Superconductivity in Mesoscopic Aluminum Rings

Nicholas C. Koshnick, Hendrik Bluhm, Martin E. Huber, Kathryn A. Moler,
From *Science*, **318**, 1440-1443 (2007)
Reprinted with permission from AAAS.
Modified slightly to use the available space for clarity.

Abstract

Fluctuations are important near phase transitions, where they can be difficult to describe quantitatively. Superconductivity in mesoscopic rings is particularly intriguing because the critical temperature is an oscillatory function of magnetic field. There is an exact theory for thermal fluctuations in one-dimensional superconducting rings, which are therefore expected to be an excellent model system. We measure the susceptibility of many rings, one ring at a time, using a scanning SQUID that can isolate

magnetic signals from seven orders of magnitude larger background applied flux. We find that the fluctuation theory describes the results and that a single parameter characterizes the ways in which the fluctuations are especially important at magnetic fields where the critical temperature is suppressed.

Superconductivity requires both electron pairing and the coalescence of the pairs into a macroscopic quantum state with long-range phase coherence, usually described as a single wavefunction. In restricted geometries, thermal energy allows contributions from multiple wavefunctions to dramatically change the behavior of the system [26, 51, 53]. Experimental knowledge of fluctuations in 1D is largely derived from transport measurements [55], which can alter the state of a mesoscopic sample: generating measurable voltages may induce non-equilibrium dynamics, and leads on the sample introduce proximity effects over the length scale of the temperature-dependent Ginzburg-Lanau (G-L) coherence length, ξ. We use a contact-less technique to study isolated, quasi-1D rings with a contact-less technique that allows us to measure fluctuation effects on length scales that are comparable to and smaller than $\xi(T)$.

Using a scanning micro-Superconducting QUantum Interference Device (SQUID), we detect the persistent currents in many quasi-1D aluminum rings, one ring at a time, paying particular attention to small currents near each ring's superconducting transition temperature, T_c. Although the magnetic signals are small, such measurements have many advantages in principle. In 1D, the current about a ring, I, is related to the free energy, F, via $I = -\partial F/\partial \Phi_a$, where Φ_a is the flux threaded through the ring by an applied magnetic field. Measuring I as a function of Φ_a thus allows us to test a fundamental thermodynamic variable and our understanding of the ring's state. If the superconducting condensate is coherent about the ring's circumference L, the ring's current near zero applied field is proportional to the density of pairs. Deviations from such mean field solutions provide information about amplitude and phase fluctuations in the ring. Because the kinetic energy is related to the applied flux, it can be tuned externally, which can lead to additional fluctuation effects.

The mean field solution to G-L theory predicts that the persistent current near zero applied field should decrease linearly to zero as the temperature, T, approaches T_c. For small rings, we find a measurable persistent current above T_c, a quantitative and calculable signature of fluctuations. The quasi-1D geometry allows a full numeric solution of non-Gaussian thermal fluctuations in a G-L framework [73, 83], which is not possible in higher dimensions. Previous results on a single ring at zero applied field [90] found a fluctuation current that was larger than that current [83] by more than a factor of ten. We studied fluctuations in 15 rings, and found that 13 rings agree quantitatively with a full numeric solution, which was numerically intractable in the full range of interest for the parameters of the other 2 rings (see section 4.2.2).

The results in an applied field are particularly interesting. Little and Parks [56] showed experimentally that T_c varies as a periodic function of Φ_a. At half-integer multiples of the superconducting flux quantum, Φ_0, the energetic cost of maintaining the flux-induced supercurrent can be larger than the condensation energy, and superconductivity is destroyed. Previous results [58, 71, 33] indicate qualitatively that fluctuations may be especially important in this regime but were not compared quantitatively with theoretical predictions. We find an enhanced response at $\Phi_a = \Phi_0/2$ that can be quantitatively explained by G-L thermal fluctuations and demonstrate that a single parameter can characterize the Gaussian and non-Gaussian regimes, and determines where the Little-Parks effect is entirely washed out by fluctuations.

Unlike stationary sensors, a scanning sensor (Fig. 4.1) can measure many samples during a single cool-down. We report measurements on rings with radii R = 0.35, 0.5, 1, and 2 μm, annulus widths w from 65 to 180 nm, and thickness d =60 nm. The scanning SQUID also allows excellent background cancellation (12). After background subtraction, the signal (Fig 4.2) is proportional to current in the ring.

Many of the features in Fig. 4.2 can be explained with the mean field response obtained by the minimization of a 1D G-L functional. This process gives an expression

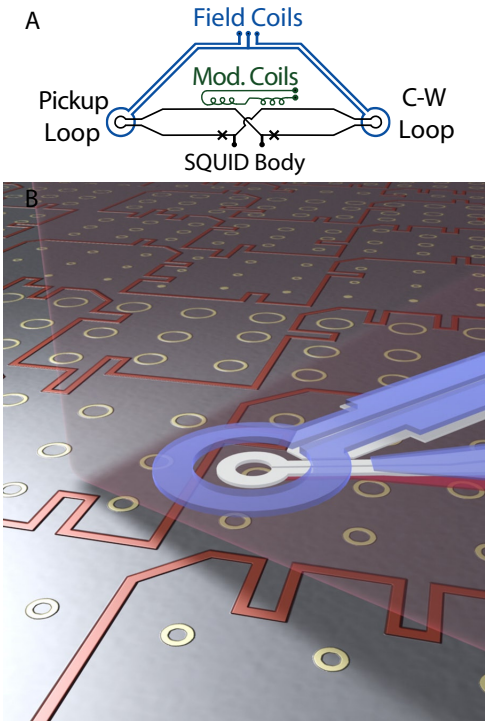

Figure 4.1: **A:** Diagram of the DC SQUID susceptometer. One field coil applies a local field to the sample, whose response couples a magnetic flux into the 4 μm pickup loop. A second counter-wound (C-W) loop compensates the sensor response to the applied field to within one part in 10^4. Additional modulation coils maintain the optimum working point. **B:** The SQUID chip's pickup loop (white) and field coil (blue) are positioned over a single micron-scale aluminum ring. *In-situ* background measurements allow the magnetic flux induced by currents in the ring to be unambiguously distinguished from the applied field, which is up to seven orders of magnitude larger.

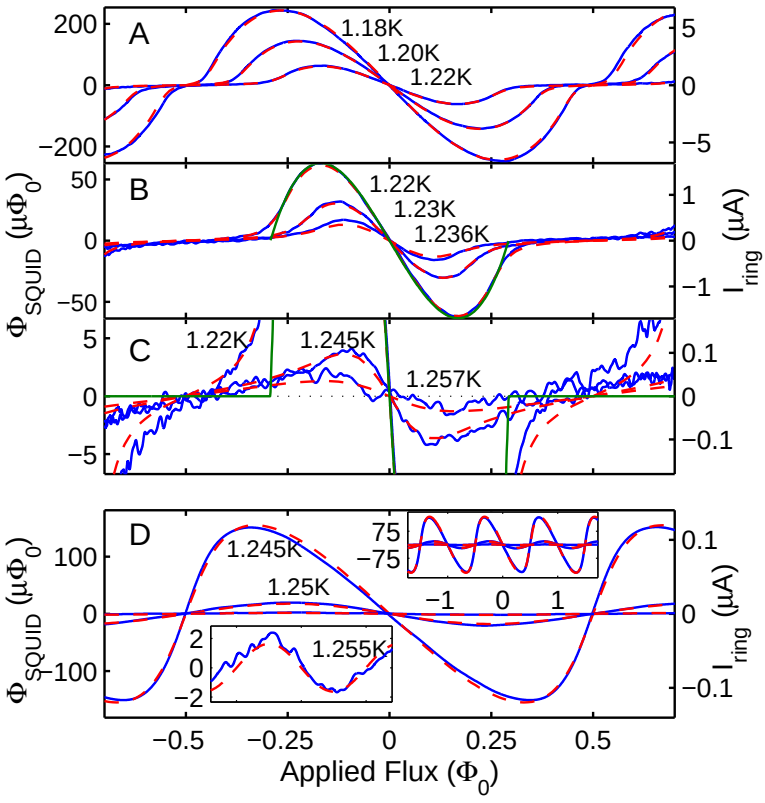

Figure 4.2: SQUID signal (left axis) and ring current (right axis) as a function of applied flux Φ_a for two rings, both with thickness $d = 60$ nm and width $w = 110$ nm. The fluctuation theory (dashed red) was fit to the data (blue) through the temperature analysis shown in Fig 4.3. **A-C** Radius $R = 0.35\ \mu m$, fitted $T_c(\Phi_a = 0) = 1.247$ K, and $\gamma = 0.075$. The green dashed line is the theoretical mean-field response for $T = 1.22K$ and shows the characteristic Little-Parks lineshape, in which the ring is not superconducting near $\Phi_a = \Phi_0/2$. The excess persistent current in this region indicates the large fluctuations in the Little-Parks regime. **D** Radius $R = 2\ \mu m$, fitted $T_c = 1.252$ K, and $\gamma = 13$. The periodic response (right inset) shows a 1D treatment is appropriate and can be approximated by a thermal average over mean field G-L fluxoid states (eq. 4.2 and section 4.2) until addition fluctuations contribute near T_c.

for the current in the ring [90],

$$I_n = -\frac{1}{\lambda^2}\frac{wd\Phi_0}{L\mu_0}(\Phi_a/\Phi_0 - n)P, \tag{4.1}$$

$$P = \min\left(1 - \left(\frac{2\pi\xi(T)}{L}\right)^2(\Phi_a/\Phi_0 - n)^2, 0\right), \tag{4.2}$$

where $1/\lambda(T)^2$ represents the superfluid density and n is the phase winding number imposed by the single-valuedness of the macroscopic wave function. The dependence on $\Phi_a/\Phi_0 - n$ makes the overall response periodic in Φ_0 (right inset Fig 4.2D), as the state with the lowest free energy is obtained when n is the nearest integer to Φ_a/Φ_0. The Φ_a-linear term is the London response where $1/\lambda^2 \propto T_c - T$ below $T_c(0)$ in the temperature range of interest, and 0 above $T_c(0)$. P describes pair-breaking due to an Aharonov-Bohm phase around the ring, which leads to a downturn of the response at finite field when $\xi(T) \gtrsim R$. In small rings, this effect occurs well below $T_c(0)$ (Fig. 4.2A-C). The Little-Parks effect occurs in the temperature range where, bringing P to zero for a range of applied flux. The dashed green line in Figs 4.2C, D shows the best match to eq. 4.2 at 1.22K. The data's large remnant response in the region in which the mean field curve vanishes is a clear demonstration that fluctuation effects are important in this regime. In large rings (Fig 4.2D), fluctuations dominate the response before the effect of the pair-breaking term is apparent.

For a quantitative comparison with theory [83], we evaluate the contribution of all possible wavefunctions, ψ, weighted according to their G-L energy, $E[\psi]$, to the mean current $I \equiv -\partial F/\partial\Phi_a = k_B T\frac{\partial}{\partial\Phi_a}\ln Z_{sc}$. The superconducting partition function, Z_{sc}, is the path integral over all possible wave functions: $Z_{sc}(\Phi_a) = \int \mathcal{D}\psi\mathcal{D}\psi^* \exp(E[\psi]/k_B T)$. Using the transfer operator technique [73], the evaluation of Z_{sc} for a 1D ring [83] can be transformed into a quantum mechanical eigenvalue problem, which allows for a numerical evaluation that is exact up to truncation errors. The flux-dependent terms can be separated, so that one obtains $Z_{sc} = \sum_{l=-\infty}^{\infty}\exp(-i2\pi l\Phi_a/\Phi_0)\sum_{n=0}^{\infty}\exp(-\gamma^{1/3}\mathscr{E}_{n,l})$ where $\mathscr{E}_{n,l}$ are the eigenvalues of the 2D single-particle Hamiltonian, $H = -\frac{1}{2}\nabla^2 +$

$\frac{4\pi}{\gamma^{2/3}}\left(\frac{T-T_c}{E_c/k_B}\right)\bar{r}^2+\frac{1}{4}\bar{r}^4$. We have rewritten these equations from the expression in reference [83] to emphasize the parameter

$$\gamma \equiv \frac{42\zeta(3)}{\pi}\frac{1}{M_{\rm eff}}\frac{k_B T_c}{E_c} \approx \frac{.87}{M_{\rm eff}}\frac{L^2}{\ell_e \xi_0}, \tag{4.3}$$

where $E_c = \pi^2\hbar v_F \ell_e/3L^2$ is the correlation or Thouless energy, ζ is the Riemann zeta function, v_F is the Fermi velocity, and ξ_0 is the Pipard zero temperature coherence length. The annulus width w and thickness d enter into the effective number of channels, $M_{\rm eff} = (\ell_e/L)\ (k_F^2 wd/4\pi)$, where k_F is the Fermi wavelength. This combination of parameters characterizes the size of the ring. Temperature only enters into the problem through the prefactor in the second term of the Hamiltonian, which can be rewritten using $8\pi\frac{T-T_c}{E_c/k_B} = \frac{L^2}{\xi(T)^2}$ to illustrate the relation to the pair-breaking term of Eq. 4.3, and indicate the region where $T > T_c(\Phi_a = \Phi_0/2)$ in Fig 4.3C. Thus, once the correct E_c and T_c are known for a given ring, the current as a function of Φ_a/Φ_0 and T is entirely determined by γ. We will discuss the dependence of the fluctuation response on γ after describing the way we fit our data to the model.

The data points in Fig 4.3 were derived from I-Φ_a curves (e.g., Fig 4.2) by fitting low order polynomials around the field symmetric points $\Phi_a = 0$ and $\Phi_a = \pm\Phi_0/2$. We have compared these susceptibilities as a function of temperature dependence to the theory using the measured geometry factors, the k_F and v_F for bulk aluminum, and three parameters, chosen by hand: ℓ_e, T_c, and M_{S-R}, the mutual inductance between the SQUID and the ring. ℓ_e is identified by the shape of the curve as a function of temperature, M_{S-R} is determined by the magnitude of the response, and T_c is chosen to allow the theory to match the linear temperature dependence of the $\Phi_a = 0$ susceptibility below T_c. The T_c of the rings we have considered varied from 1.237 to 1.268 K with up to 7 mK difference for nominally identical line-width rings. The fitted M_{S-R} lie within 15% of the inductance calculated with a model based on a 0.75 μm ring – sensor-loop separation. The fitted varies between 14 and 25 nm with an increasing dependence on line-width. We attribute this dependence to oxygen absorbed during the fabrication process and, to a lesser extent, the observed 20% variations in w (see section 4.2). The 4 fits shown in Fig 4.3 all have $\ell_e = 19.5 \pm 0.5$

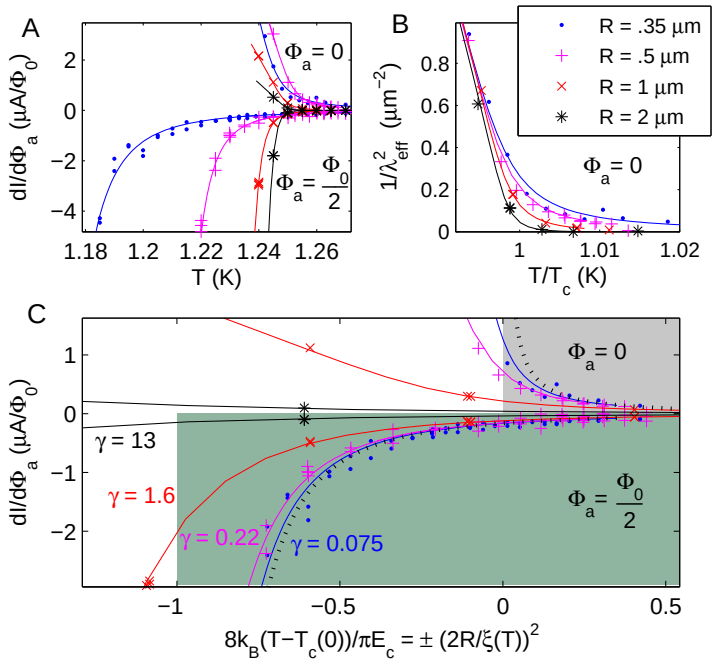

Figure 4.3: Susceptibility data (symbols) and fits (lines) at $\Phi_a = 0$ (positive values) and $\Phi_0/2$ (negative values) for 110 nm wide 60 nm thick rings with various radii, R. **A** Smaller rings have a larger temperature region where the Little-Parks criterion $\xi(T) > 2R$ is satisfied, and thus have a larger region with a reduced $\Phi_a = \Phi_0/2$ response. **B** $\Phi_a = 0$ susceptibility scaled with the cross section and radius to show the effective mean field superfluid density around T_c. Smaller rings have an enhanced fluctuation response. **C** When the temperature is scaled by the correlation energy E_c, the susceptibility is uniquely determined by the size parameter γ. The grey and green shaded regions indicate the temperature above $T_c(\Phi_a)$ for $\Phi = 0$ and $\Phi_0/2$, respectively. The fluctuation response above $T_c(\Phi_a)$ is clearly enhanced for $\Phi_a = \Phi_0/2$. The dotted line shows a Gaussian prediction (see section 4.2) that is valid at some γ-dependent temperature above $T_c(\Phi_a)$. When $\gamma \gtrsim 1$, the response at $\Phi_a = 0$ and $\Phi_0/2$ are comparable in the Little-Parks regime, which corresponds to a fluctuation dominated sinusoidal $I - \Phi_a$ response.

nm. The agreement with the 1D models we have discussed demonstrates that the finite line-width effects are not essential to our physical result and that small variations in w do not qualitatively change the response above $T_c(\Phi_a)$.

Near $T_c(\Phi_a)$, γ characterizes the non-Gaussian fluctuations that interpolate between the mean field behavior far below T_c and the Gaussian fluctuations that dominate at high temperatures. Non-Gaussian fluctuations are important when quadratic expansions of the free energy cannot describe the physical result. This is particularly apparent at $T_c(\Phi_a)$, where any Gaussian approximation would predict a divergent susceptibility [3]. By using Eq 4.2 to define an effective superfluid density from the zero field response, $\frac{1}{\lambda^2_{\text{eff}}} = \frac{\mu_0 L}{wd}\frac{\partial I}{\partial \Phi_a}\big|_{\Phi_a=0}$, one can see (Fig 4.3B) that fluctuations make the susceptibility deviate from the mean field response below $T_c(0)$, gradually smoothing the transition. Our parameterization of the theory shows that γ is the only sample dependent parameter at $T = Tc(0)$. The temperature range where non-Gaussian fluctuations are important is typically parameterized through the Ginzburg parameter as $|T - T_c(\Phi_a)|/T_c < Gi$, or equivalently $|T - T_c(\Phi_a)|/E_c < \frac{2}{\pi^2}\sqrt{\gamma} = \frac{T_c}{E_c}Gi$ [25, 75]. Inside this range, γ determines the magnitude of the response. Far above this range, Gaussian fluctuations dominate and the susceptibility is a function of $|T - T_c|/E_c \propto L^2/\xi^2$ alone.

The theory's dependence on γ allows us to state the criterion for the visibility of the Little-Parks effect in the context of fluctuations. The region that is shaded in green in Fig 4.3C is above $T_c(\Phi_a = \Phi_0/2)$ because $\xi(T) > L/\pi$. The susceptibility would be zero in this regime if fluctuation effects were not considered. When $\gamma \ll 1$, the distinct Little-Parks shape is visible, in that the susceptibility is smaller at $\Phi_a = \Phi_0/2$ than at $\Phi_a = 0$. However, when $\gamma \gg 1$, the Little-Parks shape is entirely washed out by fluctuations (Fig 4.4). For sufficiently large γ, the susceptibilities at $\Phi = 0$ and $\Phi_0/2$ are equal and opposite even below $T_c(\Phi = \frac{1}{2})$ so the response appears sinusoidal. This dependence on γ, rather than L and ξ alone, is the reason why the Little-Parks lineshape does not occur in the ring shown in Fig 4.2A, 4.4C.

Several factors contribute to the large fluctuation response near $\Phi_a = \Phi_0/2$ above $T_c(\Phi_a)$. First, the Gaussian fluctuations between $T_c(\Phi_a = 0)$ and $T_c(\Phi_a)$ have an large magnitude which is due to the interplay between adjacent phase winding states. In

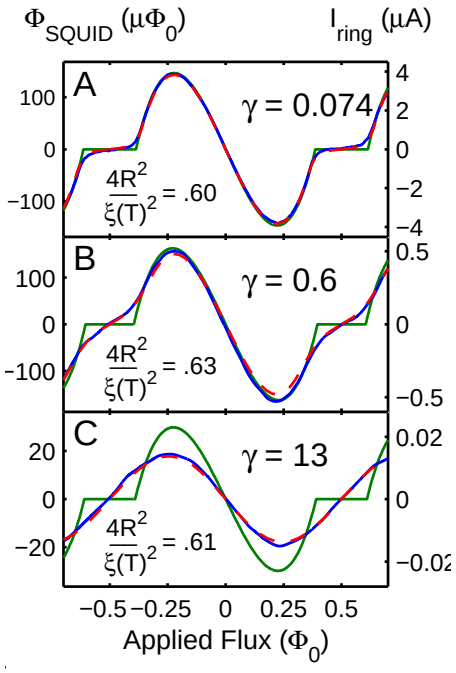

Figure 4.4: Mean field theory (green), fluctuation theory (red) and data (blue) for three rings with different γ parameters. The mean field response is derived from the fluctuation theory parameters for each ring at the given temperature. A $T = 1.20$K. In small γ rings, the Little-Parks line shape is clearly observable. B $T = 1.25$K. When $\gamma \approx 1$, the reduction of the response due to the Little-Parks effect is significantly suppressed. C T = 1.25K. In large γ rings, the Little-Parks effect is completely washed out by fluctuations, which affect the response at all flux values.

small γ rings, the non-Gaussian fluctuation region in Fig 4.3C is quite small. Thus, there is a large region where the magnitude of the persistent current near $\Phi = \Phi_0/2$ is strictly a function of $k_B(T - T_c)/E_c$. In large γ rings, non-Gaussian fluctuations play an increased role in the phase diagram, multiple phase winding modes need to be considered [25] indicating the importance of phase fluctuations. In all rings, non-homogeneous wavefunction solutions similar to saddle points solutions may have a non-negligible contribution to the final currents due to their vanishing energy cost near $T_c(\Phi_a)$. Small variations in width 4.2 make non-homogeneous wavefunctions more important [9], and would be important to include in an extended theory.

Fluctuation effects play a important role in 1D superconducting structures. Our analysis explicitly demonstrates how Gaussian and non-Gaussian fluctuations affect the persistent current in rings with various diameters and cross-sections, as a function of applied magnetic flux. A single parameter, γ, characterizes the fluctuations for a given ratio of the temperature-dependent coherence length to the circumference. When γ is large, the signature of a Little-Parks flux dependent $T_c(\Phi_a)$ is entirely washed out by fluctuations. When γ is small, the susceptibility in the non-Gaussian region near $T_c(\Phi_a)$ is enhanced and Gaussian fluctuations are clearly visible between $T_c(\Phi_a)$ and $T_c(0)$ for $\Phi_a \approx \Phi_0/2$. This new framework for understanding Little-Parks fluctuations is supported by our data on fluctuation-induced currents in rings.

4.2 Supplementary Online Material for ""Fluctuation Superconductivity in Mesoscopic Aluminum Rings"

Abstract

In the materials and methods section, this document elaborates on the experimental Superconducting Quantum Interference Device (SQUID) technique introduced in section 4.1 by describing the measurement apparatus and experimental conditions. After describing the sample fabrication, special attention is given to variations in the

cross section of the ring, which can have the effect of a decreased mean free path. The supporting online text section expands theoretical discussion, pedagogically introducing the Ginzburg Landau (G-L) free energy and the effects one might expect in finite line-width rings. The discussion includes a fluxoid fluctuation model that is appropriate far below $T_c(\Phi)$ and a Gaussian fluctuation model that is appropriate far above $T_c(\Phi)$. The section concludes by describing aspects of the full fluctuation solution discussed in the main text such as the difficulties involved with its full numeric solution far from $T_c(0)$. Two tables introduce the measured and fitted parameters for each ring, and the agreement with a quantitative SQUID–Ring mutual inductance model. Additional data of each ring's response as a function of temperature at three flux values is available online.

4.2.1 Materials and Methods

Our measurement apparatus [11] consists of a SQUID susceptometer attached to a scanning assembly that includes a large area scanner and an atto-cube coarse positioner system. Sub-millikelvin temperature control is made possible by feeding back on the temperature of the sample/scanner assembly, which is connected to the base plate of a dilution refrigerator through a single copper braid. The primary evidence for the fact that thermal drifts within the system do not significantly affect this control mechanism is that ring-current features, which vary strongly with temperature, change by less than 1 mK after a period of up to several days regardless of the temperature state before the measurement was made.

The DC SQUID susceptometer is voltage-biased and amplified by a series-array SQUID preamplifier [36]. Feedback through integrated modulation coils allows for optimal noise performance and a linearized response at all applied fields. Under operating conditions, the susceptometer has a $1/f$ noise of $\sim 2\ \mu\Phi_0/\sqrt{\text{Hz}}$ around the measurement frequency of 10 Hz. This low frequency noise is similar to the reported noise of other devices [86]. Additional measurements indicate that this low frequency noise is not due to the room temperature electronics or any of the amplification stages. Tests using bias reversal schemes [21] indicate that this noise is flux noise, rather

Ring	Radius (μ m)	width (nm)	ℓ_e (nm)	M_{S-R} (μ Φ_0/nA)	T_c (K)	γ
1	0.35	65	14.5	0.041	1.268	0.22
2	0.35	110	17	0.042	1.249	0.093
3	0.35	110	17	0.038	1.249	0.093
4a	0.35	110	19	0.037	1.247	0.074
4b	0.35	110	19	0.030	1.247	0.074
5	0.35	135	26	0.035	1.24	0.032
6	0.35	180	31	0.032	1.237	.014
7	0.5	65	15	0.091	1.264	0.597
8	0.5	110	19	0.071	1.253	0.218
9	0.5	110	19.5	0.081	1.248	0.206
10	0.5	110	19.5	0.084	1.244	0.205
11	0.5	135	24.6	0.075	1.241	0.105
12	0.5	175	24	0.089	1.244	0.085
13	1	110	19	0.31	1.251	1.742
14	1	110	20	0.38	1.251	1.572
15	2	110	19.4	1.3	1.252	12.92

Table 4.1: Tabulation of the measured rings with geometrical parameters R and w, fit parameters ℓ_e, M_{S-R}, and T_c, and the resulting values of γ. Due to the numerical limitations described above, the theory was not tractable in the full Little-Parks temperature range for rings for rings 5 and 6 so the fit parameters are only approximate results, estimated from the response immediately around $T_c(\Phi_a = 0)$. The results for these two rings were not discussed in the main paper.

than critical current noise. The counter-wound device geometry cancels the response of the SQUID to the applied field to one part in 10^4, thus allowing direct digitization of the feedback signal without exceeding the dynamic range of the room-temperature electronics. An additional three orders of magnitude of background cancellation are achieved by comparing the signal immediately above the ring to the signal 12 μm above the sample. The difference between these two signals is the ring response plus a residual background that is primarily out of phase with the applied field, varies reproducibly with the distance from the bare sample substrate, is independent of temperature, and does not have the periodicity of the ring signal. For each ring, this single temperature-independent ellipse (that is, an in and out of phase linear

Radius (μ m)	M_{S-R} (H)	M_{S-R} (μ Φ_0/nA)
0.35 μm	7.65e-14	0.0382
0.5 μm	1.60e-13	0.0800
1 μm	7.30e-13	0.365
2 μm	2.65e-12	1.325

Table 4.2: Mutual inductances calculated with a Fast Henry model of our pickup loop 0.75 μm away from rings with various radii.

response) was subtracted from the data set at each temperature to reveal $I - \Phi_a$ plots such as those shown in Fig 2 of the main text.

The rings were fabricated using standard electron beam lithography techniques on a SiO_x substrate, which is separate from that of the SQUID. The reported rings have a range of radii (R = 0.35 - 2 μm) as shown in table 4.1. Measurements on smaller rings are not reported here, because we could not apply a full flux quantum through the ring's center with our local field coils. The line widths, which vary between 65 and 180 nm were measured with a scanning electron microscope. The thickness, $d = 60$ nm, was measured with an atomic force microscope. The aluminum was ebeam-evaporated at a relatively high rate (3.5 nm/second) in a low pressure environment ($< 10^{-7}$ Torr) to obtain a long mean free path, ℓ_e. The fit parameters to our fluctuation model indicate that $\ell_e = 15 - 25$ nm varies systematically with the annulus line width, w, which we attribute to oxygen released by the polymethyl methacrylate (PMMA) resist during the metal evaporation process. The predominant variation in the cross-section of each ring comes from a $\sim 20\%$ roughness at the ring-edge associated with the liftoff process. It has been shown [9] that gradual variations of order 30% can change $T_c(\Phi_a = \Phi_a/2)/T_c(\Phi_a = 0)$ by approximately 5%. We expect that this change would be absorbed into the fitting parameters that are displayed in table 4.1. While we do not observe effects that are qualitatively different from the susceptibilities predicted by our strictly homogenous line width models, such effects may exist where our full fluctuation solution is not numerically tractable.

4.2.2 Supplemental Online Text

The thermal fluctuations described in this study are theoretically grounded in the Ginzburg-Landau free energy, F, for a 1D superconductor with periodic boundary conditions. The rings are 1D in the sense that the wave function, ψ, is assumed to only vary along x, the coordinate which is parallel to the circumference of the ring. This assumption is valid when the annulus width, w, and thickness, d, are much smaller than the temperature-dependent G-L coherence length, $\xi(T)$, which determines the length scale for the energetic costs associated with changes in ψ. The solution that minimizes the free energy of a homogeneous cross-section ring has the form $\psi(x) = |\psi| \exp(i2\pi nx/L)$, where n is the phase-winding number guaranteed by the single-valuedness of the wave function. The free energy [90, 91] for a solution of this form is

$$\begin{aligned} F/V &= \alpha|\psi|^2 + \frac{1}{2}\beta|\psi|^4 \\ &\quad + \frac{\hbar}{2m^*V}\int_V dV \left(\frac{n}{r} + \frac{e^*}{2\hbar}rB\right)^2 |\psi|^2. \end{aligned} \tag{4.4}$$

where V is the volume of the ring and r is the radial coordinate. By minimizing this free energy, one can obtain an expression for current, I, in a ring with finite linewidth, as shown in [90]. This allows for a clean distinction between critical field effects, associated with flux threading the annulus of the ring, and the pair-breaking effects associated with the flux-induced Aharanov-Bohm phase around the ring's circumference. To understand the Little-Parks effect [56], it is enough to consider the $w \ll R$ limit (e.g. eq. 1 of the main text), where I_n is given by

$$\begin{aligned} I_n &= -\frac{1}{\lambda^2}\frac{wd\Phi_0}{L\mu_0}(\Phi_a/\Phi_0 - n)P, \\ P &= \max\left(1 - \left(\frac{2\pi\xi(T)}{L}\right)^2 (\Phi_a/\Phi_0 - n)^2, 0\right), \end{aligned} \tag{4.5}$$

This limit is appropriate because $w, d \ll \lambda(T)$ which allows self screening effects to be neglected. Critical field effects are negligible in our rings because the flux

captured in the annulus of the ring is much smaller than Φ_0 for flux values discussed here ($\Phi_a \lessapprox \Phi_0/2$). This last condition guarantees the strictly periodic response in $(\Phi_a/\Phi_0 - n)$, which is shown in the right inset to Fig. 2D. Above $T_c(\Phi_a)$ the agreement with the 1D fluctuation theory (Fig. 2A-C) for a relatively wide (110 nm), small radius (350 nm) ring demonstrates that the finite line-width effects are not essential to our physical result.

At some temperature below $T_c(\Phi_a)$, our rings have a hysteretic response (similar to fig 1 of [16]) that is associated with the multiple solutions to eq. 4.5 that are possible when $\xi(T) < L/\pi$. This metastability can be understood quantitatively within the framework of thermally activated phase slips [53, 63] in the context of superconducting rings [90, 16]. We believe that the data presented here is in thermal equilibrium because it is sufficiently above the temperature where hysteresis occurs. Our treatment is further justified by the fact that we focus on the temperatures where $\xi(T) > L/\pi$, where such metastable states are not theoretically possible.

Fluctuations are important when contributions from multiple wave function configurations need to be considered to describe the ring's response. A simple model [16] estimates the equilibrium response with the Boltzmann distribution of fluxoid states. This gives the expression

$$\langle I(\Phi_a)\rangle_F = \frac{\sum_n I_n \exp(-E_n(\Phi_a)/k_B T)}{\sum_n \exp(-E_n(\Phi_a)/k_B T)} \tag{4.6}$$

where $E_n(\Phi_a) = -\int_n^{\Phi_a} I_n d\Phi_a$ is the energy associated with each local minimum of the G-L free energy functional. While this model is not strictly applicable to our data, because it cannot predict a response above $T_c(\Phi_a)$, it helps to illustrate some of the important physics at half integer flux values. When $\Phi_a = (n + \frac{1}{2})\Phi_0$, I_n and I_{n+1} contribute equally to the equilibrium current with contributions of equal and opposite magnitude. The response thus goes through zero at the half-integer flux values even when a mean field solution exists at that flux bias point. In this case, the susceptibility can have a large magnitude due to the exponentially changing weight of the fully condensed mean field states. When the superconducting response is small (e.g. for our large γ rings when $\xi(T) \lessapprox 2R$), $E_n \approx k_B T$ for several n states and a

large number of fluxoid states need to be considered, giving the significantly rounded response well before $T_c(\Phi_a = \Phi_0/2)$. This phase-only model thus correctly describes aspects of the ring behavior below $T_c(\Phi_a)$.

Both Gaussian and non-Gaussian fluctuations can allow for contributions from wave function solutions that have local variations in their phase and amplitude. These contributions are not included in the model described above, because all variation around the ring is described by the single homogeneous phase winding determined by n. The Gaussian response above $T_c(\Phi_a)$ can be derived by giving k_BT of energy to each fluxoid mode of a solution of the form $\psi = \sum_n c_n \exp(in2\pi x/L)$ [25]. This process gives the expression

$$\langle I \rangle_G = 2\frac{k_B T_c}{\Phi_0} \sum_{n=0}^{\infty} \frac{(\Phi_a/\Phi_0 - n)}{\Theta/4 + (\Phi_a/\Phi_0 - n)^2} \tag{4.7}$$

where $\Theta \equiv \frac{8}{\pi}\frac{(T-T_c)}{E_c/k_B}$ is the temperature scale associated with the energetic cost of a gradient in the wave function because $\Theta \equiv \pm 4R^2/\xi(T)^2$. Gaussian fluctuations can also be important below $T_c(\Phi_a)$ but in this case the solution must also take into account the wave function response associated with the mean field response. The model described by equation 4.7 predicts a γ-independent current that agrees well with each ring at some γ dependent temperature above $T_c(\Phi_a)$.

To qualitatively understand the difference between Gaussian and non-Gaussian fluctuations, one may consider a simplified free energy $F(\psi) = \alpha(\Phi_a)|\psi|^2 + \frac{1}{2}\beta|\psi|^4$, in which spatial variations of the order parameter are assumed to be frozen out, so that its amplitude is the only variable. In this case one can define $\alpha(\Phi_a) \propto T - T_c(\Phi_a)$ to incorporate the flux dependence of T_c. A non-zero solution minimizes this expression below $T_c(\Phi_a)$, where $\alpha(\Phi_a)$ is negative (β is defined to be positive). The term "fluctuation response" refers to the response that cannot be described by this free energy minimum alone, but requires the consideration of thermally activated fluctuations around it. If these fluctuations can be calculated accurately by a quadratic expansion of the free energy around its minimum, they are called "Gaussian". This occurs far above $T_c(\Phi_a)$, where ψ is small so that the $\alpha(\Phi_a)|\psi|^2$ term dominates $\beta|\psi|^4$. Fluctuations are also Gaussian far below $T_c(\Phi_a)$, where the quadratic expansion can

be taken about the minimum of the so called "mexican hat" potential described by a negative $\alpha(\Phi_a)$ and positive β. As T approaches $T_c(\Phi_a)$, the vanishing of $\alpha(\Phi_a)$ leads to a divergence of $\langle|\psi|^2\rangle$ as obtained from the quadratic expansion, which is also reflected in eq. 4.7. It is in this regime, near $T_c(\Phi_a)$, that fluctuations become "non-Gaussian" because the fluctuation amplitude is set by the $\beta|\psi|^4$ term rather than only the quadratic term. Thus, they can be thought of as interpolating between the mean field response below $T_c(\Phi_a)$ and the Gaussian fluctuations that dominate at high temperatures. The Ginzburg criterion determines the temperature range around $T_c(\Phi_a)$ where non-Gaussian effects need to be considered by identifying where $\beta\langle\psi^2\rangle^2$ is comparable to or larger than $\alpha\langle\psi^2\rangle$, (where $\langle\psi^2\rangle$ is the overestimate derived from Gaussian predictions). In our theory, β enters through $\gamma \propto \beta k_B T_c L^3/wd$, which shows that it parametrizes the non-Gaussian term and thus controls non-Gaussian effects.

To apply the complete theory [83], we evaluate the contribution of all possible wave functions, ψ, weighted according to their G-L energy, $E[\psi]$, to the mean current $I \equiv -\partial F/\partial\Phi_a = k_B T \frac{\partial}{\partial\Phi_a} \ln Z_{sc}$. The superconducting partition function, Z_{sc}, is the path integral over all possible wave functions: $Z_{sc}(\Phi_a) = \int \mathcal{D}\psi\mathcal{D}\psi^* \exp(-E[\psi]/k_B T)$. Using the transfer operator technique [73], the evaluation of Z_{sc} for a 1D ring [83] can be transformed into a quantum mechanical eigenvalue problem. The flux-dependent terms can be separated, so that one obtains

$$Z_{sc} = \sum_{l=-\infty}^{\infty} \exp(-i2\pi l\Phi_a/\Phi_0) \sum_{n=0}^{\infty} \exp(-\gamma^{1/3}\mathscr{E}_{n,l}) \tag{4.8}$$

where $\mathscr{E}_{n,l}$ are the eigenvalues of the 2D single-particle Hamiltonian,

$$H = -\frac{1}{2}\nabla^2 + \frac{\pi^2}{2}\frac{\Theta}{\gamma^{2/3}}\vec{r}^2 + \frac{1}{4}\vec{r}^4. \tag{4.9}$$

We have rewritten these equations from the expression in reference [83] to emphasize $\gamma \approx 16\frac{k_B T_c}{M_{eff} E_c}$ and the dependence on the temperature scale Θ as defined above and in the main text.

The fact that the Little-Parks line shape is washed out by fluctuations in large γ rings can be understood qualitatively from the two components of γ. First, if

T_c/E_c is large, the entire Little-Parks temperature range is close to $T_c(\Phi_a = 0)$ and it becomes difficult to differentiate the fluctuation effects at $\Phi_a = 0$ and $\Phi_a/2$. The proportionality of γ to the cross section, entering through the number of channels, $M = k_F^2 wd/2\pi$, reflects that it is energetically more costly to thermally excite a certain order parameter amplitude over a larger volume.

While the theoretical analysis applies everywhere that a 1D G-L description is correct in principle, numeric solutions become exponentially difficult for small γ rings away from $T_c(\Phi_a = 0)$ Intuition for this difficulty can be derived from semiclassical approximations to the lowest eigenvalue energies of Eq. 4.9. Above T_c, the Hamiltonian is positive definite with a lowest eigenvalue $\mathscr{E}_{0,0} \approx 0 \Rightarrow Z_{sc} \approx 1$. Because the total partition function is the product of different states ($Z_{tot} = Z_{sc} Z_n ...$), Z_{sc} must be approximately constant above $T_c(\Phi_a)$. When the Little-Parks effect is significant, this means that $Z_{sc}(\Phi_a = \Phi_0/2)$ must also be approximately equal to one, which leads to a difficulty in our formalism because the same eigenvalues must also generate very large numbers at $\Phi_a = 0$. For instance, when $\xi = R$ below $T(\Phi_a = 0)$ the lowest eigenvalue $\mathscr{E}_{0,0}$ can be estimated by the depth of the potential well in Eq 4.9 as $\mathscr{E}_{0,0} \approx \frac{4\pi^4}{\gamma^{4/3}}$. The value of the first term of the sum is thus $\approx \exp \frac{4*\pi^4}{\gamma}$, which can be 90 orders of magnitude larger than the value of Z_{sc} at $\Phi_a = \Phi_0/2$ for some of our data points. We solved this problem through direct computation, but the exponentially increasing difficulty means that further analysis of small γ rings will require further insight or a new approach. Daumens et al. [25] have shown that the full non-Gaussian response of two modes can be treated analytically, which should provide a good approximation for small γ rings. Numeric techniques such as Monte Carlo or TDGL-based Langevin simulations [8] could also provide further insight, particularly in the case of non-homogeneous rings.

Chapter 5

Fluxoid Fluctuations in Mesoscopic Superconducting Rings

Nicholas C. Koshnick, Hendrik Bluhm, Julie A. Bert , Kathryn A. Moler
A paper draft intended for submission to *Physical Review Letters* or *Physical Review B*

Abstract

Rings are a model system for understanding phase coherence in one dimension. Uniform superconducting rings exhibit metastable states whose phase winds uniformly by an integer multiple of 2π around the ring. When the energy difference between these states is less than or equal to the temperature, several states contribute to the ring's response in thermal equilibrium. We present magnetic susceptibility data and a theoretical framework that demonstrate how these fluxoid fluctuations suppress the ring's diamagnetism below T_c. We also identify the parameters which determine the crossover between the reduction of the response due to phase fluctuations and the enhancement due to amplitude fluctuations.

5.1 Introduction

Fluctuations play an important role in the superconducting behavior of reduced dimensional samples: they can make electron pairing and long-range phase coherence occur at different temperatures in unconventional superconductors[26], lead to the Berezinskii-Kosterlitz-Thouless transition [51] in two dimensions (2D), cause the destruction of long range phase order in infinitely long one-dimensional (1D) wires [69], and determine the resistive properties of 1D wires of finite length [53, 63, 29, 55].

We study the properties of 1D wires in a model system, uniform isolated aluminum rings. We focus on the case where the circumference is much longer than the superconducting coherence length, $\xi(T)$. In this case one finds several metastable states, which only differ by a phase winding, or fluxoid, number. Comparing the response predicted from these phase-only solutions to experimental data and more comprehensive theories allows for a clear distinction between phase and amplitude fluctuations.

Transport measurements probing 1D fluctuations rely on the voltage generated by changes in the phase winding value. We measure the current, I, as a function of applied flux, Φ_a, which gives us access to the free energy, F. By measuring at sufficiently high temperatures that phase slips occur rapidly compared to the measurement time, we are able to probe the thermal effects associated with the energy from phase winding about the entire ring, rather than the condensation energy of a ring-section of length ξ, ie. the phase slip energy.

In this paper we show that the thermal distribution of fluxoid states suppresses the ring's diamagnetism below the mean field value. These results complement previous studies of fluctuation effects in rings [90, 49], which mostly discuss the enhanced diamagnetism caused by amplitude fluctuations at and above the superconducting critical temperature, T_c. After presenting relevant ring data, we outline the theoretical definition of the effect and state a criterion for where a downturn in the susceptibility will occur. We then compare the fluxoid fluctuation effect to a theory that includes all thermally induced fluctuations in the G.L. framework [73, 83]. We describe the range of ring parameters where the simplified model is theoretically justified, and

identify where a fluxoid-like reduction in response is distinguishable from the response-enhancing effects near T_c.

5.2 Experimental Results

In previous experiments [16, 49, 17] we measured quasi-one-dimensional superconducting rings in a dilution refrigerator [11] with a scanning SQUID susceptometer [37] that was explicitly designed for this purpose. The data discussed here was measured one ring at a time, as described in our previous work [16]. We focus on narrow, relatively dirty rings with width $w = 80$ nm and thickness $d = 40$ nm, which showed no sign of two-order-parameter-like behavior. Using the models discussed below and in [16], we extract a zero temperature penetration depth $\lambda(0) \approx 800$ nm and the coherence length $\xi(0) \approx 80$ nm, consistent with a mean free path $l_e \approx 4$ nm.

The current from each ring is measured by positioning the SQUID about 1μm above the ring and recording the flux induced by the ring's current. During the measurement, the applied flux threading the ring is varied by several flux quanta at a few Hertz. This measurement is repeated 13μm above the ring and the ring signal is computed as the difference between the two positions for each value of applied flux. We will only discuss the zero field susceptibility, extracted from the I vs. Φ_a data by linear fits near $\Phi_a = 0$.

If one only considers the lowest energy Ginzburg Landau solution, the susceptibility $(dI/d\Phi)$ near zero field is proportional to the superfluid density. This factor is expected to decrease linearly as temperature increases, reaching zero at T_c. When examining the response very near T_c, the susceptibility of rings with radius $R = 0.5\mu$m showed a slight upturn when compared to the linear decrease extrapolated from lower temperature data (Fig. 5.1a). This response is consistent with the fluctuation induced superconductivity reported [49] in rings with a larger mean free path, $l_e \approx 19 - 25$, which we will discuss later in the paper. This paper focusses on the data from five rings with $R = 2\mu$m where, in each instance, a downturn in the susceptibility vs. temperature curve occurs around a susceptibility of 120 nA/Φ_0 (Fig. 5.1b).

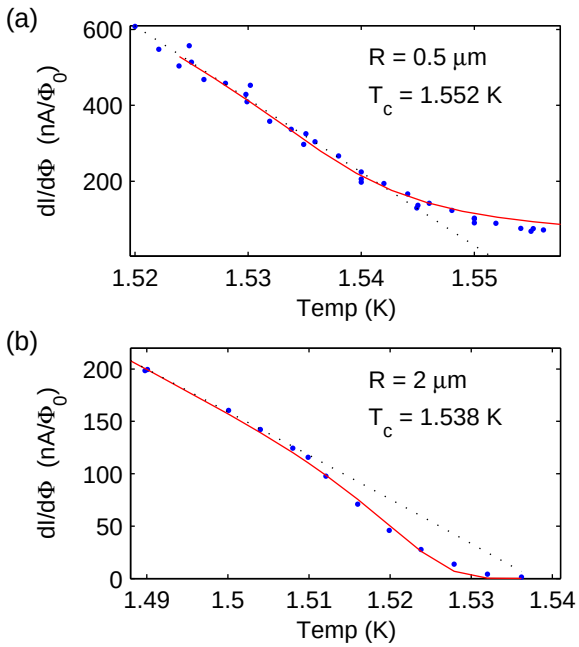

Figure 5.1: (Color Online) Zero field susceptibility (blue dots) as a function of temperature for two rings with $w = 80$ nm, $d = 40$ nm. The black dotted line represents the expected susceptibility given by I_0' (Eq. 5.3). a) Data from a ring with R $= 0.5$ μm. The red line is a fit to Eqs. 5.7, 5.8, which can describe the fluctuation induced superconductivity above T_c. b) Data from a ring with R $= 2$ μm. The red line is the fluxoid fluctuation model (Eq. 5.5), which predicts a downturn when $dI/d\phi \lessapprox 12k_BT/\Phi_0 = 120$ nA$/\Phi_0$ for $T = 1.51K$.

5.3 The Fluxoid Fluctuation Transition

Solutions that minimize the Ginzburg Landau free energy functional for a one dimensional ring with n phase windings have free energies

$$F_{GL} = -V\frac{B_c^2}{\mu_0}\Big(1 - \frac{\xi(T)^2}{R^2}(\phi - n)^2\Big)^2. \tag{5.1}$$

where B_c is the critical field, V is the ring volume, and μ_0, the permeability of free space, all enter into the ring's total condensation energy. The dependence on ξ/R accounts for the energy cost of n phase windings around the ring. The Aharonov-Bohm phase gradient, $\phi = \Phi_a/\Phi_0$, associated with the applied flux in units of the superconducting flux quantum, $\Phi_0 = h/2e$, can be transformed into a shift in the boundary conditions for a wave function in a ring [19], and therefore contributes to the energy in the same way as n.

Expanding this energy to the lowest order in ξ/R we get

$$E_n(\phi) = \frac{I_0'\Phi_0}{2}(\phi - n)^2 - V\frac{B_c^2}{\mu_0}. \tag{5.2}$$

where

$$I_0' \equiv V\frac{B_c^2}{\mu_0}\frac{4}{\Phi_0}\frac{\xi^2}{R^2} = -\frac{wd\Phi_0}{L\mu_0}\frac{1}{\lambda^2}. \tag{5.3}$$

is the magnitude of the Meissner response $I = -\frac{1}{\Phi_0}\frac{\partial F}{\partial \phi} = I_0'(\phi - n)$ given in terms of physical constants, geometric parameters, and the inverse squared penetration depth, $1/\lambda^2$, which is proportional to the super-fluid density.

Multiple phase winding states effect the ring response significantly when the energy difference between the lowest energy levels, $\Delta(E_n) = E_{n=\pm1} - E_{n=0}$, is comparable to k_BT. This criteria is directly related to the Meissner currents that screen the magnetic field.

If phase slips occur at a high enough rate, and the metastable fluxoid states are in thermal equilibrium (see section 5.5), the resulting response can be modeled [16]

as a Boltzmann distribution of fluxoid states

$$I(\phi)_F = \frac{\sum_n I_n \exp(-E_n(\phi)/k_B T)}{\sum_n \exp(-E_n(\phi)/k_B T)}. \tag{5.4}$$

The derivative about $\phi = 0$ is

$$\left.\frac{dI}{d\phi}\right|_{\phi=0} = I_0' \left(1 - \frac{\sum_n 2\beta n^2 \exp(-\beta n^2)}{\sum_n \exp(-\beta n^2)}\right) \tag{5.5}$$

where $\beta \equiv I_0' \Phi_0 / 2k_B T$. When β is large, terms with $n \neq 0$ are small and the susceptibility is simply I_0'. When $\beta < 6$, the $n = \pm 1$ terms begin to play a significant role, and the Meissner response is reduced by more than 5%. This allows us to define

$$\frac{dI}{d\phi} \approx I_0' < \frac{12 k_B T}{\Phi_0}. \tag{5.6}$$

as a criterion for the visible onset of fluxoid fluctuations. A distinct down turn is visible in Fig. 5.1 at this value ($dI/d\phi \approx 0.1 \mu A/\phi_0$), around $T = 1.51$K. This downturn occurs close to T_c where the superfluid density decreases linearly with increasing temperature. However, we note that fluxoid fluctuations are energetically allowed for sufficiently long, thin rings, even for much larger superfluid densities at $T \ll T_c$.

5.4 Relating Fluxoid and Non-Fluxoid Fluctuations

Thus far, we have considered a simplified description that explains the existence of the downturn in susceptibility shown in figure 5.1b. In some of the data, near $T = T_c$, the $L \gg \xi$ assumption is not strictly valid. In this case, the energy between successive metastable states is no longer directly related to the Meissner current as described above. Equation 5.4 is also not well behaved because incorporating the quartic term of Eq. 5.1 requires the consideration of infinitely many states. Furthermore, our treatment thus far has ignored phase oscillations that are not uniform around the ring and amplitude oscillations of every kind. To address these issues, we compare our simple fluxoid model to the model of von Oppen and Riedel, VOR [83], which allows

for numeric solutions that include all thermal fluctuations in a homogeneous rings. We also discuss the approximate harmonic oscillator, HO, solution to this theory, which provides a direct mathematical connection to the fluxoid model discussed above.

The VOR model uses a formalism [73] where the Ginzburg-Landau path integral partition function of the ring can be mapped onto another partition function

$$Z = \sum_{l=-\infty}^{\infty} \exp(-i2\pi l\phi) \sum_{n=0}^{\infty} \exp(-\gamma^{1/3}\mathscr{E}_{n,l}) \tag{5.7}$$

where $\mathscr{E}_{n,l}$ are the eigenvalues of the fictitious 2D single-particle Hamiltonian,

$$H = -\frac{1}{2}\nabla^2 + \frac{\pi^2}{2}\frac{\Theta(T)}{\gamma^{2/3}}\vec{r}^2 + \frac{1}{4}\vec{r}^4. \tag{5.8}$$

In this expression, $\Theta(T) \equiv 8k_B(T - T_c)/\pi E_c$ where $E_c = \pi^2\hbar v_F \ell_e/3L^2$ is the correlation or Thouless energy, v_F is the Fermi velocity, and ξ_0 is the Pippard zero temperature coherence length. The parameter $\gamma \equiv (42\zeta(3)/\pi)k_B T_c/M_{\text{eff}}E_c$, where $\zeta(3) \approx 1.2$ and $M_{\text{eff}} = (\ell_e/L)\ (k_F^2 wd/4\pi)$, has been discussed in the context of the Little-Parks effect [49]. The temperature dependence is set by the coherence length through the relation $-\Theta(T) = \frac{L^2}{\xi(T)^2}$ for $T < T_c$.

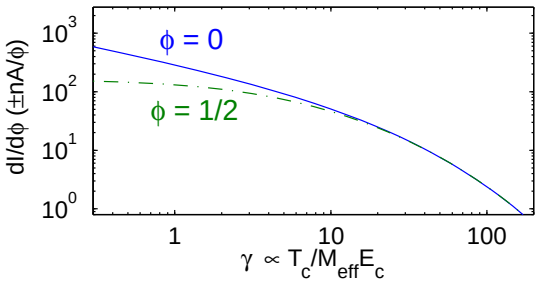

Figure 5.2: The susceptibility at $T = T_c$ as predicted by the VOR theory. When $dI/d\Phi > 12k_B T_c/\Phi_0$ (Eq. 5.6), fluxoid fluctuations are overcome by the enhanced response at and above T_c. The Little-Parks effect is observable as the difference in susceptibilities at $\phi = 0$ and $\phi = 1/2$, for small γ.

Numeric solutions to equations 5.7, 5.8 can predict the fluctuation induced response at and above T_c [49]. We solved these equations to generate the red curve in

Fig. 5.1a. In Fig. 5.2, we show the susceptibility as a function of γ at $T = T_c$. At this temperature, γ is the only sample dependent parameter . When the susceptibility at $T = T_c$ is greater than that given by Eq. 5.6, (eg. $\approx$120 nA for $T_c = 1.5$ K) the fluctuation induced superconductivity at and above T_c masks the fluxoid effects that can reduce the response below T_c. This indicates that a visible downturn in the susceptibility cannot occur if $\gamma \lesssim 10$ when $T_c \approx 1.5K$.

The presence of a visible upturn or downturn is demonstrated in the plots of theoretical susceptibilities as a function of temperature shown in Fig. 5.3. In this figure we use the relation $I_0' = k_B T_c 4\pi^4 \Theta(T)/\gamma\Phi_0$ to compare the full theoretical response to the simplified models. When $\gamma = 3$, the susceptibility at $T = T_c$ is 140 nA, so a downturn is not observable. When $\gamma = 3100$, the fluctuation induced superconductivity near $T \approx T_c$ is negligible, and the fluxoid induced downturn becomes visible below T_c.

At some temperature sufficiently below T_c, the mexican hat potential given by Eq. 5.8 is mostly parabolic near its minimum. In this case, non-Gaussian effects should not play a significant role, and the eigenvalue solutions can be estimated by a harmonic oscillator (HO) approximation. Solutions have the form $\vec{r} = |r| \exp(il\phi)$, so Eq. 5.8 can be written as a 1D problem, $H = -\frac{1}{2}\frac{d^2}{dr^2} + V(r)$ where

$$V(r) = \frac{l^2}{2r^2} + \frac{\pi^2\Theta(T)}{2\gamma^{2/3}} r^2 + \frac{1}{4} r^4. \tag{5.9}$$

Expanding $V(r)$ about its minimum at $R_{\rm m}(l)$ the eigenvalues have the form

$$\mathscr{E}_{n,l} = \frac{l^2}{2R_{\rm m}(l)^2} + \frac{R_{\rm m}(l)^4}{4} + \omega(n + 1/2) \tag{5.10}$$

where $\omega = \sqrt{\pi^2\Theta(T)/2\gamma^{2/3} + 3R_{\rm m}(l)^2 + 3l^2/R_{\rm m}(l)^4}$

Only terms that change with l, the angular momentum coordinate in the fictitious Hamiltonian, contribute to the flux dependence of the partition function, thus only these terms can contribute to the thermodynamic ring-current. If we only include the

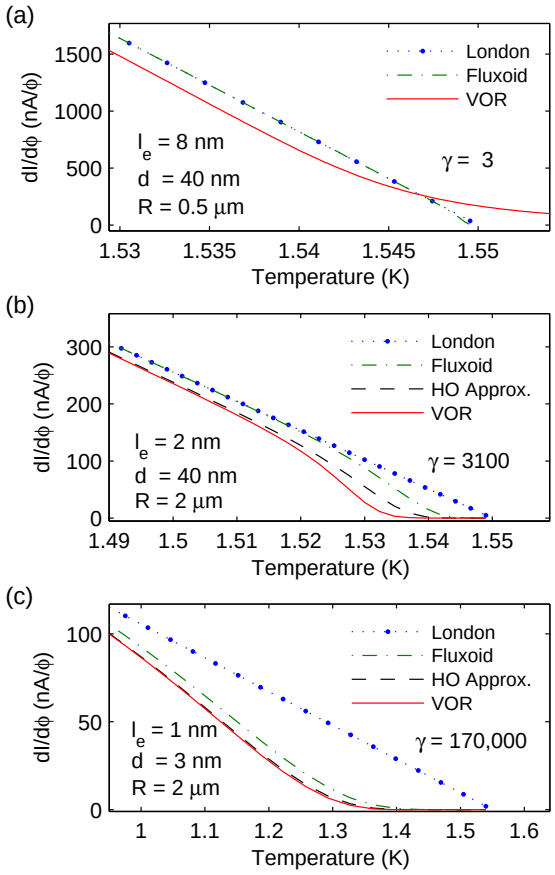

Figure 5.3: (Color Online) Theoretical susceptibilities of the London response (Eq. 5.3), the fluxoid model(Eq. 5.4), the VOR model (Eq. 5.7, 5.8), and its approximate HO solution (Eq. 5.12). $T_c = 1.55$ and $w = 40$ nm for all rings. a) $\gamma = 3$. The VOR model predicts a response at and above T_c. Well below T_c, the response only matches the London predictions if the value of T_c used for the London model is renormalized to a slightly lower value. b) $\gamma = 3100$. A downturn occurs at $dI/d\Phi \approx 12k_BT/\Phi_0$. The HO approximation mirrors the Fluxoid model with the renormalized T_c of the VOR model. c) $\gamma = 170,000$. Fluxoid fluctuations effect the ring over a large temperature range ($\approx 30\%$ of T_c). The HO and fluxoid models become increasing accurate predictors of the full fluctuation theory.

$l^2/2R_{\rm m}(0)^2$ term, the current is

$$I = k_B T \frac{1}{Z} \frac{\partial}{\partial \Phi_a} Z_{sc} = \frac{\sum_n 2\pi l \sin(2\pi l\phi) \exp(l^2\gamma/\pi^2\Theta(T))}{\sum_n \cos(2\pi l\phi) \exp(l^2\gamma/\pi^2\Theta(T))} \tag{5.11}$$

which is exactly equivalent to equation 5.4. Including the second two terms of Eq. 5.10, which account for the angular momentum dependence of ω and $R_{\rm m}(l)$, we get

$$\begin{aligned} Z = & \sum_{l=-\infty}^{\infty} \exp(-i2\pi l\phi) \exp(-\gamma^{1/3} V(R_{\rm m}(l))) \\ & \times \frac{\exp(-\gamma^{1/3}\omega/2)}{1-\exp(-\gamma^{1/3}\omega)} \end{aligned} \tag{5.12}$$

Figure 5.3b,c show the results from the simple fluxoid model (Eqs. 5.4, 5.11, dashed green lines), and this HO approximation (dashed black lines) alongside the VOR model (Eq. 5.7, 5.8, solid red) and the London response (Eq.5.3, dotted blue). The HO solution qualitatively reproduces the downturn in susceptibility of the fluxoid model. One striking difference is that both the VOR model and its HO approximation have an offset in the linear regime far below T_c when compared to the London or fluxoid model. This can be described as an apparent renormalization in T_c due to the consideration of all possible fluctuation modes.

When γ is in the range of a few thousand (Fig. 5.3c), the VOR model predicts more of a downturn in the susceptibility than is predicted by the fluxoid or HO models, which is presumably due to contributions from non-homogeneous phase winding solutions, amplitude fluctuations, or both. When γ is substantially larger, the fluxoid fluctuation effect occurs far below T_c. In this case, the harmonic oscillator and T_c shifted fluxoid models are in good agreement with the more complete theory, indicating that that fluxoid fluctuation approximation is valid.

Superconducting phase slips in one dimensional wires have been the subject of theoretical and experimental interest for several decades. While phase slips determine the onset of resistance, the fluxoid process we describe here causes the loss of another hallmark of superconductivity, the ability to screen magnetic field. Our rings are a model 1D system that is easy to manipulate with modern fabrication techniques.

One could imagine extending this ring system to a weakly connected grid, linking the underlying physics to results in the field of percolation superconductivity. Achievable experimental conditions (see section 5.5) allow fluxoid fluctuations to occur at temperatures down to 50 mK. Fluctuation effects at these low temperatures could shed further light on quantum activated phase fluctuations [29, 10] and resulting quantum mechanical behavior of a 1D ring [62]. Finally, we note the experimental conditions could occur in short mean free path classical superconductors where localization effects become important when the ring resistance is more than e^2/h.

This work was supported by NSF Grants DMR-0507931, DMR-0803974, PHY-0425897 and by the Packard Foundation. Work was performed in part at the Stanford Nanofabrication Facility, which is supported by NSF Grant No. ECS-9731293, its lab members, and industrial afliates.

Addendum

I have prepaired additional rings with $w = 80-300$ nm, $d = 4$ nm, and $R = .35-2\mu$m, fabricated under conditions where $l_e \lesssim 4$nm. These parameters should allow for a much larger temperature range where fluxoid fluctuations occur, further illucidating the effect and allowing for the possibility of new physics. Julie A. Bert currently plans to measure these samples in the spring of 2009.

Supplemental Material

Abstract

In the main paper, we use our fluxoid model to describe a condition where a thermodynamic distribution of phase states can dramatically affect the ring's ability to screen magnetic field. The assumption of thermodynamic equilibrium is justified when phase slips occur at a rate that is high compared to experimental time scales, typically on the order of a few hundred hertz. In this supplement, we address the issue of when the ring is in equilibrium by considering the phase slip theory of Langer

and Ambegaokar [53] as formulated for rings [91, 90].

5.5 Conditions for Equilibrium

The phase slip theory of Langer and Ambegaokar [53] as formulated for rings [91, 90], predicts a phase slip rate, by calculating the lowest energy pathway between two fluxoid states as defined by the energy barrier for the saddle point in wave function configuration space. The saddle point energy is

$$F_{\text{saddle}} = F_c\Big(\frac{4\sqrt{2\delta}}{3}\frac{\xi}{L} - \frac{(2+\delta)^2}{18}\Big) \tag{5.13}$$

where $F_c \equiv wdLB_c^2/\mu_0$ is the ring's condensation energy and δ is a real number between 0 and 1 that satisfies the relation

$$2\pi n = \frac{2}{\sqrt{3}}\frac{L}{\xi}\frac{\sqrt{1-\delta}}{2} + 2\tan^{-1}\left(\sqrt{\frac{3\delta}{2(1-\delta)}}\right) + 2\pi\phi. \tag{5.14}$$

In the regime of interest $L \gg \xi$, δ must be close to one. By using the substitution $\delta = 1 - (\epsilon\frac{\xi}{L})^2$, expanding to lowest order in ξ/L, and solving for ϵ, we arrive at a simplified expression

$$\delta = 1 - \Big(\frac{\sqrt{3}\pi(2n - 2\phi - 1)}{\frac{L}{\xi} - 2\sqrt{2}}\Big)^2. \tag{5.15}$$

Going back to the energy expression, we can see that the lowest flux independent terms give $F_{\text{saddle}} = F_c(4\sqrt{2}\xi/3L - 1/2)$ (red dotted line in fig 5.4). As ξ/L becomes increasingly small, the flux dependent nature of both F_{saddle} and F_{GL} become less important to the energy difference $\Delta E_{\text{saddle}} = F_{\text{saddle}} - F_{GL}$ leaving only this flux-independent term. While F_c is proportional to the volume of the entire ring, $\Delta E_{\text{saddle}} \approx 3.8wd\xi B_c^2/\mu_0$ is proportional to the condensation energy of a section of the ring of length ξ. The criterion for phase slips is therefore physically distinct from the energy difference, $\Delta E_{\text{GL}} = E_{n=\pm1} - E_{n=0}$ as defined by Eq. 2 in the main paper, that determines the temperature where fluxoid fluctuations occur. However, in the limit where $L \gg \xi$, the fluxoid condition is already satisfied when phase slips begin

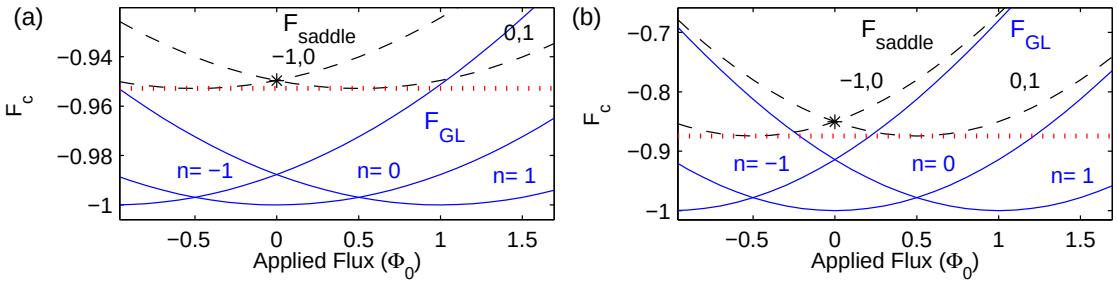

Figure 5.4: Fluxoid (solid) and saddle point (dashed) energies as a function of applied flux, in units of the condensation energy. The red dotted line is ≈ 3.8 times the condensation energy for a ring section of length ξ. **a** The respective energies when $L/\xi(T) = 80$. **b** The respective energies when $L/\xi(T) = 30$. The fluxoid fluctuation energy $\Delta E_{\rm GL} = E_{n=\pm1} - E_{n=0}$ scales differently than $\Delta E_{\rm saddle}$.

to occur, so in the longest wires both the fluxoid fluctuation and thermally induced phase slip effects have the same onset temperature.

Given the the saddle point energies, we can estimate the phase slip rate as:

$$R = \Omega \exp\left(-\frac{(F_{\rm saddle} - F_{GL})}{k_B T}\right) \tag{5.16}$$

The prefactor, $\Omega = (L/\xi)(F_{\rm saddle} - F_{GL}/k_B T)^{1/2}/\tau$, was derived based on arguments using the time dependent Ginzburg Landau model [63], where $\tau = \pi h/8k_B(T_c - T)$ is the relaxation time. In this formulation, the temperature dependence of the exponent is set by $\xi(T)$ and $\lambda(T)$. Aluminum with $l_e = 4nm$ has $\lambda(0) \approx 800nm$ and $\xi(0) \approx 85nm$. Using standard temperature dependences for these parameters, a ring of this material with $w = 80nm$ and $d = 40nm$ will have switching occur on experimental time scales down to 1.1 K when $T_c \approx 1.24$, while a ring with $d = 4nm$ will continue to have phase slips down to 0.45 K. Already, in this range, the foundations of time-dependent and time-independent Ginzburg Landau theory are invalid, and quantum fluctuations may play an important role [29, 10]. In future fabrication runs, we can extend the testable regime by further tweaking physical parameters. For instance, using the same model with $l_e = 1$ nm, $d = 2$ nm, and $w = 30$ nm, phase slips are predicted to occur at a high rate down to a temperature of 50 mK.

Chapter 6

Towards Superconducting Rings Where $E_c > k_B T_c$

In this chapter, I describe my efforts to fabricate and measure small, clean rings where the Thouless or correlation energy, E_c, is greater than or approximately equal to T_c. When considering this problem, an important limit is the amount of field that we can apply with the on-chip field coils. If we only consider rings where we can apply at least half a flux quantum of field, we are limited to rings that have a radius $R \gtrapprox 350$ nm. This sets a limit to the extent by which $E_c \propto v_F l_e / R^2$ can be increased simply by reducing R. After briefly discussing the exciting new physics in this regime, we will discuss our efforts to make cleaner rings (e.g. longer l_e) and clean rings with reduced T_c.

6.1 Theoretical Background

6.1.1 Clean Wide Rings: $T < E_c \approx k_B T_c$

The $E_c \gtrapprox T_c$ regime offers interesting Little-Parks physics because the ratio of E_c/T_c determines the amount that $T_c(\Phi)$ is reduced at finite values of applied flux.

$$\frac{T_c(0) - T_c(\Phi_a)}{T_c(0)} = 0.73\frac{\xi_0 l_e}{R^2}\left(\frac{\Phi_a}{\Phi_0} - n\right)^2 \quad (6.1)$$

$$= \frac{E_c}{4k_B T_c(0)}\left(\frac{\Phi_a}{\Phi_0} - n\right)^2 \quad (6.2)$$

When T_c is reduced much more than the approximately 10% of T_c reported in chapter 4, thermodynamic predictions in the Ginzburg-Landau (G-L) framework need to include temporal dynamics, which can be handled by including so called Matsubara frequencies [76]. If T_c is reduced all the way to $T = 0$, the second-order flux-tuned superconductor to normal metal transition creates a quantum critical point, where quantum fluctuations play an important role. One major goal for studying this regime is thus to reach this limit, which requires $\xi(0) \geq 2R$ in the standard G-L framework, as stated in chapter 4, or $\xi(0) \geq 1.6R$ when low temperature corrections to G-L are taken into account [75].

This "destructive" regime, where $T_c(\Phi_a = \Phi_0/2) = 0$ (Fig 6.1a), has been achieved in thin-walled cylinders [58]. The resistance at $\Phi_a = \Phi_0/2$ above $T_c(\Phi_a)$ is markedly reduced from the value at $\Phi_a = 0$. This effect has been attributed to fluctuation effects [71], although the existence of a co-axial degree of freedom along the cylinder allows for multiple interpretations of the underlying low temperature physics [82] and additional effects related to the vortex behavior perpendicular to the cylinder's axis [57]. The low temperature properties for a ring geometry are also a matter of current debate [76], but are more tractable theoretically because the reduced dimensionality simplifies the problem considerably. To avoid proximity effects, this regime must be measured either magnetically (without leads), or through tunneling measurements [33].

To study quantum effects in Little-Parks physics, one must have experimental

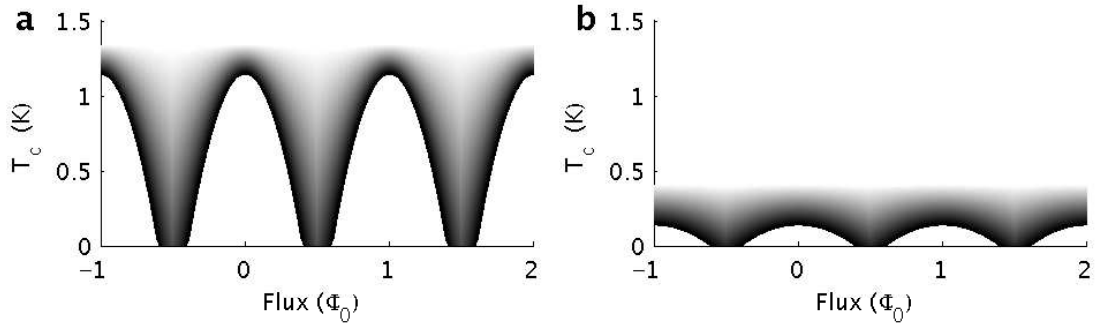

Figure 6.1: Diagram of T_c as a function of applied flux. The gray scale in the region indicates the relative importance of fluctuation effects above $T_c(\Phi_a)$, with darker regions having the potential for stronger fluctuation effects. a) Diagram of an Aluminum ring with $T_c(0) = 1.15$. b) A bilayer ring with $T_c(0) = .3$.

access to temperatures well below T_c. In some sense, this represents a trade-off, because materials with lower T_c's have a longer zero-temperature coherence length ($\xi(0) \propto 1/T_c$), and thus are more affected by the Little-Parks effect. We have primarily worked with aluminum (Al) because it is a well-known material with a relatively low T_c and a relatively long mean free path. In Al, $\xi_0 \approx 1.6$ is much larger than l_e, so $\xi(0) \propto \sqrt{l_e \xi_0}$. Section 6.2 will primarily talk about mean free path engineering of aluminum, in an attempt to reach the destructive regime.

In practice, the finite line-width, w, of superconducting rings can allow for additional reduction in $T_c(\Phi_a)$ in two ways. First, wider rings tend to have a larger l_e (see table 4.1), presumably due to less edge scattering and less oxidation effects from the outgassing of nearby PMMA during the metal deposition process. Second, wide rings have a lower critical field, H_{c2}. Critical field effects reduce T_c with increasing flux, which adds to the strictly 1D, periodic Little-Parks physics, shown in figure 6.1. This means that finite-width rings can have $T_c(\Phi = \Phi_0/2) = 0$ even when their coherence length and radius would predict that they would not reach the destructive regime if one only considers equation 6.2.

Zhang and Price [90, 91] derived an expression for the Ginzburg Landau free energy for rings with finite width. After minimizing this expression, they found the

current

$$I = \left(n - \left(1 + \frac{w^2}{4R^2}\right)\frac{\Phi_a}{\Phi_0}\right) \min\left[1 - \frac{\xi(0)^2}{R^2}\left(\left(n - \frac{\Phi_a}{\Phi_0}\right)^2 + \frac{w^2}{4R^2} * \left(\frac{n^2}{3} + \frac{\Phi_a}{\Phi_0}^2\right)\right), 0\right]. \tag{6.3}$$

This expression has terms that relate to both flux focusing and H_{c2} effects in a somewhat non-trivial way. Analyzing the conditions when $I = 0$, $\Phi_a \neq 0$, yields us a plot of $T_c(\Phi_a)$, from which we can derive a T_c versus Φ_a that has a decreasing phase with additional applied field. This effect is, of course, also important for superconducting cylinders, where the combination of Little-Parks and H_c physics has already been discussed [57]. The first $w/2R$ term in equation 6.3 increases the effective applied flux, allowing us to study smaller rings. The reduction in T_c due to the second term with $w/2R$ also allows rings to more easily reach $T_c(\Phi_a = \Phi_0/2) = 0$. Clearly, this effect is limited to the case where $w = R$, at which point the ring becomes a disc. The Little-Parks effect can most easily be distinguished from H_c effects when superconductivity re-emerges at an applied flux value $|\Phi_a| \approx \Phi_0/2$. For rings with radii R = 300 nm, this sets a limit on $\xi(T) > 500$ nm.

6.1.2 Bilayers: $T < T_c < E_c$

A second approach to reach the limit where $E_c > T_c$ is to maintain cleanliness while reducing T_c by making the ring from a bilayered superconducting/normal metal material. The physical intuition for the advantage of this approach does not rely on the fact that in pure metals, $\xi(0) \propto \xi_0 \propto 1/T_c$, which is probably not true for a proximity-effect reduced T_c. Rather, the curvature of the ring's $T_c(\Phi_a)$ phase diagram is set by some coherence length that should not reduce much in the bilayered material. By using the proximity effect to reduce T_c, there is a smaller temperature range to which the $T_c(\Phi_a)$ must to be lowered, in order to reach $T_c(\Phi_0/2) = 0$ (Eq.6.2, Fig. 6.1). Intuition for this logic stems from the Usadel equations, where a single-order parameter describes the superconducting response to Little-Parks-like phase gradients, T_c lowering magnetic impurities, or magnetic fields [4] Thus, in this simplified picture, the T_c reducing proximity effect and Little-Parks effect can be summed independently.

Although the Usadel theory formally only applies to homogeneous systems, similar logic might apply even with the introduction of normal metal layers.

A bilayer ring in the Cooper limit can can be modeled as a superconductor with a transverse-direction-independent order parameter and new physical parameters λ and ξ. This limit requires that the thickness of both layers is $d \lessapprox l_e$, and that the transmission coefficient between layers is sufficiently large. If a highly conductive noble metal is used for the normal metal layer, the ring can also have an increased l_e which in turn increases E_c.

The successful implementation of a SC/N ring could always allow for $E_c \gg k_B T_c$, if T_c is made to be arbitrarily small. The question then becomes what values are experimentally accessible. SQUID radiation on the sample limits effective ring temperatures to ~ 200 mK [15]; thus in our experimental setup, many bilayered systems may only be measured in a regime where $T > E_c/k_B > T_c$. Even so, this limit presents an interesting regime that is intimately related to the $h/2e$ persistent current physics in normal metal rings or the response of aluminum rings above H_{c2} [13]. In the Gaussian region above T_c, the magnitude of fluctuation is $\propto T_c/\Phi_0$. The magnitude of h/e persistent currents is $\propto E_c/\Phi_0$ [70]. Thus, by varying the superconductor or normal metal layer thicknesses, one can reach a limit where the two effects co-exist.

Clean, low-T_c, 2D materials have received attention in the superconductor-metal transition literature recently as a regime where even small amounts of disorder could lead to large spacial variations in the superconducting properties [78]. This prediction may manifest itself as enhanced mesoscopic fluctuations in measurements of a large number of nominally identical rings. Such a result would considerably extend the G-L description of the way inhomogeneities affect the Little-Parks effect [9].

The exact behavior of bilayered samples is difficult to relate to the physics discussed in chapter 4 because it is not clear whether the mesoscopic parameters that characterize γ have the same role in a bilayered system as they do in pure classical superconductors. That fact aside, it is interesting to note that a clean, low T_c superconductor, governed by standard G-L theory, would have different criteria for where the Little-Parks line-shape may be washed out by fluctuations. This is because the magnitude of susceptibility, shown for instance in figure 4.3c, needs to be scaled with

temperature if a material with a different T_c is used. While $\gamma \propto k_B T_c / E_c M_{\text{eff}}$ would be small compared to chapter 4's aluminum rings, the susceptibility value where fluxoid fluctuations are relevant would also be small, suggesting a lower γ value would be required for the Little-Parks line-shape to be washed out by fluctuations. Along this line of reasoning, large diameter bilayer rings would present an interesting opposite extreme to the dirty, thin rings discussed in chapter 5. In that chapter, fluctuations between fluxoid states are allowed because the ring's susceptibility is reduced by both the small cross section and small superfluid density associated with the small scattering length. Large diameter, small cross section bilayer rings would also have a small zero field susceptibility, and thus fluctuations, but in this case the reduced superfluid density is due to the presence of the normal metal.

6.2 Sputtered Aluminum Rings

In noble metals, such as gold, it is relatively straightforward to achieve thickness limited mean free paths ($l_e \approx 1.4d$) in ebeam-evaporated samples. Among superconductors, aluminum is often used in experiments that require a relatively long coherence length and mean free path. However, it is not trivial to achieve thickness limited mean free paths with ebeam evaporated samples, at least when used in combination with standard liftoff techniques. After discussing the results from early experiments, I will describe a test in which we fabricated rings by etching the aluminum that was previously sputtered onto a clean wafer, a process that, at least in bulk, is known to give a longer scattering length.

Our work with aluminum rings has shown that the mean free path of aluminum is highly dependent on the deposition conditions (table 6.1). The sample's mean free path is likely related to grain size. The grain size is also related to the fact that Al can have a T_c anywhere from the bulk value of 1.15 K to 2.9 K in dirty thin films [23, 68]. It is thought that the oxidation layers formed around grains during the evaporation process helps to prevent room temperature re-crystallization, thus locking in the higher T_c and lower mobility associated with small grains. In one of our samples, where additional oxygen may have been present[16], we observed

line-width-dependent T_c's of up to 1.9 K. In general, longer l_e's are achieved when thicker/wider samples (less edge scattering) are evaporated at high deposition rate, on a warm sample substrate (both associated with larger grains), in a chamber with a lower vapor pressure (less oxygen and other impurities).

Table 6.1: Aluminum film properties during three sample fabrication processes. The mean free path, l_e, was determined from the effect ξ has on the ring's response.

Reference	Deposition Rate	Pressure	Film Thickness	l_e
[49]	$\sim$ 30 Å/sec	1×10^{-7} torr	60 nm	14-25 nm
[16]	$\sim$ 1 Å/sec	$\sim 1 \times 10^{-6}$ torr	40 nm	4 nm
[2]	$\sim$ 0.1 Å/sec	5.7×10^{-7} torr	4 nm	non-SC

Our experience with the variables listed above suggests that it will be difficult to fabricate samples with ebeam evaporators that have mean free paths that are substantially larger than the values presented in table 6.1. Without increasing l_e substantially, $\Delta T_c(\Phi_a)/T_c(0)$ will be reduced by no more than $\sim$6% of $T_c(\Phi_a = 0)$. Noble-metal-like mean free paths may be possible in aluminum created by other means such as MBE. Notably, it is thought that sputter evaporated aluminum films can also have thickness limited mean free paths in some cases [61]. The combination of line-width effects ($\sim$ 30%) and the low temperature reduction in the coherence length criterium (20%) means that a $T_c(\Phi_a = \Phi_0/2) = 0$ could be achieved with $\xi(0) = 400$ nm or $l_e = 140$ nm for a 350 nm radius ring. Since even rings with $\Delta T_c(\Phi_a)/T_c(0) \approx 50\%$ present the possibility of exciting new physics, we fabricated sputtered aluminum rings and present the results in this section.

We received a 200 nm thick aluminum on silicon sample grown by Erik Lucero in the Martinis Group at University of California at Santa Barbara in a dedicated aluminum sputtering system. We fabricated rings with a chlorine based reactive ion etch process in the Plasma Quest® at Stanford Nano-Fabrication facility (SNF). The sparse rings were patterned with ebeam lithography using Ma-N 2403, a novolac-based negative-tone resist. We found that doses that created the intended features also created a resist scum halo, presumably due to electron backscattering, which sometimes extended more than a micron over the nearby area (Fig. 6.2b). This scum acted as an effective etch stop (Fig. 6.2c). The minimum dose-to-clear varied

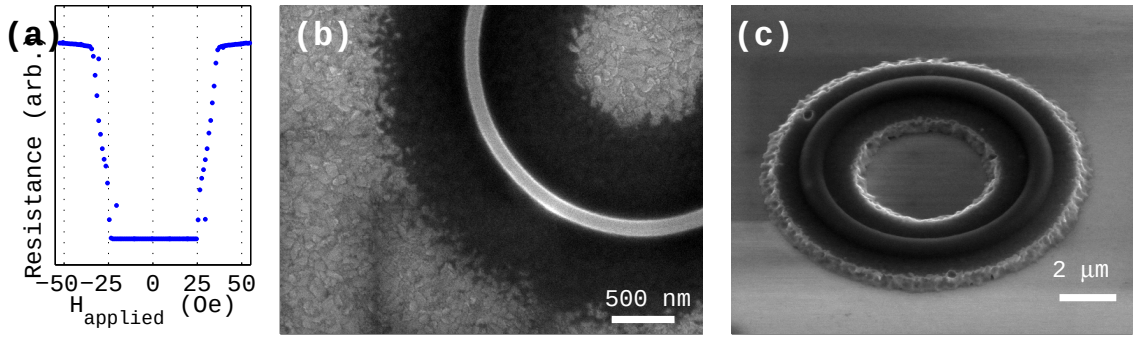

Figure 6.2: a) Resistance of a sputtered aluminum film as a function of applied field, demonstrating a critical field of 24.5 Gauss. b) Ma-N 2403 negative-tone resist patterned by ebeam lithography. The large dark area is thought to be resist scum. Note the large grain size in the aluminum film. c) The resist scum acts as an effective etch stop when making rings. The scum was minimized by varying the dose, beam acceleration, and using various amounts of oxygen plasma etching as a precursor to the ring etch process.

considerably with radius and line width, and the scum was not effectively removed by an oxygen plasma de-scum recipe designed to cut through ≈ 30 nm of resist. A suitable array of rings was created using a combination of these methods: an oxygen de-scum recipe, which removed ≈ 115 nm of the ≈ 350 nm thick resist, and three separate dose factors for each combination of ring parameters.

Low temperature measurements of the bulk film and the above-mentioned rings revealed limits to the use of sputtered aluminum as an ultra-clean material. The critical field (H_{c2}) of bulk films was 24.5 Gauss at 0.51 K, which corresponds to a coherence length $\xi(0.51) = 366$ nm. Extrapolating this to zero temperature using a standard G-L temperature dependence gives $\xi(0) \approx 300$ nm, from which we can derive $l_e = 1.4\xi(0)^2/\xi_0 \approx 80$ nm. This l_e is not thickness-limited, but it is better than what we have observed in ebeam evaporated films (Table 6.1).

The ring fabrication reduced the bulk film l_e, $\xi(0)$ considerably. This may be due to corrosion from the Cl etch, or from additional edge scattering from the large grain structure that is apparent in Fig 6.2a,b. Fitting the cubic component of ring $I - \Phi$ curves, we find $\xi \approx 90$ nm at 0.25 K, which corresponds to $\xi(0) \approx 80$ nm or $l_e \approx 5$ nm.

Another check on the cleanliness of the rings, which would lead to a larger but still not large enough l_e, is that the Little-Parks effect was observable, but the minimum $T_c(\Phi_a)$ was no more than 15% below $T_c(0)$. Difficulties with dilution refrigerator operation lead to the conclusion of this cool down without significant further results.

6.3 Normal Metal/Superconductor Bilayer Rings

The normal/superconductor bilayer idea was originally suggested to us by John Price at the University of Colorado - Boulder. He was exposed to the concept through interactions with the transition edge sensor (TES) community after Xiaxian Zhang's unsuccessful attempts to create $E_c > T_c$ superconducting rings with normal/superconductor alloys. TES sensors and our rings require similar features, but for separate reasons. X-ray/infrared analysis requires large pixel sizes and fast thermal response times (e.g. clean films). A low, tunable T_c allows for optimal thermal noise, typically achieved when $T_c \approx 100 - 200$ mK. In this context, several groups have tested a number of material combinations, including Cu/Mo [38, 34], Au/Mo [20], Al/Ag [89], AlMn/Al [74].

Making bilayered materials with a high transmission coefficient can be challenging. Known issues include oxididation, film stress, impurity levels, corrosion, and interdifussion. Because of these issues, we based our work on a previously engineered system of Cu/Mo, although our project complicates this further with the sub-micron ring line widths. The primary difficulty with this particular combination is the all known chemical etchants that remove copper remove Molybdenum much more aggressively, resulting in interlayer undercutting and roughness that can extend microns from the edge point of a desired feature. The current TES solution is to use normal metal capping layers (Fig 6.3) that provide boundary conditions that reduce edge effects [35]. Such a solution would be very difficult to implement effectively in sub-micron rings.

We worked with a 140 mK T_c, 70 nm thick Cu, 45 nm thick Molybdenum sample, given to us by Gene Hilton at N.I.S.T.-Boulder. Our sparse small-featured rings required ebeam lithography on a negative-tone resist. As described in the previous

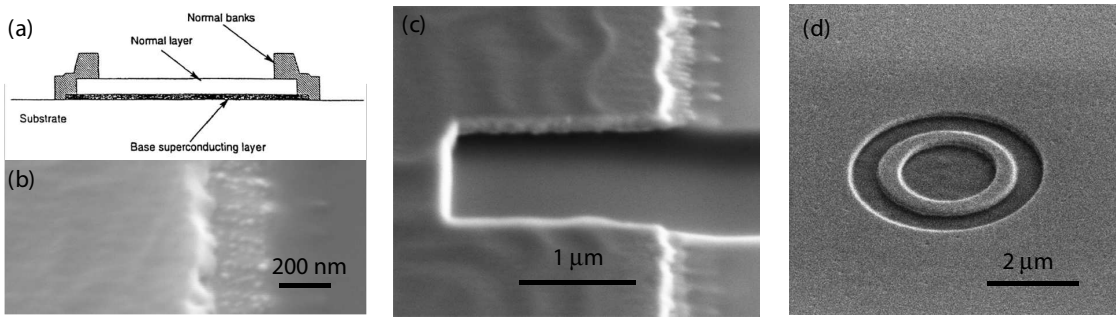

Figure 6.3: Copper/Molybdenum ring fabrication. Asymmetries in etch rates make it difficult to define small features while maintaining a clean normal/superconductor interface. a) Previous work was limited to larger features where normal metal banks could create suitable boundary conditions [35]. b) Ion milling ebeam patterned features left a metallic edge residue, which led to a superconducting response at all dilution refrigerator temperatures. c) Focused ion beam milling (center rectangle) left a clean interface. (Note that copper's wavy surface was due to oxygen plasma etch). d) Rings with $\sim 2\mu$m diameter have been milled for further study.

chapter, we used Ma-N 2403 to form the etch stop. To avoid chemical corrosion at the bilayer interface, we milled the sample with the 500 eV Argon Ion beam in the RIBE system, which removes Ma-N at a rate of $\sim$ 40 nm/s, Cu at $\sim$ 88 nm/s, and Mo at $\sim$ 41 nm/s. The resultant samples had a $T_c > 700$ mK, which was most likely due to a $\approx$ 200 nm wide layer of partially etched, probably mostly Mo material near the edge of each lithographically-defined feature (Fig. 6.3b). This problem was most likely due in part to the previously discussed Ma-N scum problem (Fig. 6.2) and in part due to the reduced argon milling rate of Mo. One possible solution is the FIB milling of micron-scale rings (Fig. 6.3c,d). This possibility requires further research into the effects of the FIB-implanted gallium ions.

Our work on Cu/Mo was curtailed due to the above issues and because the T_c of 140 mK was less than the likely achievable electron temperature. Nevertheless, several projects still seem ripe for achieving the stated results of $E_c > T_c$. Cu/Mo processing could be done with other negative tone ebeam resists that do not have the same scum problems. Al/Ag bilayers have the benefit that they may work with standard PMMA-based lift off processes because they need not be sputter deposited, and thus could

also be deposited with more widely available set of equipment. The main drawback of Al/Ag systems is their reported degradation with time [38, 34]. More exotic, liftoff-compatible bilayers made from Al/AlMn could also offer the promise of high mobility and low Tc [66].

Appendix A

1/f-like Noise in Our System

In chapters 2 and 3, we focussed on the white noise of our susceptometers, comparing it to other scanning SQUIDs (table 3.1), describing the temperature dependence (Fig. 2.5), and discussing cooling fin engineering that may allow for a reduced electron temperature in the shunt resistors (Fig. 3.5). The noise at low-frequencies is often much larger than the white noise floor. At the time of this writing, the SQUID-Array circuit as implemented in our dilution refrigerator has a bandwidth greater than 70 KHz (fig A.1a), with significant phase shifts as low as $\sim$ 5 Khz. When measuring susceptibility, we typically applied a sinusoidal field at frequencies, f, between 4-111 Hz. Ring signals with N periods are sensitive to the noise at $2Nf$, somewhat alleviating this criterum, but other signals such as spin susceptibility measurements do not have this advantage. Low frequency noise is thus often the limiting factor during our measurements. This low frequency $1/f$-like noise is also the limiting noise for flux qubit dephasing and often the most important noise process for a variety of other electronic technologies. It is therefore worthwhile to report the information we have about our system's low-frequency noise.

By a process of elimination, we conclude that the dominant low frequency noise source in our system, when operating properly, is that of the susceptometer itself. The low frequency noise in the devices reported in chapter 2 are consistent with rather large levels characterized elsewhere [86]. These levels are consistent with models which attribute the noise to electronic spins on the surface of the material [48]. The low

frequency noise of the devices reported in chapter 3 are consistently a factor of ~ 2.5 smaller, and could also be caused by critical current fluctuations in the junctions [30] or johnson noise induced currents in nearby metals.

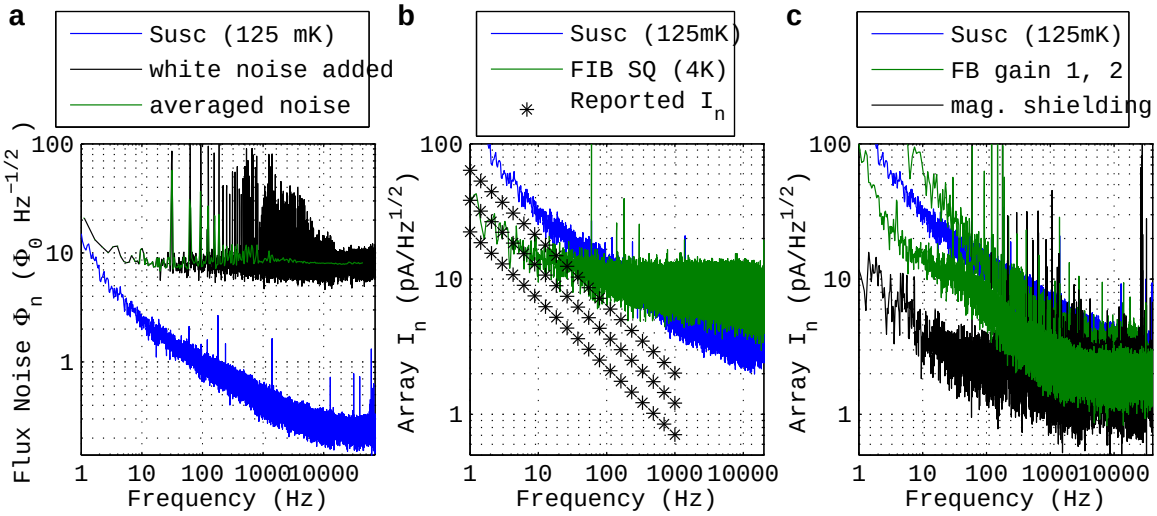

Figure A.1: a) Noise spectrum of a susceptometer from chapter 2 at 125 mK. At this temperature, Low frequency 1/f like noise is dominate up to $\sim$ 10 Khz. The SQUID's frequency independent sensitivity to white noise applied to the field coil demonstrates a bandwidth of $\gtrsim$ 70 Khz. b)The same susceptometer's noise, plotted in units of current at the SQUID serries array preamplifier input. Reported values for low frequency junction noise [30] are less than the typical noise of the SQUIDs reported in 2 , but comparable to the FIB SQUID's described in 3. c) When the array preamplifier is mounted without magnetic shielding, it's noise is comparable to the noise of the susceptometer itself. When the gain of the feedback electronics is not optimized, the readout can provide the dominate low frequency noise. Magnetically shielding the SQUID array significantly improves is low frequency noise properties, presumably by screening the coupling to nearby copper.

A.1 Low frequency noise observations

There are many sources of low frequency noise. We have observed an anomolously large spin signal[14] on the surface of a variety of materials. Random switches in the

orrientations of these spins could be the source of at least some of the 1/f-like noise [48] but it is important to rule out other factors.

Critical current fluctuations are often the dominant low-f noise source in Hi-T_c SQUIDs, but well engineered junctions made from low-T_c materials have less switching states, and critical current fluctuations are often times not the dominant problem [21]. Several reported values [30] are shown in figure A.1b. A typical measurement of a chapter 2 device has a low-f noise above this value. On this generation, we have also implemented a bias reversal scheme [21], but saw no decrease in low frequency noise. Thus, we conclude critical current fluctuations do not limit the first generation of devices. At the time of this writing, bias reversal has not been implemented on the devices in chapter 3, and the measured reduced value of low-f noise could be explained by this effect.

Because low-f noise is a ubiquitous problem, it is important to analyze the amplication stages independently. The measurements reported in figure A.1c were made in closed loop mode, with the SQUID susceptometer unbiased. Sub-optimal feedback gain can add additional low-f noise, presumably from the room temperature ICs. Individual $1/f^2$-like telegraph switchers (plausably from vortex based two-level systems) can occasionally be seen in the array noise. Magnetical shielding significantly reduces the low-f noise in the array (Fig. A.1c). This is presumably due to a reduction in the coupling to normal metal currents, as described in the next section.

A.2 Calculation of low-f noise from nearby metal

We now turn to a method for calculating low frequency noise contribution from johnson noise induced eddy currents in nearby metals. The approach uses the fasthenry inductance program [40] to calculate the complex frequency dependent impedance, $Z(\omega)$, of a given susceptometer design. Nearby normal metal contributes a non-zero frequency-dependent real component to the impedance, which in turn acts as a johnson noise voltage source, $V_n = \sqrt{4k_BT\mathrm{Re}(Z)}$. The corresponding current noise is $I_n = V_n/|Z|$, where most of the impedance is from the reactance $|Z| \approx \mathrm{Im}(Z) \approx i\omega L$, and the flux noise is $\Phi_n = I_n L$.

Included below is a minimized Fasthenry input file. It includes a standard pcb board thickness of copper 380 μm (approximately one wafer thickness) away from the susceptometer. It also includes the parameters for a single square pickup loop that is 3.75 μm on each side. A more complete file includes a second counter-wound pickup loop 1.2 mm away, and two 10 μm counter-wound modulation loops that are spaced by 10 μm in the center of the design. The resulting real impedance contributes 3.2 $\mu\Phi_0/\sqrt{}$(Hz) at 1 Hz. Below 1 Hz, the frequency dependence of the real impedance leads to an overall $1/\sqrt{f}$ (corresponding to $1/f$ noise in $S_\Phi \propto \Phi_n^2$), while above 1 Hz, $\Phi_n \propto 1/f$ as produced by a frequency independent Re(Z). This contribution to low frequency noise is less than the amount observed in the Chapter 2 susceptometers. Furthermore, these susceptometers did not have a noticeable temperature dependence. The noise level reported above is consistent with the noise of the Chapter 3 devices a frequencies below $\sim$ 3 Hz. Thus, the temperature dependence of this noise would be important factor for distinguishing if the noise is derived from spins, critical current fluctuations, or coupling to nearby normal metals.

```
.units um
g1 x1=-1000 y1=-1000 z1=380   ** First do the Cu ground plane
+  x2=1000 y2=-1000 z2=380
+  x3=1000 y3=1000 z3=380
+  thick=35                  ** thickness 1 oz Cu PCB
+  sigma=6000                  ** Copper, RRR=100, 1/(um-ohm)
+  seg1=100 seg2=100
.Default nwinc=1 nhinc=1
N1 x=-598.125 y=.25 z=0
N2 x=-598.125 y=1.875 z=0
N3 x=-601.875 y=1.875 z=0
N4 x=-601.875 y=-1.875 z=0
N5 x=-598.125 y=-1.875 z=0
N6 x=-598.125 y=-.25 z=0
.Default w=.5 h=.2 lambda=.085
E1 N1 N2
```

```
E2 N2 N3
E3 N3 N4
E4 N4 N5
E5 N5 N6
.external N1 Nf
.freq fmin=0.159155  fmax=1.59155 ndec=0.01
.end
```

Appendix B

Concepts for future scanning SQUID designs

Nicholas C. Koshnick, John R. Kirtley, Kathryn A. Moler

An early paper draft intended for submission to *Superconductor Science and Technology*

Abstract

In this paper we discuss design concepts for decreasing the spatial resolution, improving the sensitivity and reducing the invasiveness in scanning Superconducting Quantum Interference Device (SQUID) microscope sensors with integrated flux pickup loops. This can be done not only by reducing the ground-rule line widths and spacings, but also by taking advantage of planarization, reducing flux noise through reducing the SQUID inductance, and reducing back-action through dispersive readouts or on-chip filtering.

Introduction

In chapters 2 and 3 we presented SQUID susceptometers that were designed explicitly for the purpose of measuring mesoscopic objects. The first paper [37] focused on the design's symmetry and on issues relating to operation and performance. The primary achievement of this generation of devices is the ability to measure the magnetic signals from micron-sized objects down to the fundamental Johnson noise limits [15]. The second paper's [50] focus was to reduce the pickup loop size and line width to a point close to the limits set by the superconducting penetration depth of Niobium, the material of choice for superconducting integrated circuits. This paper also demonstrated a design that avoids the thickness problems associated with the multiple layers required by a shielded device with a pickup loop inside a larger field coil. Specifically, layer crossings occurred in such a way that the pickup loop could be positioned as close as possible to the surface (Fig B.1a).

In this work, we discuss additional ways to improve SQUIDs for the purpose of measuring mesoscopic objects as well as imaging. This revision was motivated, in part, by the possibility of a planarized superconducting process [44], with design rules that allow for 250 nm optically defined features, and 1 μm vias. Section B.1 will discuss design improvements made possible by this process. Planarization allows for significantly reduced geometric constraints in the tip design, and continuous conducting layers that reduce vortex motion, thereby allowing for higher locally applied fields. The small feature size allows for a significant reduction in the primary imaging area and in the device's stray pickup area. Section B.2 outlines steps that reduce the SQUID's inductance below that of previous designs. This in turn should allow for a reduction in the SQUIDs flux noise. The most significant reduction in inductance comes from a lower-inductance modulation loop area, and a flux-coupled, single pickup loop design that replaces previous designs, which were direct-coupled and had two pickup loops. The final section, section B.3, describes methods for reducing the amount of Johnson noise seen by the sample, thus allowing for lower sample temperatures and the possibility of measuring additional mesoscopic physics results.

B.1 Advantages of a planarized device with multi-layer sub-micron features

The thickness of superconducting layers in an integrated process is constrained to be larger than the superconducting penetration depth. Layers thinner than this have limited field screening abilities and narrow, thin features can have a non-negligible kinetic inductance. To avoid these potential problems, superconducting foundries post design rules with layers thicknesses between 150 and 200 nm, substantially greater than the $\approx$ 85 nm penetration depth of sputtered Niobium. Given the thickness of individual layers, it is difficult to design sub-micron features into a multi-layered architecture, because small features cannot be reliably fabricated when the underlying height profile varies on the same length scale. It is therefore reasonable to conclude that any new superconducting foundry that utilizes the now readily available sub-micron lithography tools, will also likely choose to adopt chemical-mechanical polishing steps after each conductor/insulator layer.

The adoption of a planarization process would considerably reduce the geometric constraints that determine whether the pickup loop layer will touch down first. Our previous paper [50] described the use of a shallow etch outside the pickup loop and a deep etch outside the field coil. This geometry, shown in the layer diagram in Fig. B.1a, can allow a top-layer pickup loop to touch down first with an alignment tolerance of 3 degrees. Such alignment tolerance is necessary because of the limited alignment ability in home-built scanners and because changes after alignment due to thermal contractions. With a planarized process, a minimum alignment angle is no longer inherent in the design. This means a larger tolerance angle can be achieved (Fig B.1b,c,), or a wider field coil can be used, which has the potential of increasing the maximum usable applied field.

Another very important geometric advantage of a planarized design is that the via to a top layer pickup loop can be much closer to the pickup loop itself, which would allow for a smaller imaging kernel. In the design shown in Fig B.1a, the electrical connection to the top layer is more than 15 μm from the touch down point. Although the magnetic field seen by the pickup loop leads (in layer W2) is partially screened

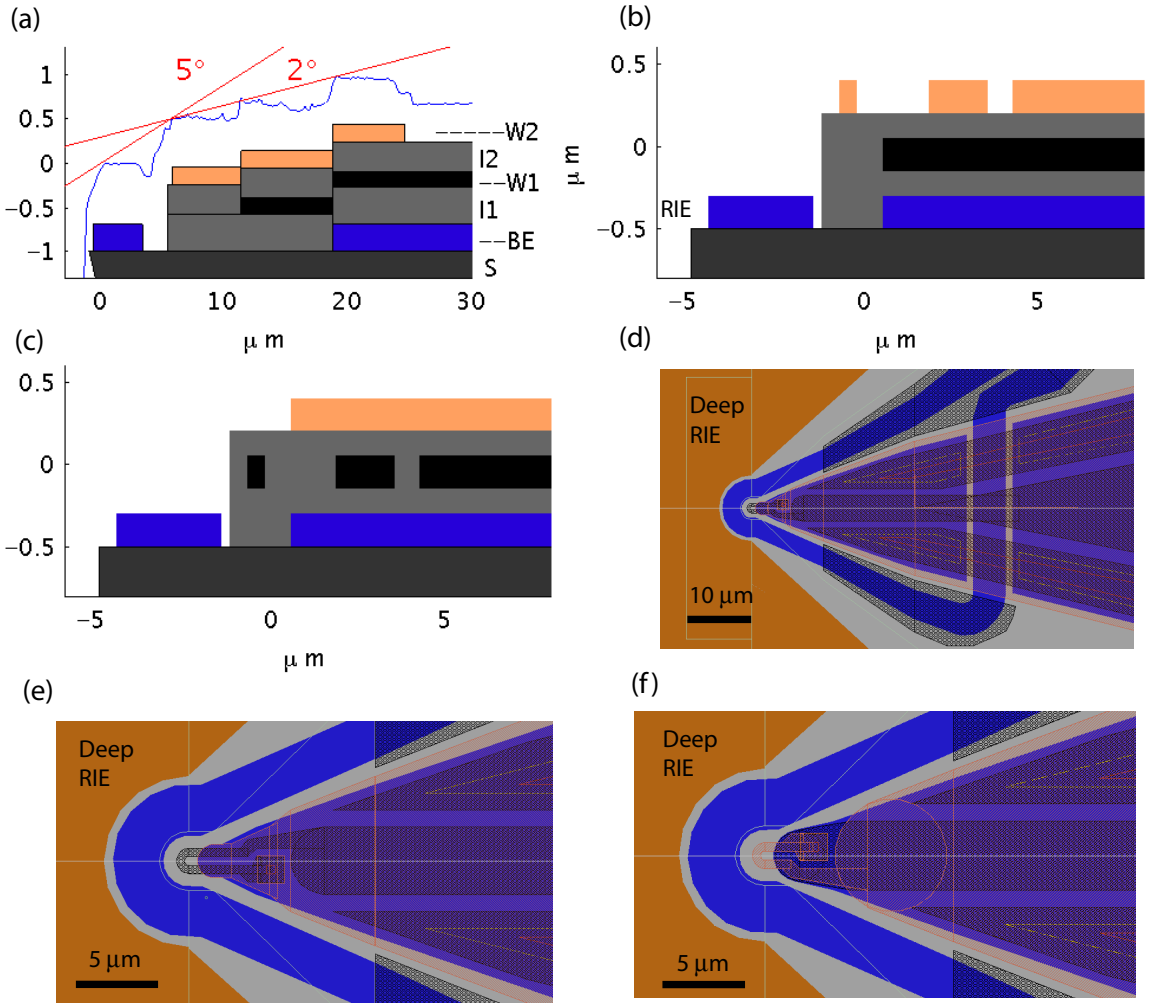

Figure B.1: (Color Online) Comparison of design layouts and layer considerations for a planarized vs. a non-planarized design with sub-micron feature sizes. (a-c) Cross-sections down the the center line of the design showing layer thickness effects. (a) Layer thicknesses of a non planarized process described elsewhere [50], with three superconducting layers (BE, W1, W2), two insulating layers (I1, I2), and the substrate. Atomic force microscope data (blue) shows the tolerance angles that would allow a top layer FIB fabricated pickup loop to touch first. (b) The layer thicknesses of a planarized design allow for much shorter pickup loop leads with the same tolerance angles. (c) The layer thickness diagram of a middle layer pickup loop design. (d-f) Top down view of SQUID design. (d) Passing the field coil under the linear coax section of the SQUID leads allows for a symmetric tip. (e) The mid-layer pickup loop design shown in (c). (f) The top layer design shown in (b).

by the middle layer (W1), the long leads still make for a large area where the SQUID is responsive to the sample's magnetic field. In a planarized design, the vias can be brought as close as is allowed by the design rules.

In previous papers we have demonstrated how susceptometry and background cancellations can enable Johnson noise limited detection of magnetic signals from mesoscopic samples such as superconducting and normal metal rings. Such objects can have periodic response due to quantum mechanical effects, where the amplitude of this response is inversely related to the ring size. The minimum ring size is set by the applied field, because at least half a flux quantum of field is required to distinguish a periodic signal from an (often much larger) linear signal related to spins. Furthermore, we have found that if the field is not sourced by the local field coils, then coupling into the SQUID modulation loop, SQUID array amplifier, and additional vibration-related signals severely reduce the technique's sensitivity. Increasing the width and thickness of the field coil loop is not enough to increase the usable maximum applied field. We have found that these measures increase the field coil current that makes the SQUID go normal, but that sensitivity is no longer optimal once vortices begin to move at a much lower field [50]. Planarization also allows for continuous conducting layers, which reduces thin superconducting areas in the design, and thus should also help to reduce the field coil current where vortices begin to move.

Spatial resolution is an important factor of a SQUID's design for many reasons. In the large set of cases where it is acceptable have the pickup loop $\gtrapprox$ 300 nm from the sample, it is advantageous to put the pickup loop in the middle layer as shown in Figs. B.1c-e. This allows for a minimal image kernel size, because both the top and bottom layers can screen the pickup loop from magnetic field. The width of the shielding layers has been kept to a minimum in the area immediately before the pickup loop to minimize the flux-focusing effects that can increase the effective pickup loop size [42].

Our design for a SQUID with a pickup loop in the top layer, Fig. B.1f, is similar to that of Fig. B.1e, except that the flux-focusing condition was relaxed to allow for shorter leads and thus less stray coupling. Both designs have a field coil line that

crosses far behind the pickup loop area in a region where the SQUID has a linear coaxial geometry, Fig. B.1d. This allows for a symmetric tip, minimal unshielded leads, and thus a pickup and transition area that contributes minimally to the inductance of the rest of the design.

B.2 Optimizing flux sensitivity through reduced inductance

While table 3.1 demonstrates that the flux sensitivity of our SQUIDs is comparable to or better than scanning devices of its kind, quantum-limited devices [21] with flux sensitivities as low as $\sim 0.08\mu\Phi_0/\sqrt{Hz}$ [5] have been realized. Referring back to Fig. 3.5, we note that our designs are limited by thermal noise in the shunt resistors. When optimally tuned, this Johnson noise dependence scales like $L^{3/2}$ where L is the SQUID's self inductance [79]. The quantum limited flux noise has a $L^{1/2}$ dependence when optimally tuned. By reducing L one can both reduce the SQUID's overall white noise floor, and increase the temperature, where temperature-independent quantum noise becomes the dominate noise source.

For both the optically [37] and FIB [50] fabricated SQUIDs, the inductance [40] of each section is approximately 12 pH per pickup loop, 10 pH/mm in the linear coaxial connection region, and $\sim$ 55 pH for the core junction/modulation loop area.

The majority of the core area inductance in the previous designs come from the two modulation loops, each with an inner diameter of 10 μm. Estimating from their inner diameter [39], these two loops contribute 30 pH to the total inductance. This contribution would decrease linearly with a reduction in the diameter of the loop. The main drawback to this in our case (low bandwidth requirements) is that more current is required to keep the SQUID in a flux-locked loop. Increases in the amount of current sent to the modulation loops can lead to heating from stray resistances in dilution refrigerator temperature wiring. Reducing the modulation loop diameter to 4 μm decreases the self inductance to 12 pH, while maintaining a reasonable 175 uA/phi_0 mutual inductance. Further enhancement could come from having only one

modulation loop in a non-gradiometric design. Small modulation loops with multiple windings could also allow for smaller loops.

Another avenue worth considering for reduced inductance involves questioning the assumption that dual, counter wound pickup coils aid background subtraction. Assuming that comparative/background measurements are made, either by scanning or by systematically positioning the sensor at various points around a mesoscopic object, the net effect of the counter winding is to reduce the pickup loop coupling to the field coils to a sufficient extent that the dynamic range of the direct signal does not overwhelm the room temperature electronics. For small pickup loops the field coil coupling is already small, thus the counter-winding may not be necessary. It is also physically reasonable to require room temperature electronics that send some of the field coil signal to the modulation loop, so that this direct coupled signal is cancelled before amplification. It is thus possible that a one-sided SQUID could have lower noise.

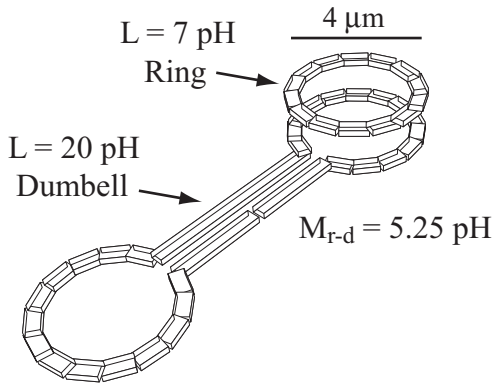

Figure B.2: A simplified model for a flux coupled SQUID, which consists of a dumbell shaped flux coupler with 4 μm loops, and a 4 μm ring with specified inductances.

Directly cutting out one of the pickup loops creates an unbalanced inductance in the two sides of the SQUID circuit. This leads to non-symmetric I-V characteristics [67] and slightly more complicated modeling, but does not necessarily reduce the flux sensitivity. A more reliable design may be to change the bulk of the current design into a flux coupler with just the central part being an independent low-inductance SQUID. A simplified Fasthenry [40] model of superconducting elements (Fig B.2)

illustrates the tradeoffs between the reduced coupling to the sample, and the reduction in the SQUID's inductance. It considers the inductances of two objects: a simple 4 μm diameter ring, and a "dumbell" consisting of two 4 μm diameter loops coupled by two lines. This dumbell object has a self inductance, $L_d = 20$ pH, and can be considered either as a direct coupled SQUID or the flux coupler that is coupled to the ring. In the latter case, the ring, which has a self inductance $L_r = 7$ pH, represents the non-directly coupled SQUID. The mutual inductance between the ring and dumbell is $M_{r-d} = 5.25$ pH. The flux-coupled SQUID only sees $M_{r-d}/L_d = .26$ as much flux as its direct-coupled counterpart, but when limited by Johnson noise, it has $(L_r/L_d)^{3/2} = .21$ as much white noise. Flux-coupled and direct-coupled SQUIDs therefore have very similar white noise characteristics until the inductance is small enough that the $L^{1/2}$-dependent quantum limit is applicable. The main advantage may be that a flux-coupled SQUID could have only one pickup loop, substantially reducing the inductance without leaving the SQUID unbalanced.

B.3 Reducing SQUID sample back action

Understanding the way the SQUID perturbs the sample is an important part of measuring quantum effects in mesoscopic samples. We will consider one of the simplest kinds of back action on the sample, joule heating from SQUID radiation at the Josephson frequency, f_j. While studying persistent currents in normal metal rings, we discovered that metallic regions had a spin-like linear susceptibility that increased with decreasing temperature. The coupled SQUID radiation of $\approx 10^{-14}$ Watts for our $\approx 2\Omega$ rings, balanced by electron-phonon limited cooling [85], limited the temperature in isolated rings to about 200 mK [15]. Since there are many interesting effects that only occur below this temperature, it is important to consider design aspects that can reduce this form of back action.

In general, the cost of reduced back-action is often reduced sensitivity. A simple estimate for the energy dissipated in a ring is given by the flux-change-induced ring-voltage

$$V_{ring} = \frac{d\Phi}{dt} = I_0 f_j M_{SQ-s} \tag{B.1}$$

where M_{SQ-s} is the mutual inductance between the SQUID and the sample. The power dissipated is then just V_{ring}^2/R, where R is the ring's resistance. One can reduce this heating effect by moving the SQUID further away from the sample, thereby reducing M_{SQ-s}. This is only a useful approach when there is ample signal. Another approach is to bias the SQUID with the lowest possible voltage, and thus lowest operating f_j. In general, this approach is limited by the minimum voltage bias ($\propto k_B T/e$), where the SQUID noise begins to deteriorate, and by the feedback electronics' ability to lock into a signal that has a reduced modulation amplitude.

The noise dependance on $L^{3/2}$, mentioned in section B.2, was calculated in the $\beta_L = 2LI_0/\Phi_0 \approx 1$ limit, where the standard design rules [79] set critical current to $I_0 = \Phi_0/2L$, and the appropriate shunt resistor is determined by $\beta_c \approx 1$. Increasing the flux sensitivity by reducing L thus comes with an increased I_0 and correspondingly increased radiation on the sample. While the SQUID's energy sensitivity, Φ_n^2/L, is optimal for $\beta_L \approx 1$, the relevant figure of merit when measuring mesoscopic samples must include back action. The optimal point in this case would probably require $I_0 < \Phi_0/2L$. This effect has been analyzed in quantum limited SQUIDs [24].

Another way to reduce the back action on the sample is to read out the the SQUID dispersively. Josephson radiation (and thus sample heating) does not occur when the SQUID is in the zero voltage state. Dispersive readout measures the flux-dependence of the inductance, without inducing voltage, typically by placing the SQUID in some kind of resonant circuit. Thus the Josephson radiation (of typically 1-10 GHz) gets replaced by the readout frequency ($\sim$ 100 Mhz). One excellent way to implement dispersive readout involves the microstrip SQUID amplifier designed by the group of John Clarke [65]. The superconducting qubit community has invested considerable effort in comparing the back action from this type of measurement to the back action from other non-voltage state readout schemes, such as the scanning SQUIDs [32] that rely on the bias current switching threshold.

A final way to limit SQUID heating would be to implement on-chip filters inside the SQUID circuit that divert the Josephson frequency currents from the pickup loop and sample. This approach was implemented with LC filters by John Price's group [90] in a two-chip design. Implementing the same type of LC filters on a single chip

would help to keep inductive losses to a minimum. We estimate the feasibility of this approach by noting the capacitance in our 40 μm wide, 1.2 mm long linear coaxial coupler with a 200 nm wire-to-wire spacing is roughly 20 pF. The 30 pH pickup loop and strip line inductance thus has a cutoff frequency of 6.5 Ghz, indicating that a reasonable portion of the Josephson frequency current is already not flowing through the pickup loop itself. The radiation from the SQUID would be further decoupled from the sample if the on-chip capacitance was further increased.

A second type of on-chip filter involves placing a placing a small (0.3 Ω) shunting resistor between the SQUID and the pickup loop. This form of an RC filter works as a frequency dependent current divider, where the Josephson frequency currents would see a reactance of 0.95 Ω (15 pH at $\sim$ 10 Ghz) and thus largely run through the shunt, whereas the zero frequency currents that set up the SQUID phase relations would still all be coupled to the pickup loop itself.

As with the LC filter technique, this logic intrinsically relies on the fact that we are trying to measure time-averaged equilibrium currents in our rings, and thus can simply limit the frequencies where effective coupling occurs to some value below the frequencies involved with the intrinsic SQUID (or for that mater, ring) dynamics. The LC filter could effectively shunt essentially all of the Josephson frequency radiation if such an ideal capacitor layer, with sufficiently low stray inductance, could be incorporated into the superconducting process. The effectiveness of the RC filter is limited by the Johnson current noise it sends through the pickup loop, integrated up to the bandwidth set by the LC filter. In practice, however, it is likely that this RC shunting technique could reduce the sample temperature significantly before this limit sets in.

Bibliography

[1] Attocube Systems AG.

[2] An Aug.-Sep. 2008 ring cool down intended to provide extra data for the phase fluctuations discussed in chapter 5.

[3] V. Ambegaokar and U. Eckern. Nonlinear diamagnetic response in mesoscopic rings of superconductors above tsub c. *Europhys. Lett.*, 13(8):733 – 8, Dec 1990.

[4] A. Anthore, H. Pothier, and D. Esteve. Density of states in a superconductor carrying a supercurrent. *Physical Review Letters*, 90(12):127001, March 2003.

[5] D. D. Awschalom, J. R. Rozen, M. B. Ketchen, W. J. Gallagher, A. W. Kleinsasser, R. L. Sandstrom, and B. Bumble. Low-noise modular microsusceptometer using nearly quantum limited dc squids. *Applied Physics Letters*, 53(21):2108–2110, November 1988.

[6] D. D. Awschalom, J. Warnock, and S. Vonmolnar. Low-temperature magnetic spectroscopy of a dilute magnetic semiconductor. *Physical Review Letters*, 58(8):812 – 15, FEB 1987.

[7] J. G. Bednorz and K. A. Müller. Possible high t_c superconductivity in the ba-la-cu-o system. *Zeitschrift für Physik B Condensed Matter*, 64(2):189–193, June 1986.

[8] Jorge Berger. Ginzburg-landau equations with consistent langevin terms for nonuniform wires. *Phys. Rev. B*, 75(18):184522, 2007.

[9] Jorge Berger and Jacob Rubinstein. Topology of the order parameter in the little-parks experiment. *Phys. Rev. Lett.*, 75(2):320–322, Jul 1995.

[10] Alexey Bezryadin. Quantum suppression of superconductivity in nanowires. *Journal of Physics: Condensed Matter*, 20:043202, 2008.

[11] P. G. Bjornsson, B. W. Gardner, J. R. Kirtley, and K. A. Moler. Scanning superconducting quantum interference device microscope in a dilution refrigerator. *Rev. Sci. Inst.*, 72(11):4153 – 8, NOV 2001.

[12] P. G. Bjornsson, Y. Maeno, M. E. Huber, and K. A. Moler. Scanning magnetic imaging of srsub 2ruosub 4. *Physical Review B (Condensed Matter and Materials Physics)*, 72(1):12504 – 1, 2005.

[13] Ania Bleszynski and Jack Harris. (unpublished).

[14] H. Bluhm, N. C. Koshnick, J.A. Bert, M. E. Huber, and K. A. Moler. Spin-like susceptibility of metallic and insulating thin films at low temperature. (unpublished).

[15] Hendrik Bluhm, Nicholas C Koshnick, Julie A Bert, Martin E Huber, and Kathryn A Moler. Persistent currents in normal metal rings. *arXiv.org:0810.4384*, October 2008. Accepted for publication in Physical Review Letters.

[16] Hendrik Bluhm, Nicholas C. Koshnick, Martin E. Huber, and Kathryn A. Moler. Magnetic response of mesoscopic superconducting rings with two order parameters. *Physical Review Letters*, 97:237002–4, December 2006.

[17] Hendrik Bluhm, Nicholas C Koshnick, Martin E Huber, and Kathryn A Moler. Multiple fluxoid transitions in mesoscopic superconducting rings. *arXiv.org:0709.1175*, September 2007.

[18] Ernst Helmut Brandt and John R. Clem. Superconducting thin rings with finite penetration depth. *Physical Review B*, 69:184509, May 2004.

[19] N. Byers and C. N. Yang. Theoretical considerations concerning quantized magnetic flux in superconducting cylinders. *Phys. Rev. Lett.*, 7(2):46–49, Jul 1961.

[20] J. A. Chervenak, F. M. Finkbeiner, T. R. Stevenson, D. J. Talley, R. P. Brekosky, S. R. Bandler, E. Figueroa-Feliciano, M. A. Lindeman, R. L. Kelley, T. Saab, and C. K. Stahle. Fabrication of transition edge sensor x-ray microcalorimeters for constellation-x. *Nuclear Instruments and Methods in Physics Research Section A: Accelerators, Spectrometers, Detectors and Associated Equipment*, 520(1-3):460–462, March 2004.

[21] J. Clarke and A. I. Braginski, editors. *The SQUID Handbook*. Weinheim : Wiley-VCH, 2003.

[22] J.-P. Cleuziou, W. Wernsdorfer, V. Bouchiat, T. Ondarcuhu, and M. Monthioux. Carbon nanotube superconducting quantum interference device. *Nat Nano*, 1:53–59, October 2006.

[23] Roger W. Cohen and B. Abeles. Superconductivity in granular aluminum films. *Physical Review*, 168(2):444, April 1968.

[24] V. Danilov, K. Likharev, and A. Zorin. Quantum noise in squids. *Magnetics, IEEE Transactions on*, 19(3):572–575, 1983.

[25] M. Daumens, C. Meyers, and A. Buzdin. Little-parks effect for arbitrary geometry: fluctuations of the magnetic moment of mesoscopic loops. *Physics Letters A*, 248:445–452, Nov 1998.

[26] V.J. Emery and S.A. Kivelson. Importance of phase fluctuations in superconductors with small superfluid density. *Nature*, 374:434–437, March 1995.

[27] M. Freitag, J.C. Tsang, J. Kirtley, A. Carlsen, J. Chen, A. Troeman, H. Hilgenkamp, and Ph. Avouris. Electrically excited, localized infrared emission from single carbon nanotubes. *Nano Letters*, 6:1425–1433, July 2006.

[28] Brian W. Gardner, Janice C. Wynn, Per G. Bjornsson, Eric W. J. Straver, Kathryn A. Moler, John R. Kirtley, and Mark B. Ketchen. Scanning superconducting quantum interference device susceptometry. *Review of Scientific Instruments*, 72(5):2361–2364, 2001.

[29] N. Giordano. Evidence for macroscopic quantum tunneling in one-dimensional superconductors. *Physical Review Letters*, 61:2137, October 1988.

[30] D. J. Van Harlingen, T. L. Robertson, B. L. T. Plourde, P. A. Reichardt, T. A. Crane, and John Clarke. Decoherence in josephson-junction qubits due to critical-current fluctuations. *Physical Review B*, 70(6):064517, 2004.

[31] K. Hasselbach, D. Mailly, and J. R. Kirtley. Micro-superconducting quantum interference device characteristics. *Journal of Applied Physics*, 91:4432–4437, April 2002.

[32] K. Hasselbach, C. Veauvy, and D. Mailly. Microsquid magnetometry and magnetic imaging. *Physica C*, 332:140–147, May 2000.

[33] M. Hayashi and H. Ebisawa. Superconducting fluctuations in a mesoscopic ring structure: Little-Parks oscillation in fluctuation regime. *Physica C Superconductivity*, 352:191–194, April 2001.

[34] G.C. Hilton, J.M. Martinis, K.D. Irwin, N.F. Bergren, D.A. Wollman, M.E. Huber, S. Deiker, and S.W. Nam. Microfabricated transition-edge x-ray detectors. *Applied Superconductivity, IEEE Transactions on*, 11(1):739–742, 2001.

[35] Gene C. Hilton, John M. Martinis, Kent D. Irwin, and David A. Wollman. Normal metal boundary conditions for multi-layer tes detectors, September 2002. U.S. Patent Classification: 250/336.2 ; International Classification: H01L 3900.

[36] M. E. Huber, P. A. Neil, R. G. Benson, D. A. Burns, A. F. Corey, C. S. Flynn, Y. Kitaygorodskaya, O. Massihzadeh, J. M. Martinis, and G. C. Hilton. Dc squid series array amplifiers with 120 mhz bandwidth (corrected). *Applied Superconductivity, IEEE Transactions on*, 11(2):4048–4053, 2001.

[37] Martin E. Huber, Nicholas C. Koshnick, Hendrik Bluhm, Leonard J. Archuleta, Tommy Azua, Per G. Björnsson, Brian W. Gardner, Sean T. Halloran, Erik A. Lucero, and Kathryn A. Moler. Gradiometric micro-squid susceptometer for scanning measurements of mesoscopic samples. *Review of Scientific Instruments*, 79(5):053704, 2008.

[38] K. D. Irwin, G. C. Hilton, John M. Martinis, S. Deiker, N. Bergren, S. W. Nam, D. A. Rudman, and D. A. Wollman. A mo-cu superconducting transition-edge microcalorimeter with 4.5ev energy resolution at 6kev. *Nuclear Instruments and Methods in Physics Research Section A: Accelerators, Spectrometers, Detectors and Associated Equipment*, 444(1-2):184–187, April 2000.

[39] J. Jaycox and M. Ketchen. Planar coupling scheme for ultra low noise DC SQUIDs. *Magnetics, IEEE Transactions on*, 17(1):400–403, 1981.

[40] M. Kamon, M. J. Tsuk, and J. K. White. Fasthenry: a multipole-accelerated 3-d inductance extraction program. *IEEE Transactions on Microwave Theory and Techniques*, 42(9):1750 – 1758, Sept 1994.

[41] M. B. Ketchen and J. R. Kirtley. Design and performance aspects of pickup loop structures for miniature squid magnetometry. *IEEE Transactions on Applied Superconductivity*, 5(2):2133 – 2136, Jun 1995.

[42] M. B. Ketchen and J. R. Kirtley. Design and performance aspects of pickup loop structures for miniature squid magnetometry. *IEEE Transactions on Applied Superconductivity*, 5(2):2133 – 2136, Jun 1995.

[43] M. B. Ketchen, T. Kopley, and H. Ling. Miniature squid susceptometer. *Applied Physics Letters*, 44(10):1008 – 10, May 1984.

[44] M. B. Ketchen, D. Pearson, A. W. Kleinsasser, C.-K. Hu, M. Smyth, J. Logan, K. Stawiasz, E. Baran, M. Jaso, T. Ross, K. Petrillo, M. Manny, S. Basavaiah, S. Brodsky, S. B. Kaplan, W. J. Gallagher, and M. Bhushan. Sub-mu m,

planarized, Nb-AlO_x -Nb josephson process for 125 mm wafers developed in partnership with si technology. *Applied Physics Letters*, 59(20):2609–2611, November 1991.

[45] M.B. Ketchen, D.D. Awschalom, W.J. Gallagher, A.W. Kleinsasser, R.L. Sandstrom, J.R. Rozen, and B. Bumble. Design, fabrication, and performance of integrated miniature squid susceptometers. *Magnetics, IEEE Transactions on*, 25:1212–1215, 1989.

[46] J. R. Kirtley, M. B. Ketchen, K. G. Stawiasz, J. Z. Sun, W. J. Gallagher, S. H. Blanton, and S. J. Wind. High-resolution scanning squid microscope. *Applied Physics Letters*, 66:1138–1140, February 1995.

[47] John R. Kirtley and John P. Wikswo. Scanning squid microscopy. *Annual Review of Materials Science*, 29(1):117–148, 1999.

[48] Roger H. Koch, David P. DiVincenzo, and John Clarke. Model for 1/f flux noise in squids and qubits. *Physical Review Letters*, 98(26):267003–4, June 2007.

[49] Nicholas C. Koshnick, Hendrik Bluhm, Martin E. Huber, and Kathryn A. Moler. Fluctuation superconductivity in mesoscopic aluminum rings. *Science*, 318:1440–1443, November 2007.

[50] Nicholas C. Koshnick, Martin E. Huber, Julie A. Bert, Clifford W. Hicks, Jeff Large, Hal Edwards, and Kathryn A. Moler. A terraced scanning superconducting quantum interference device susceptometer with submicron pickup loops. *Applied Physics Letters*, 93(24):243101–3, December 2008.

[51] J M Kosterlitz and D J Thouless. Ordering, metastability and phase transitions in two-dimensional systems. *Journal of Physics C: Solid State Physics*, 6(7):1181–1203, 1973.

[52] S. K. H. Lam and D. L. Tilbrook. Development of a niobium nanosuperconducting quantum interference device for the detection of small spin populations. *Applied Physics Letters*, 82(7):1078–1080, 2003.

[53] J. S. Langer and Vinay Ambegaokar. Intrinsic resistive transition in narrow superconducting channels. *Phys. Rev.*, 164(2):498–510, Dec 1967.

[54] A. Larkin and A. A. Varlamov. *Theory of Fluctuations in Superconductors*. Oxford University Press, USA, 2005.

[55] C. N. Lau, N. Markovic, M. Bockrath, A. Bezryadin, and M. Tinkham. Quantum phase slips in superconducting nanowires. *Phys. Rev. Lett.*, 87(21):217003, Nov 2001.

[56] W. A. Little and R. D. Parks. Observation of quantum periodicity in the transition temperature of a superconducting cylinder. *Phys. Rev. Lett.*, 9(1):9, Jul 1962.

[57] Y. Liu, H. Wang, Yu. Zadorozhny, M.M. Rosario, B.Y. Rock, N.A. Kurz, and P.T. Carrigan. Ultrathin, doubly connected superconducting cylinders: A link between one- and two-dimensional superconductors. *Physica C: Superconductivity*, 468(4):331–336, February 2008.

[58] Y. Liu, Yu. Zadorozhny, M. M. Rosario, B. Y. Rock, P. T. Carrigan, and H. Wang. Destruction of the Global Phase Coherence in Ultrathin, Doubly Connected Superconducting Cylinders. *Science*, 294(5550):2332–2334, 2001.

[59] D. Mailly, C. Chapelier, and A. Benoit. Experimental observation of persistent currents in gaas-algaas single loop. *Physical Review Letters*, 70(13):2020, March 1993.

[60] J. B. Majer, J. R. Butcher, and J. E. Mooij. Simple phase bias for superconducting circuits. *Applied Physics Letters*, 80:3638–3640, 2002.

[61] J. Martinis. personal communication, 2008.

[62] K. A. Matveev, A. I. Larkin, and L. I. Glazman. Persistent current in superconducting nanorings. *Physical Review Letters*, 89(9):096802, 2002. Copyright (C) 2009 The American Physical Society; Please report any problems to prola@aps.org.

[63] D. E. McCumber and B. I. Halperin. Time scale of intrinsic resistive fluctuations in thin superconducting wires. *Phys. Rev. B*, 1(3):1054–1070, Feb 1970.

[64] Toshimitsu Morooka, Keiichi Tanaka, Akikazu Odawara, Satoshi Nakayama, Atsushi Nagata, Masanori Ikeda, and Kazuo Chinone. Development of scanning squid microscope for studying superconducting films and devices. *Physica C*, 335:157–163, June 2000.

[65] Michael Muck, J. B. Kycia, and John Clarke. Superconducting quantum interference device as a near-quantum-limited amplifier at 0.5 ghz. *Applied Physics Letters*, 78(7):967–969, February 2001.

[66] G. O'Neil, D. Schmidt, N. A. Miller, J. N. Ullom, A. Williams, G. B. Arnold, and S. T. Ruggiero. Observation of nonmagnetic resonant scattering effects by tunneling in dilute al-mn alloy superconductors. *Physical Review Letters*, 100(5):056804–4, February 2008.

[67] R. L. Peterson and C. A. Hamilton. Analysis of threshold curves for superconducting interferometers. *Journal of Applied Physics*, 50:8135–8142, December 1979.

[68] Richard B. Pettit and J. Silcox. Film structure and enhanced superconductivity in evaporated aluminum films. *Physical Review B*, 13(7):2865, April 1976.

[69] T. M. Rice. Superconductivity in one and two dimensions. *Phys. Rev.*, 140(6A):A1889–A1891, Dec 1965.

[70] Eberhard K. Riedel and Felix von Oppen. Mesoscopic persistent current in small rings. *Physical Review B*, 47(23):15449, June 1993.

[71] M. M. Rosario, Y. Zadorozhny, B. Y. Rock, P. T. Carrigan, H. Wang, and Y. Liu. Superconducting fluctuations in the destructive regime of ultrathin, superconducting cylinders. *Physica B Condensed Matter*, 329:1415–1416, May 2003.

[72] J.E. Sauvageau, C.J. Burroughs, P.A.A. Booi, M.W. Cromar, R.P. Benz, and J.A. Koch. Superconducting integrated circuit fabrication with low temperature ecr-based pecvd sio_2 dielectric films. *Applied Superconductivity, IEEE Transactions on*, 5:2303–2309, 1995.

[73] D. J. Scalapino, M. Sears, and R. A. Ferrell. Statistical mechanics of one-dimensional ginzburg-landau fields. *Phys. Rev. B*, 6(9):3409–3416, Nov 1972.

[74] D. R. Schmidt, K. W. Lehnert, A. M. Clark, W. D. Duncan, K. D. Irwin, N. Miller, and J. N. Ullom. A superconductor–insulator–normal metal bolometer with microwave readout suitable for large-format arrays. *Applied Physics Letters*, 86(5):053505–3, 2005.

[75] G. Schwiete. personal communication, 2007.

[76] Georg Schwiete and Yuval Oreg. Persistent current in small superconducting rings. *arXiv.org:0812.4088*, December 2008.

[77] J. Siegel, J. Witt, N. Venturi, and S. Field. Compact large-range cryogenic scanner. *Review of Scientific Instruments*, 66(3):2520 – 3, MAR 1995.

[78] B. Spivak, P. Oreto, and S. A. Kivelson. Theory of quantum metal to superconductor transitions in highly conducting systems. *Physical Review B (Condensed Matter and Materials Physics)*, 77(21):214523–18, June 2008.

[79] Claudia D. Tesche and John Clarke. dc squid: Noise and optimization. *Journal of Low Temperature Physics*, 29:301–331, November 1977.

[80] Claudia D. Tesche and John Clarket. dc squid: Current noise. *Journal of Low Temperature Physics*, 37(3):397–403, November 1979.

[81] A.G.P. Troeman, H. Derking, B. Borger, J. Pleikies, D. Veldhuis, and H. Hilgenkamp. Nanosquids based on niobium constrictions. *Nano Letters*, 7:2152–2156, July 2007.

[82] Oskar Vafek, M. R Beasley, and Steven A Kivelson. Disorder induced non-fermi liquid near a metal-superconductor quantum phase transition. *arXiv.org:0505688*, May 2005.

[83] F. von Oppen and E. K. Riedel. Flux-periodic persistent current in mesoscopic superconducting rings close to tsub c. *Phys. Rev. B*, 46(5):3203 – 6, AUG 1992.

[84] L.N. Vu and D.J. Van Harlingen. Design and implementation of a scanning squid microscope. *Applied Superconductivity, IEEE Transactions on*, 3:1918–1921, 1993.

[85] F. C. Wellstood, C. Urbina, and John Clarke. Hot-electron effects in metals. *Physical Review B*, 49:5942, March 1994.

[86] Frederick C. Wellstood, Cristian Urbina, and John Clarke. Low-frequency noise in dc superconducting quantum interference devices below 1 k. *Applied Physics Letters*, 50(12):772–774, 1987.

[87] W. Wernsdorfer, K. Hasselbach, D. Mailly, B. Barbara, A. Benoit, L. Thomas, and G. Suran. Dc-squid magnetization measurements of single magnetic particles. *Journal of magnetism and magnetic materials*, 145(1-2):33–39, 1995.

[88] W. Wernsdorfer, E. Bonet Orozco, K. Hasselbach, A. Benoit, B. Barbara, N. Demoncy, A. Loiseau, H. Pascard, and D. Mailly. Experimental evidence of the néel-brown model of magnetization reversal. *Physical Review Letters*, 78:1791, March 1997. and related refferences.

[89] D.A. Wollman, K.D. Irwin, G.C. Hilton, L.L. Dulcie, D.E. Newbury, and J.M. Martinis. High-resolution, energy-dispersive microcalorimeter spectrometer for x- ray microanalysis. *Journal of Microscopy*, 188(3):196–223, 1997.

[90] X. Zhang and J. C. Price. Susceptibility of a mesoscopic superconducting ring. *Phys. Rev. B*, 55(5):3128 – 3140, FEB 1997.

[91] Xiaxian Zhang. *SQUID Microsusceptometry of Mesoscopic Superconducting Rings*. PhD thesis, University of Colorado, 1996.